SANDIA REPORT

SAND2015-8344
Unlimited Release
September 2015

Appraisal of Transport and Deformation in Shale Reservoirs using Natural Noble Gas Tracers

Jason E. Heath, Kristopher L. Kuhlman, David G. Robinson, Stephen J. Bauer, and W. Payton Gardner

Prepared by
Sandia National Laboratories
Albuquerque, New Mexico 87185 and Livermore, California 94550

Sandia National Laboratories is a multi-program laboratory managed and operated by Sandia Corporation, a wholly owned subsidiary of Lockheed Martin Corporation, for the U.S. Department of Energy's National Nuclear Security Administration under contract DE-AC04-94AL85000.

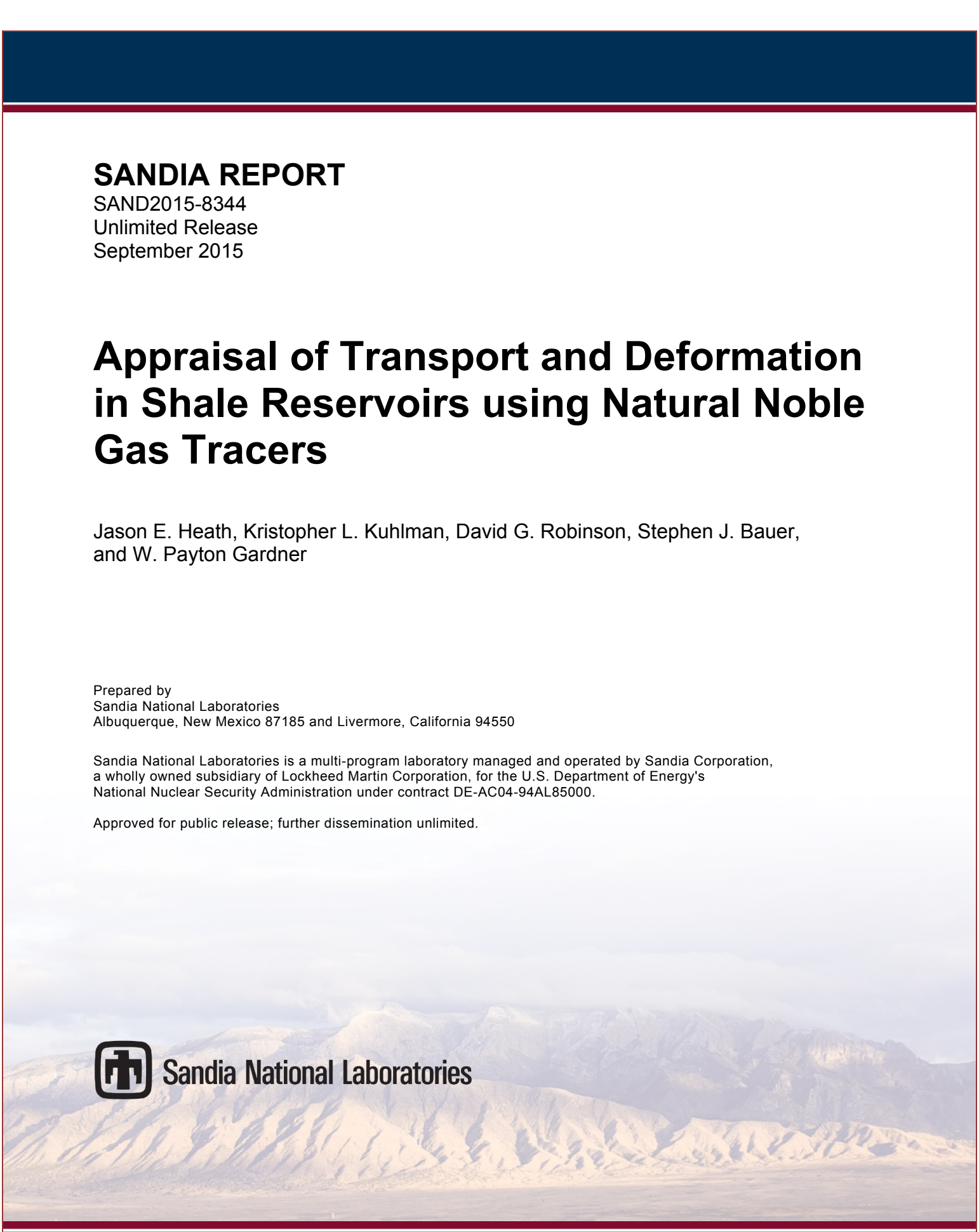

Sandia National Laboratories

Issued by Sandia National Laboratories, operated for the United States Department of Energy by Sandia Corporation.

Available to DOE and DOE contractors from
U.S. Department of Energy
Office of Scientific and Technical Information
P.O. Box 62
Oak Ridge, TN 37831

Telephone: (865) 576-8401
Facsimile: (865) 576-5728
E-Mail: reports@osti.gov
Online ordering: http://www.osti.gov/scitech

Available to the public from
U.S. Department of Commerce
National Technical Information Service
5301 Shawnee Rd
Alexandria, VA 22312

Telephone: (800) 553-6847
Facsimile: (703) 605-6900
E-Mail: orders@ntis.gov
Online order: http://www.ntis.gov/search

SAND2015-8344
Unlimited Release
September 2015

Appraisal of Transport and Deformation in Shale Reservoirs using Natural Noble Gas Tracers

Jason E. Heath
Geomechanics
Sandia National Laboratories
PO Box 5800
Albuquerque, NM 87185-MS0750

Kristopher L. Kuhlman
Applied Systems Analysis and Research
Sandia National Laboratories
PO Box 5800
Albuquerque, NM 87185-MS0747

David G. Robinson
Scalable Analysis and Visualization
Sandia National Laboratories
PO Box 5800
Albuquerque, NM 87185-MS1327

Stephen J. Bauer
Geomechanics
Sandia National Laboratories
PO Box 5800
Albuquerque, NM 87185-MS1033

W. Payton Gardner*
Applied Systems Analysis and Research
Sandia National Laboratories

*Now at: Geosciences
University of Montana
32 Campus Dr. #1296, CHCB 353
Missoula, MT 59812-1296

Abstract

This report presents efforts to develop the use of *in situ* naturally-occurring noble gas tracers to evaluate transport mechanisms and deformation in shale hydrocarbon reservoirs. Noble gases are promising as shale reservoir diagnostic tools due to their sensitivity of transport to: shale pore structure; phase partitioning between groundwater, liquid, and gaseous hydrocarbons; and deformation from hydraulic fracturing. Approximately 1.5-year time-series of wellhead fluid samples were collected from two hydraulically-fractured wells. The noble gas compositions and isotopes suggest a strong signature of atmospheric contribution to the noble gases that mix with deep, old reservoir fluids. Complex mixing and transport of fracturing fluid and reservoir fluids occurs during production. Real-time laboratory measurements were performed on triaxially-deforming shale samples to link deformation behavior, transport, and gas tracer signatures. Finally, we present improved methods for production forecasts that borrow statistical strength from production data of nearby wells to reduce uncertainty in the forecasts.

ACKNOWLEDGMENTS

This work was funded under the Sandia Laboratory Directed Research and Development (LDRD) Project Number 165670 and title "Appraisal of Hydraulic Fractures Using Natural Tracers." Lee Moo of Sandia National Laboratories was the Project Manager. A natural gas and oil producing company allowed us access for fluid sampling of two hydraulically fractured wells in a shale formation. We thank Kip Solomon and Alan Rigby of The University of Utah's Dissolved and Noble Gas Laboratory, who performed analytical measurement of noble gas compositions and isotopes of our field samples. Isotech Laboratories Inc. performed full gas chromatographic and stable carbon isotope measurements on our field samples. Several personnel of the Sandia Geomechanics Department assisted in development and execution of the tracer-release and deformation experiments.

CONTENTS

FIGURES

TABLES

NOMENCLATURE

JAGS	just another Gibbs sampler
LVDT	linear variable differential transformers
MS	mass spectrometer
ppm	parts per million
PTA	pressure transient analysis
QMS	quadrupole mass spectrometer
RTA	rate transient analysis
DOE	Department of Energy
R/R_a	the $^3He/^4He$ ratio of the measured sampled (R), normalized by the $^3He/^4He$ ratio of the atmosphere (R_a)
SNL	Sandia National Laboratories
W1	Well 1 of 2 for field noble gas sampling
W2	Well 2 of 2 for field noble gas sampling

1. INTRODUCTION

The characterization and prediction of subsurface fractures and their impact on fluid flow is a primary technical challenge in a variety of domestic energy production or related areas, including: shale-hydrocarbon production, enhanced geothermal energy production, and nuclear waste disposition in crystalline rock environments. Maximizing fracturing efficiency of stimulation techniques improves producible reservoir volumes and can mitigate risk to groundwater resources. Current fracture characterization by rate and/or pressure transient analysis (RTA/PTA), commonly used in the petroleum industry, assumes idealized geometries of fracture networks and transport properties (Clarkson, 2013), thus limiting knowledge of the actual fracture characteristics. Microseismic monitoring provides knowledge on the "stimulated reservoir volume" or the region affected by hydraulically fracturing that has become more permeable, but does not generate direct information on the fluid transport properties of the fracture network. Techniques to better appraise both the geometries, connectivity, and flow and transport properties of fractures and their interaction with the host matrix rock are needed. Diagnostic tools help reveal why the properties of a certain well or particular hydraulic fracturing treatments lead to the desired flow and transport properties or not.

This report presents efforts to develop the use of *in situ* naturally-occurring noble gas tracers to evaluate transport mechanisms and deformation, with a focus on shale hydrocarbon reservoirs. Noble gases are ubiquitous in geologic systems and have been used in many hydrogeologic studies to understand flow and transport (Mackintosh and Ballentine, 2012). The distinct major repositories or "reservoirs" of noble gases include the mantle, crust, hydrosphere, and atmosphere (Darrah et al., 2014). These noble gas sources have well-defined isotopic compositions of noble gases that allow identification of the origin of subsurface fluids and their mixing patterns. Noble gases are chemically inert, being affected predominantly by exchange between phases (e.g., solubility of noble gases between a liquid and gas), mass-dependent transport processes including diffusion, physical sorption of the heavier noble gases (e.g., krypton and xenon) as opposed to the lighter noble gases in sedimentary rocks, and patterns of fluid flow and mixing (Prinzhofer, 2013). Naturally-occurring *in situ* noble gases are promising as shale reservoir diagnostic tools due to their sensitivity of transport to: shale pore structure; phase partitioning between groundwater, liquid, and gaseous hydrocarbons; and deformation and release from hydraulic fracturing.

Specific work presented herein includes field and laboratory studies of noble gas tracers, combined with other standard data types, to evaluate subsurface transport mechanisms and deformation for a hydrocarbon-producing shale formation. Also included is work on methods for hydrocarbon production forecasts that borrow statistical strength from production data of nearby wells to reduce uncertainty in the forecasts. The field study included collection of a 1.5-year time-series of wellhead fluid samples immediately following the first gas production from two hydraulically-fractured wells (see Section 2). The noble gas compositions and isotopes of the samples suggest a strong signature of atmospheric contribution to the noble gases that mix with deep, old reservoir fluids. Complex mixing and transport of fracturing fluid and reservoir fluids occurs during production. Real-time laboratory measurements were performed on triaxially-deforming shale samples, from core from the same shale field site, to link deformation behavior, transport, and gas tracer signatures (see Section 3). The statistical methods used Bayesian techniques to investigate production data reported for horizontal Barnett gas wells in Texas (see Section 4). Three different examples are used to show the approach. Production forecasting is performed for 197 wells with the Arps and Duong models, six nearby wells are used to demonstrate the process of borrowing statistical strength to better characterize model uncertainty,

and predictions of estimated ultimate recovery are made, considering the uncertainty associated with the fit between the model and reported data.

This work also included extension of the multirate mass transfer model for pressure-driven flow, essentially a general extension of dual-porosity flow to an arbitrary number of porosities—hence termed "multiporosity" as the multirate extension of dual-porosity (Kuhlman et al., 2015). This model was developed to advance the ability of RTA/PTA methods to: better accommodate more realistic representations of fracture networks for flow modeling in low permeability systems; and form a potential framework for combining RTA/PTA with noble gas or other tracers. The resulting journal article (Kuhlman et al., 2015) is not included in this report as it is readily available in the literature. Also, while part of this work but not reproduced here, is the conference paper by Bauer et al. (2015) that reports on real-time helium mass spectrometry permeametry during triaxial deformation of shale samples. This conference paper presents information that was a part of activities that are reported in Section 3.

2. NOBLE GAS TRACING OF FLUID TRANSPORT IN SHALE: A FIELD STUDY OF TWO HYDRAULICALLY FRACTURED WELLS

2.1 Introduction

In situ natural tracers are useful diagnostic tools because they exist naturally in the environment and do not require injecting or adding them to natural systems to utilize them. Noble gases in particular have uniquely beneficial qualities, which make them especially useful among available natural tracers. Noble gases are chemically inert and therefore can provide a different measure of subsurface flow and transport properties than other tracers such as hydrocarbons, which are affected by sorption and biological, chemical, and oxidation reactions (Darrah et al., 2014). The distinct major terrestrial sources of noble gases include the mantle, crust, hydrosphere, and atmosphere (Darrah et al., 2014). These noble gas sources have well-defined noble gas isotopic compositions that allow identification of the origin of subsurface fluids and their mixing patterns. Noble gases are affected predominantly by exchange between phases (e.g., solubility of noble gases between a liquid and gas), mass-dependent transport processes including diffusion, physical sorption of the heavier noble gases (e.g., krypton and xenon) as opposed to the lighter noble gases in sedimentary rocks, and patterns of fluid flow and mixing (Prinzhofer, 2013). Noble gases have been used extensively for a variety of subsurface studies, including assessment of fluid residence times in groundwater systems, characterization of CO_2 behavior in subsurface storage applications, and characterization of conventional hydrocarbon and coalbed methane reservoirs (Castro et al., 2000; Zhou et al., 2005; Holland and Gilfillan, 2013; Prinzhofer, 2013).

Recent studies investigate the usefulness of noble gases in hydrocarbon-producing shale reservoirs and/or formations that overlie such shales to: identify the sources of hydrocarbons gases in shallow potable groundwater (Darrah et al., 2014); and determine the genetic fingerprint, origin, and history of hydrocarbon gases in shale in the Appalachian Basin (Hunt et al., 2012). We propose that in addition to these valuable applications, naturally-occurring *in situ* noble gases are promising for direct diagnostic tools for flow, transport, and deformation of the shale reservoir itself that can augment other methods such as pressure and/or rate transient analysis, production decline analysis, and microseismic methods. Noble gases are promising due to their potential sensitivity of transport to: shale pore structure (e.g., Knudsen transport versus Darcy flow); phase partitioning between groundwater, liquid, and gaseous hydrocarbons; and deformation and release from hydraulic fracturing and creation of fracture surface area. The natural noble gases exhibit a large range of mass from helium to xenon, which affects their relative solubility in different fluid phases and mass-dependent transport (e.g., diffusion as opposed to advection). Thus, patterns of relative isotopic compositions of a suite of light to heavy noble gas may reflect the mode of transport and partitioning processes as hydrocarbon fluids move within the fractured shale reservoir and transfer between the shale matrix and fractures. Such information may greatly improve understanding of coupled *in situ* flow, transport, and deformation during hydraulic fracturing and subsequent production.

In this Section we investigate *in situ* natural noble gas systematics immediately following hydraulically fracturing of two horizontal wells in the same hydrocarbon shale formation. Time-series of 50 fluid samples total (~25 per well) over the course of approximately 1.5 years were collected from these wells. Our original goal of obtaining these time-series was to combine natural noble gas compositions and isotopic signatures with production data to: diagnose reservoir transport processes and fracture properties (e.g., what are the transport mechanisms from matrix to fractures?); and improve production forecasting and prediction of estimated

reserves. We hypothesize that forecasting production and estimating hydrocarbon reserves may be improved by using natural helium, in particular, due to its relatively high concentration of ^{4}He in shale (from U and Th decay; Darrah et al., 2014), its high diffusivity compared to other subsurface gases, and thus its potential to deliver flow regime information relatively more quickly. The results of the time-series of noble gases indicate, however, that complex mixing of two different fluids is occurring—the fluids exhibit strong atmospheric and deep-old-crustal noble gas isotopic signatures, respectively. We infer that the atmospheric component of the noble gases represents the injected fracturing fluids and the crustal noble gas signature reflects the *in situ* reservoir hydrocarbon fluids (both liquid and hydrocarbon gases). Concentrations and isotopes of noble gases in the produced hydrocarbon gases alternate between having a strong atmospheric signature and a strong crustal signature through the entire 1.5-year time-series, suggesting that the presence of fracturing fluids at these wells persists with time. The alternation of the two types of signatures makes interpretation of reservoir flow mechanisms and production decline prediction difficult—we recommend continued noble gas sampling as the data appears to show that the alternating signals may be dampening. We suggest that a longer time series may obtain data that would be more amenable to our original goals. The impact of this work resides in providing the first (as far as the authors can tell from the literature) time-series of noble gases from hydraulically fracture wells that reflect early-time flow and transport behavior.

2.2 Methods and Materials

The two horizontal gas wells sampled for noble gas compositions and isotopes were completed in an actively producing shale hydrocarbon field at depths of 11,500 ft (the first well, called W1) and 12,100 ft (the second well, called W2) below ground surface. Each of these wells had approximately 5,000 ft long laterals. W1 was drilled, hydraulically fractured, and completed first, with samples first being collected in February 2014. W2 was similarly drilled and completed, coming on line with gas production in March 2014. Gas samples for noble gas analyses were collected in 300 cm^3 volume stainless steel spun sample cylinders with bellows-sealed valves. Gas samples were collected by oil company personnel downstream from the separator at both wells. Liquid hydrocarbon and groundwater samples were collected, also from the separator with backpressure-piston-type cylinders, but these were not analyzed due to incompatibilities with the noble gas laboratory's analysis process (the laboratory was not set up to extract noble gases from the liquid samples as readily as the gas samples). The filled gas cylinders were shipped by the oil company to the University of Utah's noble gas laboratory for analysis (Appendix A includes raw data from W1 listed in Table 1 and raw data from W2 listed in Table 2). The noble gas analysis was performed using a quadrupole mass spectrometer (MS) and a magnetic sector field MS. After their analysis, the samples were then sent to Isotech Laboratories Inc. for gas compositional analysis (by full gas chromatography) including hydrocarbons, and isotopic analysis of carbon isotopes of methane and ethane on select samples (Appendix A includes raw data from W1 listed in Table 3 and raw data from W2 listed in Table 4).

2.3 Results and Discussion

Both wells exhibit gas, water, and oil flow, with W2 having consistently higher gas flow rates (compare red lines in upper plots of Figure 1 and Figure 2). The predominant gas component is methane, followed by ethane and lesser amounts of other hydrocarbon gases, with generally constant mole fractions (approximately equal to vol.%) for each well, respectively, through time except for very early time (Figure 1). The peak gas production occurs within 2 months.

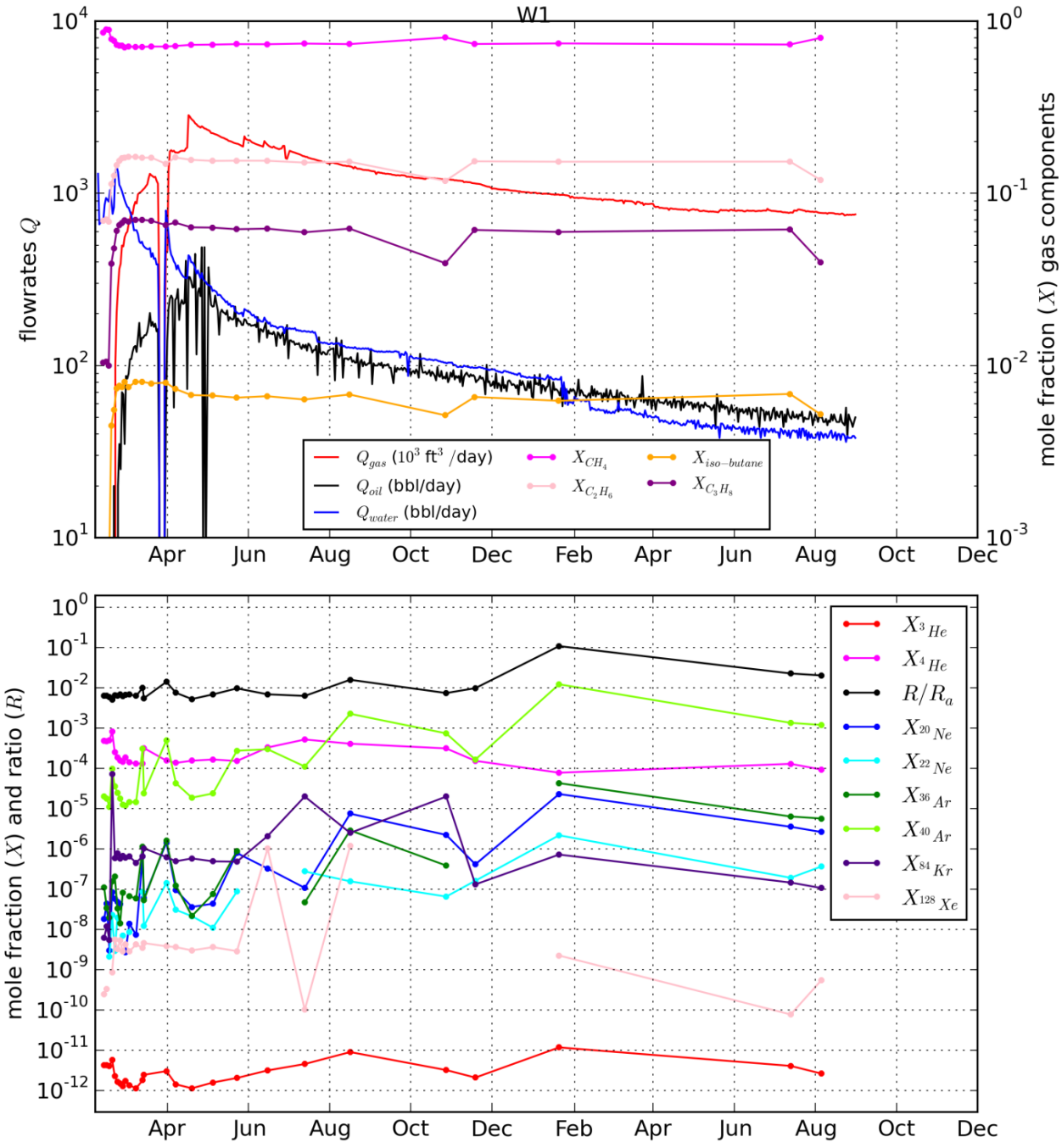

Figure 1. Well 1 (W1) data. Gas, oil and water flowrates and gas mole fractions in upper plot. Noble gas mole fractions in lower plot.

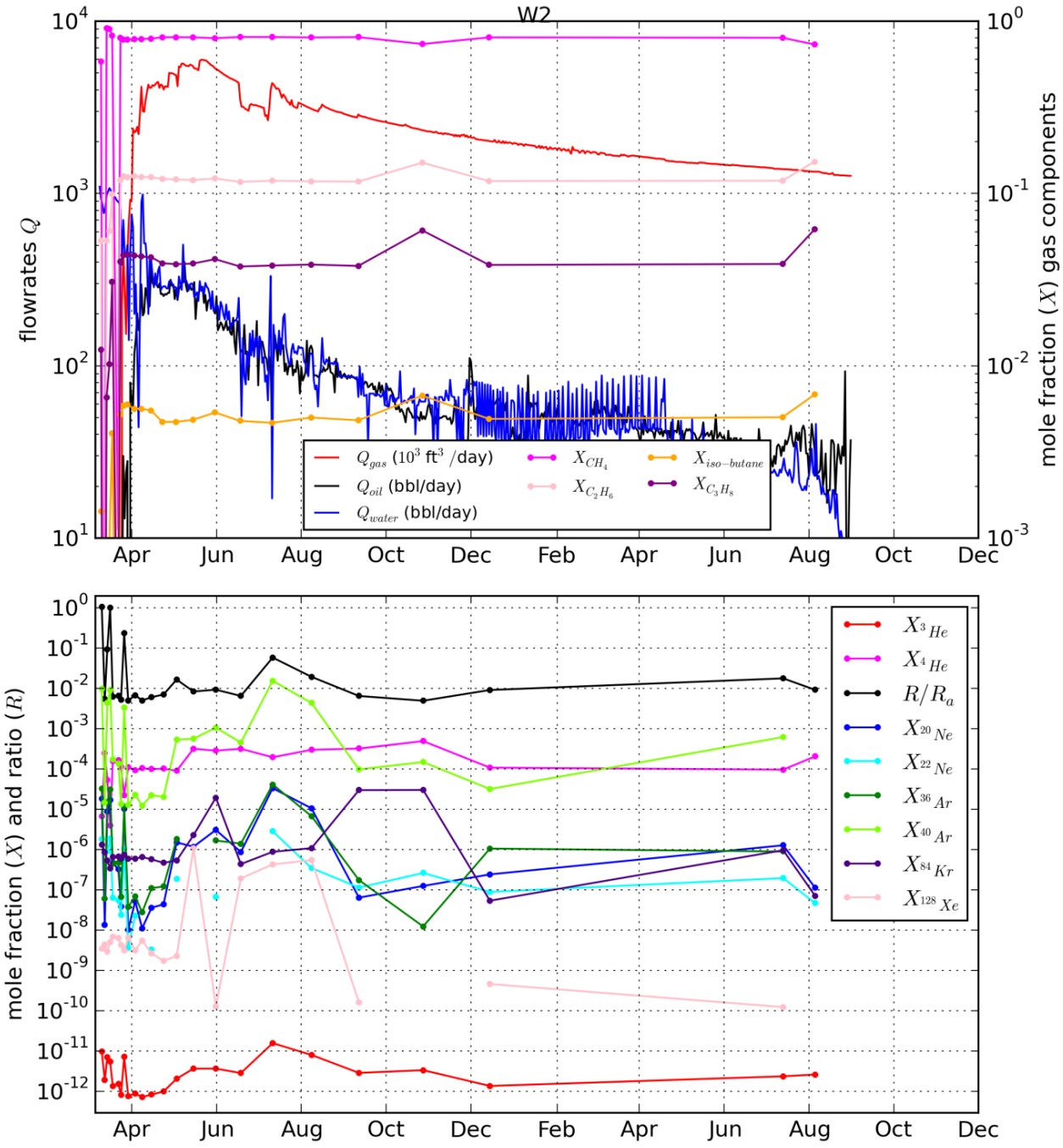

Figure 2. Well 2 (W2) data. Gas, oil and water flowrates and gas mole fractions in upper plot. Noble gas mole fractions in lower plot.

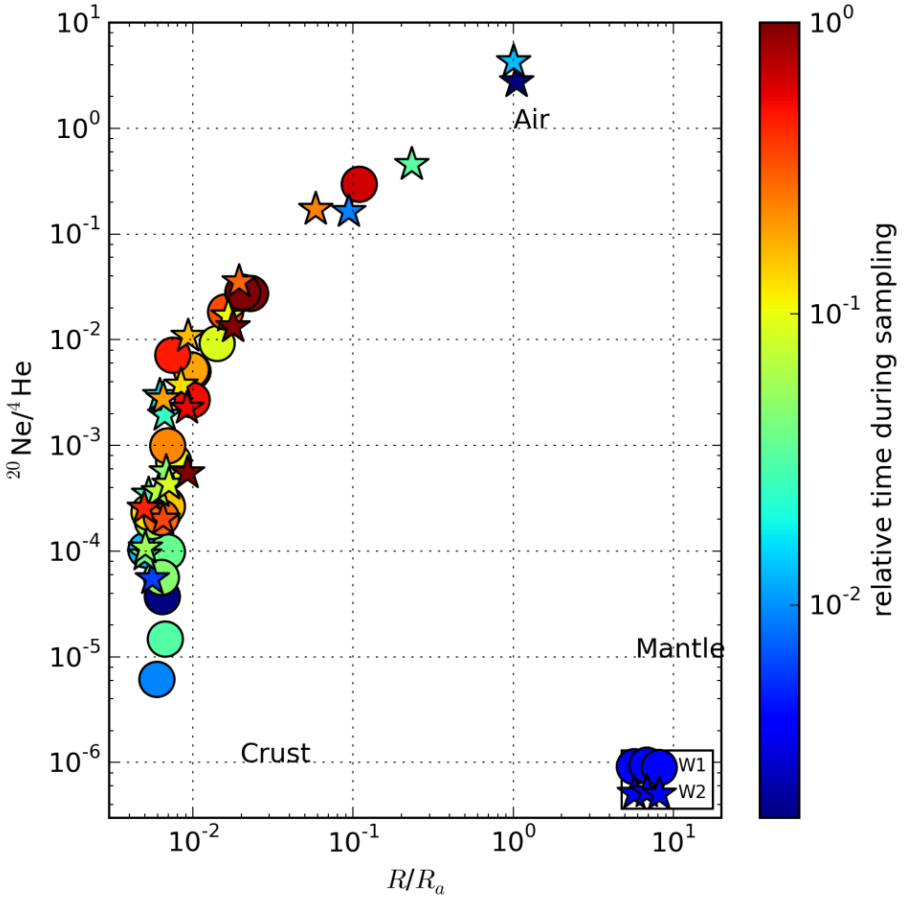

Figure 3. ^{20}Ne/4He versus R/R$_a$ for gas samples collected at wells W1 (circles) and W2 (stars), colored by their sampling time.

Figure 3 shows gas samples collected at wells W1 (circles) and W2 (stars) for the entire approximate 1.5-year time series. The R/R$_a$ ratio on the *x*-axis represents ^{3}He/^{4}He of the measured sampled (R), normalized by the ^{3}He/^{4}He ratio of the atmosphere (R$_a$)—thus, a value of one indicates that the sample's helium isotopic signature matches that of the atmosphere. The general isotopic signatures of atmosphere (air), crustal, and mantle are marked on the figure. The symbol color is related to the relative sampling time; blue symbols are early samples (soon after hydraulic fracturing and production began) and red symbols are late samples (recent 2015 samples after production has stabilized); the color scale is logarithmic (since samples were collected on an approximately logarithmic schedule).

Figure 3 shows mixing between the crustal endmember (lower left portion of figure) and the air endmember (upper middle of figure), which is believed to be related to noble gases coming from two "reservoirs" at depth. The primary reservoir is the shale, which is organic-rich and has high amounts of radiogenic isotope ^{4}He. The secondary reservoir is most likely the hydraulic fracturing fluid used in the completion of the well. It is believed the noble gases of the hydraulic fracturing fluid were comprised mostly of air-saturated water and entrained air (but these details are not available) pumped at very high flowrates and pressures into the formation. The gas being sampled at the wellhead is a mixture from these two reservoirs, but not a simple smooth mixing through time. The composition sampled at the wellhead appears to be jumping between the two endmembers (see lower subplots of Figure 1 and Figure 2 for time series of representative noble gases—also see the distribution of colors in Figure 3).

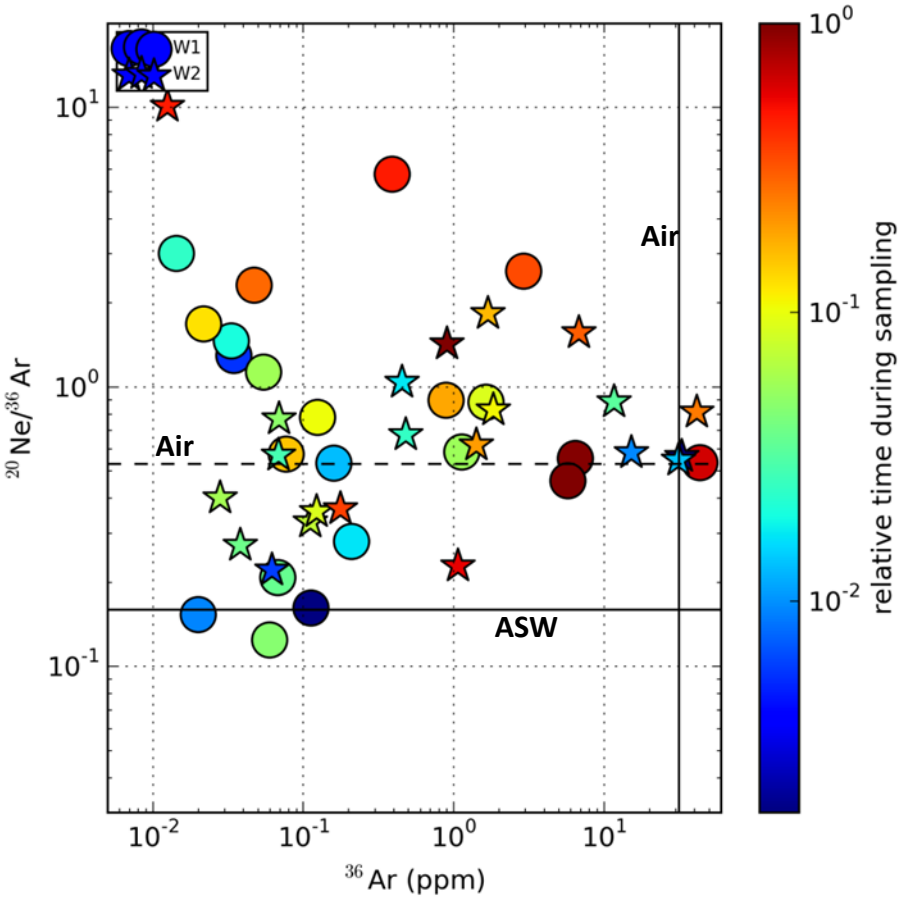

Figure 4. ^{20}Ne/^{36}Ar versus ^{36}Ar for gas samples collected at wells W1 (circles) and W2 (stars), colored by the relative time the samples were collected.

Figure 4 includes data from gas samples collected at W1 and W2, plotting ^{36}Ar mole fraction (converted to parts per million) on the *x*-axis and the ratio of ^{20}Ne to ^{36}Ar on the *y*-axis. The symbol types indicate the well, and the symbol color represents the time of sampling. Blue symbols are early, while red symbols are relatively late. The figure shows at larger ^{36}Ar mole fractions (right portion of plot) plot closer to the ^{20}Ne/^{36}Ar ratio associated with the atmosphere (see horizontal dashed line labeled "Air"). The data do not approach the ^{20}Ne/^{36}Ar ratio associated with air-saturated water (horizontal dashed line labeled "ASW"). The difference between these two lines is associated with the difference in the solubility of these two noble gases in water.

The coloring in this figure shows there is no clear trend associated with time since the well was completed. There is some "jumping" from high to low ^{36}Ar mole fractions, especially in W2; see the clustering of blue and red stars on the right.

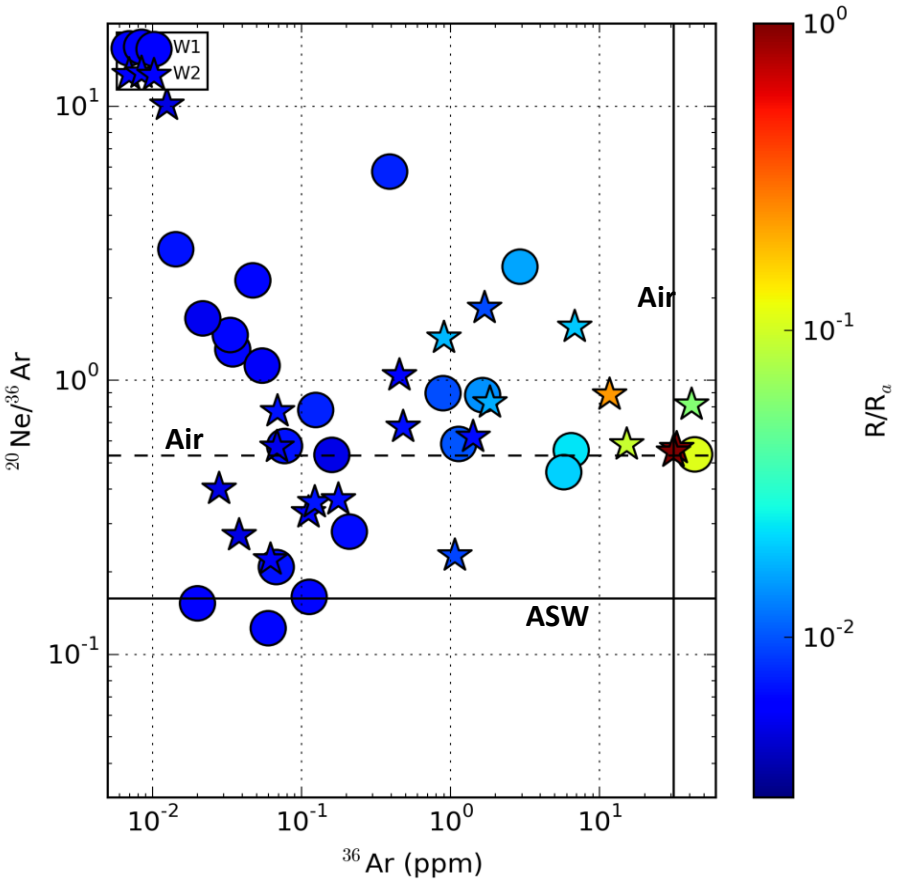

Figure 5. ^{20}Ne/^{36}Ar versus ^{36}Ar for gas samples collected at the wells W1 (circles) and W2 (stars), colored by their R/R$_a$ value.

Figure 5 shows the same data plotted in Figure 4, but the coloring indicates the R/R$_a$ value. In this figure the colors show a much stronger trend than the symbols colored by sampling time in Figure 4. Blue symbols are on the left portion of the figure and the lighter blues to reds plot on the right portion of the figure. The same mechanism that is increasing the ^{36}Ar mole fraction is likely also increasing the R/R$_a$ ratio, and causing the ^{20}Ne/^{36}Ar ratio to approach that of air. This is likely a mixing of reservoir fluid and air from the hydraulic fracturing process.

The exact mechanism that is causing this mixing of air with the reservoir gas in a non-uniform manner through time is not well known. Several factors may contribute to this effect, including the 1) mixing of gases produced from multiple hydraulically fractured stages, 2) release of bubbles of nearly atmospheric air held immiscibly in the formation, or 3) some "bubble" of reservoir air in the well or well casing that is slowly leaking back into the production tubing.

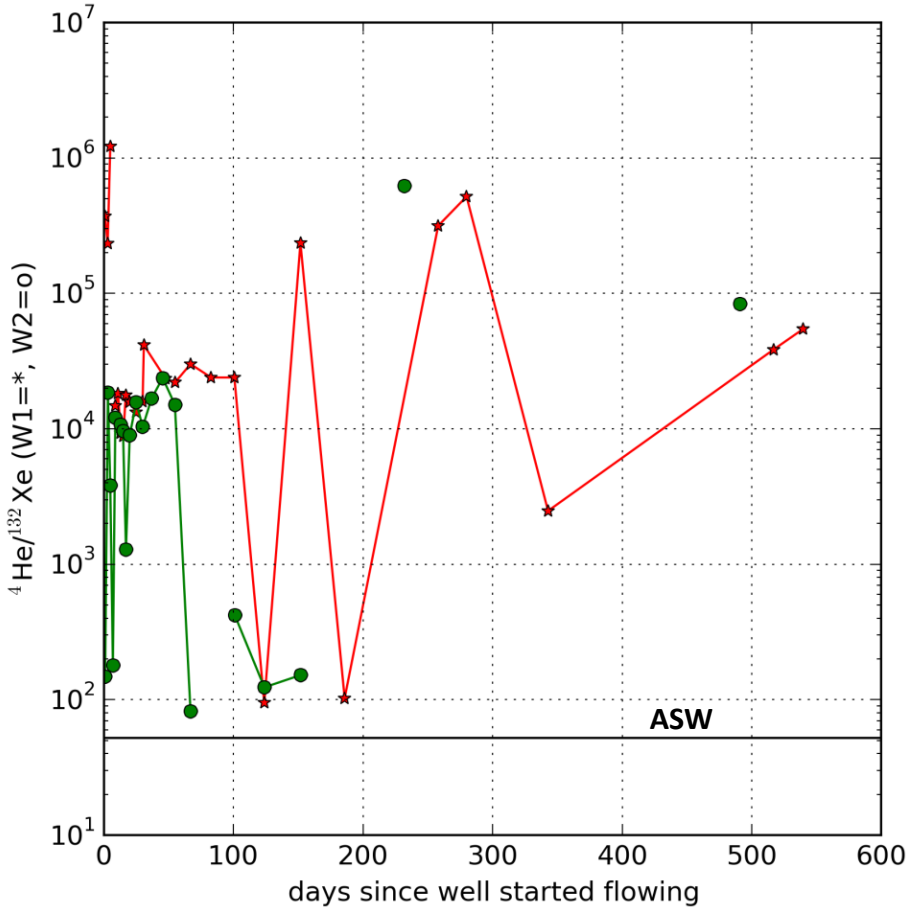

Figure 6. ^{4}He/^{132}Xe versus sample time for the wells W1 (red stars) and W2 (green circles).

Figure 6 shows a plot of the ratio ^{4}He/^{132}Xe through relative time at both wells. Helium-4 is a small inert crustal (i.e., radiogenic) gas, present in higher concentrations in the subsurface than in the atmosphere. Xenon-132 is a large sorbing atmospheric gas, contributed from the atmosphere and not generated at depth. The horizontal line labeled "ASW" represents the predicted ratio of these gases for water in equilibrium with the atmosphere. Gaps in the data (where the laboratory could not reliably report at ^{132}Xe value—see "nd" reported in Table 1 and Table 2) are indicated by a missing data point and a break in the connecting line.

Although there is significant variability in the data (e.g., data points near the ASW line for both wells), there is a possible upward trend observed in both wells. The ratio goes from approximately 10^4 to nearly 10^5 over the 1.5 years of sampling. Some of the noise in this ratio is due to the low mole fractions of xenon in the sample (generally less than 10^{-8}) contributing to higher signal-to-noise ratio in the reported results. This trend could represent the faster transport of helium, relative to xenon, but this is not definitive.

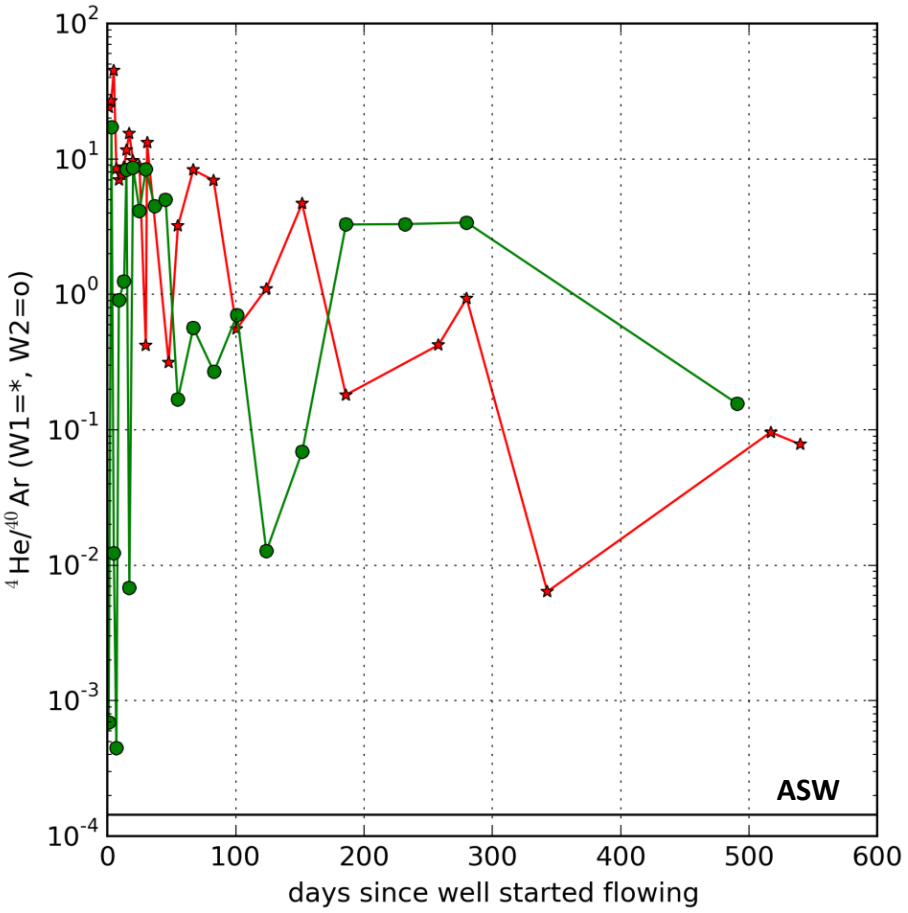

Figure 7. $^4He/^{40}Ar$ versus sample time for the wells W1 (red stars) and W2 (green circles).

Figure 7 shows a plot of the ratio $^4He/^{40}Ar$ through relative time at both wells. Helium-4 and ^{40}Ar are inert crustal (i.e., radiogenic) gases. The horizontal line labeled "ASW" represents the predicted ratio of these gases for water in equilibrium with the atmosphere. Although there is significant variability in the data, there is a possible slight downward trend in both wells with time. The ratio goes from near 10 at completion to approximately 0.1 in both wells at 1.5 years. This trend could represent an early peak of helium (due to its relatively smaller size and higher diffusivity), followed by a delayed peak in argon (due to its larger size and lower diffusivity)—see Figure 1 and Figure 2 for time-series of individual mole fractions.

2.4 Conclusions and Recommendations

In general the field noble gas data collected from the two gas wells was insightful but very noisy, with some significant temporal gaps in data due to a confluence of both sampling and laboratory issues. This shows the method holds promise, but suggests possible improvements to future sampling strategies.

Future testing ought to be conducted in gas wells with different gas/water and gas/oil ratios. Particularly the interpretation of a noble gas time-series may be simpler in a "dry" gas well. The wells sampled were considered "wet" wells because they had significant condensate (i.e., oil production from the separator—see black lines in upper plots of Figure 1 and Figure 2). The effects the separator has on the noble gases is difficult to quantify and understand; sampling a well before the separator or from a well without a separator may pose challenges related to high-pressure sample collection, but this should be considered more explicitly in any future sampling efforts.

Quantification of the noble gas composition and volume of the hydraulic fracture fluid would also improve the interpretation of the data. Currently, the contribution from the frac fluid is purely based on conjecture, with no data currently available. Depending on the cooperation from participating oil companies, it might be possible to "spike" the frac fluid with a noble gas that would more clearly and definitively show up in the results. This is already performed in some gas wells with other types of tracers, but the unique characteristics of noble gases might make their use as introduced tracers meaningful as well.

These two wells also produced some H_2S, which makes them "sour", requiring addition of a "sweetener" to the stream of gas at the separator. The exact schedule of sweetener addition and even the exact composition of the sweetener are unknown. Characterizing these factors would help to reduce uncertainty; the effect on the noble gases is likely small but unknown.

It may be advantageous to study simpler systems first (e.g., other variations on the lab testing presented in the next chapter) to understand the behavior of noble gases in these systems, and in the "engineering" portions of the gas wells (i.e., the tubing, separator, and sweetener). Modeling of noble gas partitioning and behavior in the wellbore and separator may be fruitful in the future (given more information about this). Efforts to simulate the noble gas release mechanisms in the shale reservoir were confounded by the overprinting of the mixing between the "air" and "formation" sources of the noble gases. Duplicate samples, analyzed in different labs, would help to reduce uncertainty and produce more robust data in the face of possibly leaky containers and laboratory errors or mishaps.

3. APPLIED AND NATURAL TRACER RELEASE DURING SHALE DEFORMATION: EXPERIMENTAL VALIDATION

3.1 Introduction

This work describes an initial laboratory validation study of a technology that monitors natural tracer release during deformation of shale. Naturally occurring radiogenic ^{4}He is present in high concentration in most shales. During deformation, accumulated helium can be released as new transport pathways are created. We present the results of an experimental study in which confined reservoir shale samples, cored parallel and perpendicular to bedding—some of which are initially saturated with helium to simulate reservoir conditions—are subjected to triaxial compressive deformation. A second set of shale samples from the same shale formation as Section 2 are monitored for gas release using a quadrupole mass spectrometer (QMS). During the deformation experiment, differential stress, axial, and radial strains are each systematically tracked. Release of helium and other gases is dynamically measured using a helium mass spectrometer leak detector and/or QMS. Our results show that accumulated helium is released as a function of shale deformation. QMS-determined gas release rate appears to change post deformation. These first measurements of dynamic helium release from rocks undergoing deformation show that helium provides information on the evolution of microstructure as a function of changes in stress and strain.

^{4}He continuously accumulates in mineral grains, and adjacent pore fluids due to alpha decay of naturally occurring U and Th. The transfer of helium from rock grain to the pore fluid and the transport within the porous media is a function of the pore network distribution and thus coupled to the state of stress. Changes in the distribution and flow of helium in the subsurface can, perhaps, provide information on changing states of stress and strain in the subsurface. We propose that one possible application of that phenomenon is development of a scheme to quantify structural evolution of shale during deformation.

The fine-grained nature of shale and associated narrow pore throat diameters significantly limit fluid flow and can lead to non-Darcian phenomena such as molecular sieving and species-dependent permeability. Shale pore structure is hierarchical, with 100-nm pores in organic kerogen pockets and sub-micron-cracks in the inorganic complement (Slatt and Abousleiman, 2011; King, 2010; Loucks et al., 2009; Dewers et al., 2012). The pore structure and fabric of shale and mudstone, absent of fractures lends itself to low permeability (Brace, 1980), in the nano-darcy range. Kwon et al (2004) provide a thoroughly referenced review of shale permeability indicating that laboratory measurements on shale, mudstones, and clay aggregates vary widely 10^{-16} to 10^{-23} m^2. The permeability variations are linked to rock properties (porosity and grain size) and test stress conditions. Kwon et al. (2004) indicate that composition (clay content specifically) and fabric may cause anisotropy in flow properties. Grain shape alignments, which are pronounced in shales, lends to anisotropic flow properties (e.g. Bennett et al., 1989).

The variation of permeability of shales has been found to depend on porosity (e.g. Katsube et al., 1991, Dewhurst et al., 1998, 1999), grain size and pore distributions (e.g. Morrow et al., 1984., Dewhurst et al., 1998, 1999), and the hydrostatic pressure (e.g. Morrow et al., 1984., Katsube et al., 1991, Dewhurst et al., 1998, 1999). Clay mineral content at a given porosity impacts permeability (e.g., Dewhurst et al., 1998, 1999). Permeability of shale decreases with increasing effective pressure (e.g., Metwally and Sondergeld, 2011) and increasing pressure has been shown to decrease the permeability anisotropy in shale (Kwon et al, 2004). Shearing tends to decrease permeability across an experimental shear zone (Ikari et al, 2009).

Popp and Salzer (2007) studied dilatancy in Opalinus Clay and developed conceptual models relating porosity changes, stress-induced deformation, permeability, and V_p and V_s. Their discussion seeks to relate these independently measured physical parameters with compactive, dilatant, and failure behavior of this clay rich rock. Zhang and Rothfuchs (2008) related permeability changes in clay to the onset of dilatancy.

Nicolas et al (2014) measured emanation of radon as function of stress-strain state during laboratory experiments of granite. The radon release was correlated to acoustic emissions and P- and S-wave velocity measurements and microstructural evolution. In their experiments, argon was used to flush radon from the samples at strain intervals. Similarly, the release of radon from tuffs undergoing deformation (Tuccimei et al, 2010) was reported for samples during deformation—this was an experiment in which the release of naturally occurring gas tracers was observed continuously throughout a controlled deformation experiment.

The release of helium and other geogenic gases during rock deformation could provide information on the evolution of micro and macrostructure within the rock, and/or changes in the state of stress and strain. The amount of gas liberated is dependent upon the amount present and that made accessible during deformation; the latter is a function of the created fracture surface area. Gas is released during fracture and deformation due to comminution of mineral grains, liberation of gas stored along grain boundaries, and diffusion from the mineral to the newly formed fracture.

Here we present the first continuous observations of helium released from shale specimens undergoing deformation. Our results indicate that helium flow and/or release provides a sensitive measure of pore interconnectivity during deformation and could provide a potential signal providing information on changes in stress and strain in shale formations. Changes in fluid flow in shale and/or mudstone during stress evolution could be important in monitoring subsurface seals for CO_2 sequestration, conventional oil and gas reservoirs, compressed air storage, and nuclear waste disposal where the low shale permeability is relied upon to create a flow barrier.

3.2 Experimental Procedures

Specimens for this study were shale sub-cores taken from 4” drill-hole core. Specimens were cored perpendicular to bedding and parallel to bedding. The specimens were within about 10 cm of each other. The average composition of nearby shale samples is 36% clay minerals, 30% quartz, 19 % calcite, 10 % feldspars, and 5 % other constituents. The average porosity is around 5%.

Test specimens were 2.5-cm diameter by 5.08-cm length right circular cylinders. Specimens had a porous frit on each end to facilitate gas flow in and out and were jacketed with thin layers of paint-on ultraviolet-cured epoxy which bonds tightly with the rock. Jacketing assures contact between the sample and the jacket. Representative blank tests using aluminum cores and this jacketing, using helium flow measurements determined a low end permeability of approximately 9×10^{-25} m^2.

Axial and radial displacement was recorded with a combination of resistance strain gages and/or (LVDTs) (Figure 8). LVDT displacement measurements are representative of a greater volume of rock than resistance gages; however, resistance strain gages sense strain differences due to heterogeneous mineralogy, grain size distribution, etc. in specific locations. Radial LVDTs were

mounted near mid-height and quarter height (Figure 8) providing two point measurements of radial displacement across the diameter. These measurements are tracked separately. Generally, the center LVDT displacement is used to calculate radial and volumetric strains. Using the radial displacement measurements one can also calculate the sample area as a function of applied pressure and force and stresses may be calculated. Axial displacements are measured by LVDTs mounted to the specimen end caps. If two or more (redundant) displacement measurements are made, they are averaged.

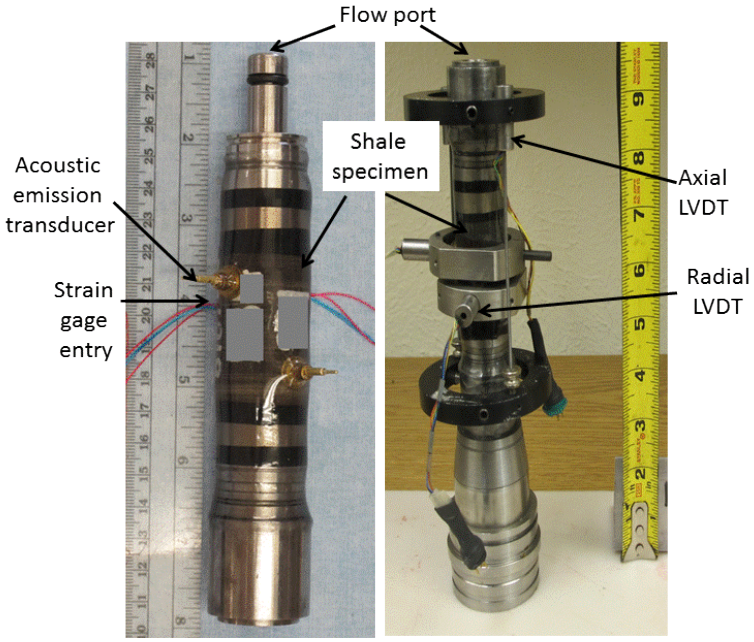

Figure 8 . Strain gaged sample (left); LVDT instrumented sample (right).

For helium release experiments, reagent grade helium is introduced to the specimen through flow ports in the end caps using O-ring connections. VCR fittings were used for the positive pressure helium flow and vacuum connections (Figure 9). Vacuum line protection from jacket failure is ensured with low pressure, vacuum relief valves and an expansion volume capable of containing the hydrostatic fluid volume expanded to 1 atmosphere. Helium flow rate release from the sample is measured using a mass spectrometer helium leak detector (Lee and Bauer, submitted 2014; Bauer et al, 2015). Prior to each test the helium flow leak detector was calibrated using a calibrated standard leak.

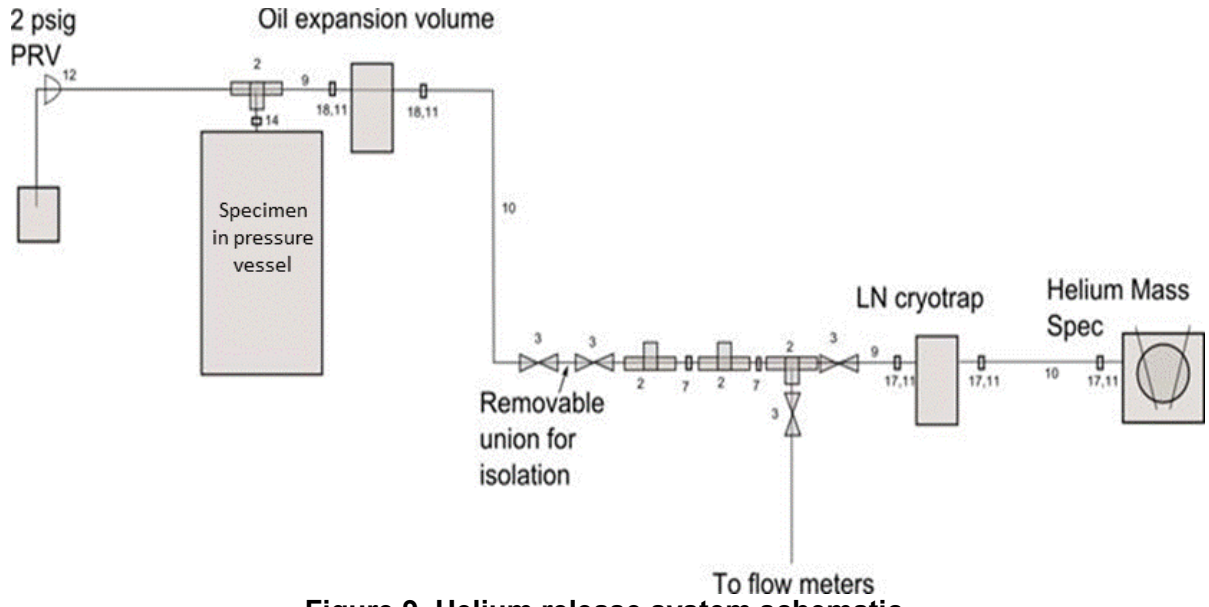

Figure 9. Helium release system schematic.

Tests were performed in the Sandia National Laboratories Geomechanics Laboratory under ambient conditions (~21°C and ~10% relative humidity). Specimens were tested in a 70 MPa pressure vessel which was placed within a 1.0 MN (225 KIP) testing system/load frame.
For the helium release experiments, jacketed specimens (Figure 8) were placed in the pressure vessel (Figure 10) and the hydrostatic pressure (20.7 MPa for all tests) applied. The confining pressure (σ_3) was applied by a servo-hydraulic pressure intensifier, which was plumbed into the pressure vessel. The load frame supports application of the maximum principal stress (σ_1) via a piston through the lid of the pressure vessel (Figure 10). After the specimen/pressure vessel system was assembled and placed into the load frame the pressure vessel was filled with confining fluid (Isopar H®). The confining pressure was maintained at approximately 20.7 MPa while the specimen was saturated with pore fluid (He). Prior to deformation helium was flowed through the sample for at least 48 hours at 100 psi inlet pressure to enrich the pore fluid in helium.

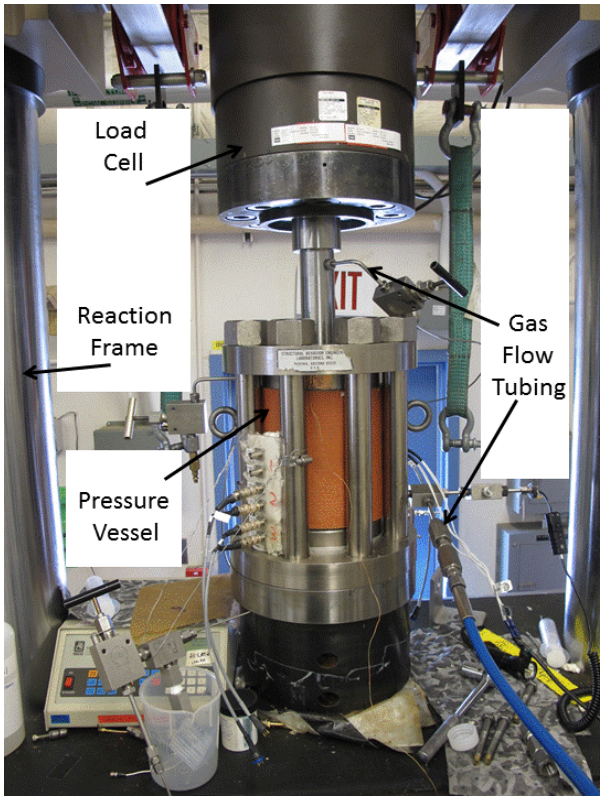

Figure 10. 1.0 MN testing system; reaction frame, 70 MPa pressure vessel, flow system tubing.

For QMS and helium flow measurements, either a quadrupole mass spectrometer or helium leak detector (a mass spectrometer which measures only helium presence/flow) is used in conjunction with the triaxial deformation apparatus (Figure 11). This test configuration required system design and set-up to accommodate physical safety and delicate equipment preservation concerns of the high precision analytical device in the vacuum line. Pressure relief valves and expansion tank volumes are part of the vacuum line and require vacuum seals.

During the QMS and helium flow measurement tests, the strain-gaged shale sample is first confined and in Test 1 gas release is measured using the QMS at 3.45 MPa confining pressure for ~10 hours, then helium is flowed through the sample ~12 psi upstream and vacuum downstream and flow rate is measured as pressure is increased in steps to 34.5 MPa. Then the sample is reconnected to the QMS and gas release is measured prior to, during, and after the triaxial deformation of the sample.

In Test 2 gas release is measured using the QMS at 3.45 MPa confining pressure for ~80 hours, then helium is flowed through the sample ~12 psi upstream and vacuum downstream and flow rate is measured as pressure is increased in steps to 34.5 MPa. Then the sample is subjected to triaxial compression, while flow is continuously measured. Then confining pressure is cycled repeatedly down to 21 MPa and back to 34.5 MPa with hold periods at each level.

Two experiments of this type were performed on shale samples cored parallel to bedding. The samples supplied were of a less than optimal length (~20% short), and the 2 samples tested arrived with a bedding parallel fracture. The fracture was glued into position from the outside (no glue was put on the fracture surface). Because the samples were short, and contained a fracture, the triaxial test data should be considered qualitative and not quantitative.

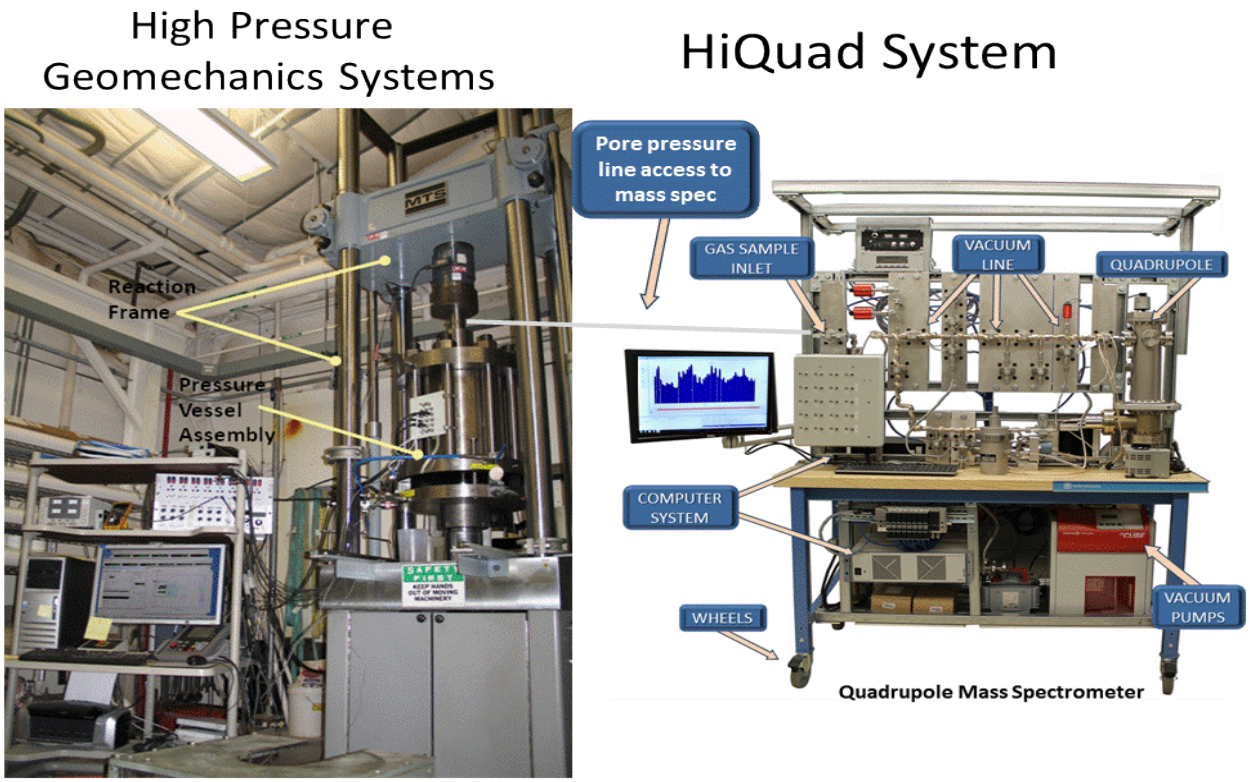

Figure 11 . High pressure geomechanics test system connected to quadrupole mass spectrometer.

During experiments, confining pressure is controlled, measured and tracked using a pressure transducer located in the intensifier connection line about a meter from the pressure vessel. Axial force is measured external to the pressure vessel and O-ring friction is corrected for during data analysis. Specimens were deformed using a controlled displacement mode and shortened at a rate of 5×10^{-6} s^{-1}. Force, displacement, confining pressure, and helium flow were recorded in an automatic data acquisition system as a function of time. A small amount of data was reviewed in order to provide reasonable confidence that the confining pressure conditions would result in elastic mechanical behavior.

Here we report the results of three different helium release tests with different boundary conditions and/or core orientation. The three combinations of axial loading orientation (parallel versus perpendicular to bedding) and experimental boundary conditions are explained below.

Experiment SSP1: Specimen cored parallel to bedding, and initially saturated by flowing helium through the sample at an inlet pressure of 0.345 MPa. Prior to the start of deformation, the upstream end of the specimen was valved off, and the vacuum was applied to the downstream end, leaving a volume of helium at 0.345 MPa in the upstream tubing between the valve and the top of the specimen. During the test vacuum was applied only to the downstream end of the sample.

Experiment SSP2: Specimen cored parallel to bedding and initially saturated by flowing helium through the sample at an inlet pressure of 0.345 MPa. After saturation and prior to deformation inlet pressure was relaxed to 0.1 MPa. During the test vacuum was applied to both sides of the specimen.

Experiment SSP3: Specimen cored perpendicular to bedding and initially saturated by flowing helium through the sample at an inlet pressure of 0.345 MPa. After saturation and prior to deformation inlet pressure was relaxed to 0.1 MPa. During the test vacuum was applied to both sides of the specimen.

3.3 Experimental Results

3.3.1 Helium release tests

Figure 12, Figure 13, and Figure 14 show the stress strain response for SSP1, SSP2, and SSP3, respectively. The compressive strength of the three samples is similar and ranges from140 to 150 MPa. The axial strains vary from near 0.01 to just greater than 0.02. Because the effective confining pressure is essentially identical for all tests, the differences in strains are attributed to mineralogical and textural variations between specimens. It is interesting to note that SSP1 and SSP2 (shortened parallel to bedding) show a concave down axial stress-strain curve for differential stresses less than ~40 MPa, whereas SSP3 (perpendicular to bedding) exhibits concave up behavior at differential stresses less than ~40 MPa.

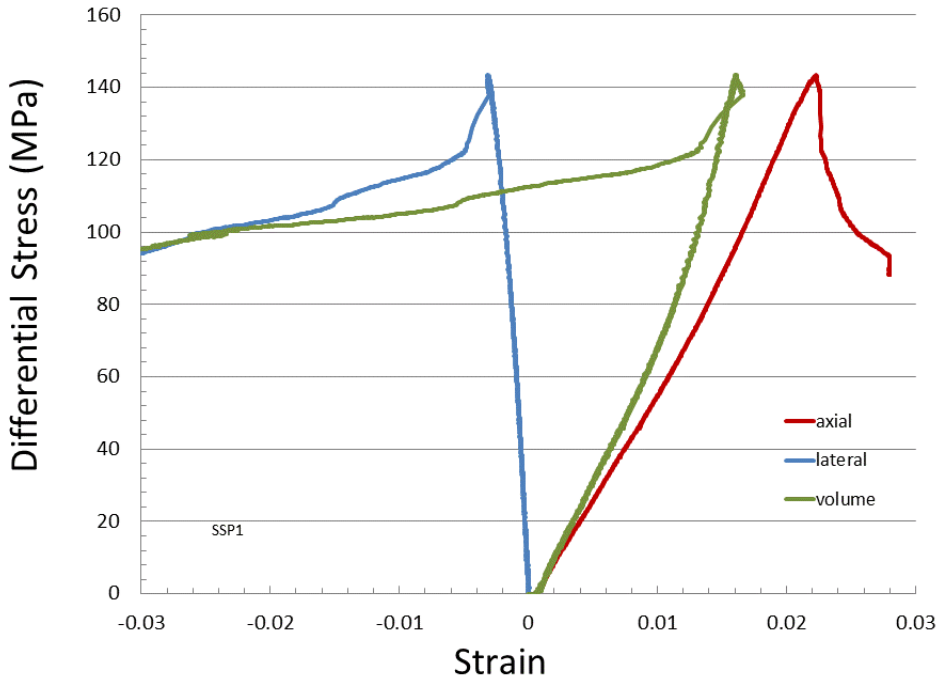

Figure 12 . Differential stress versus strain SSP1.

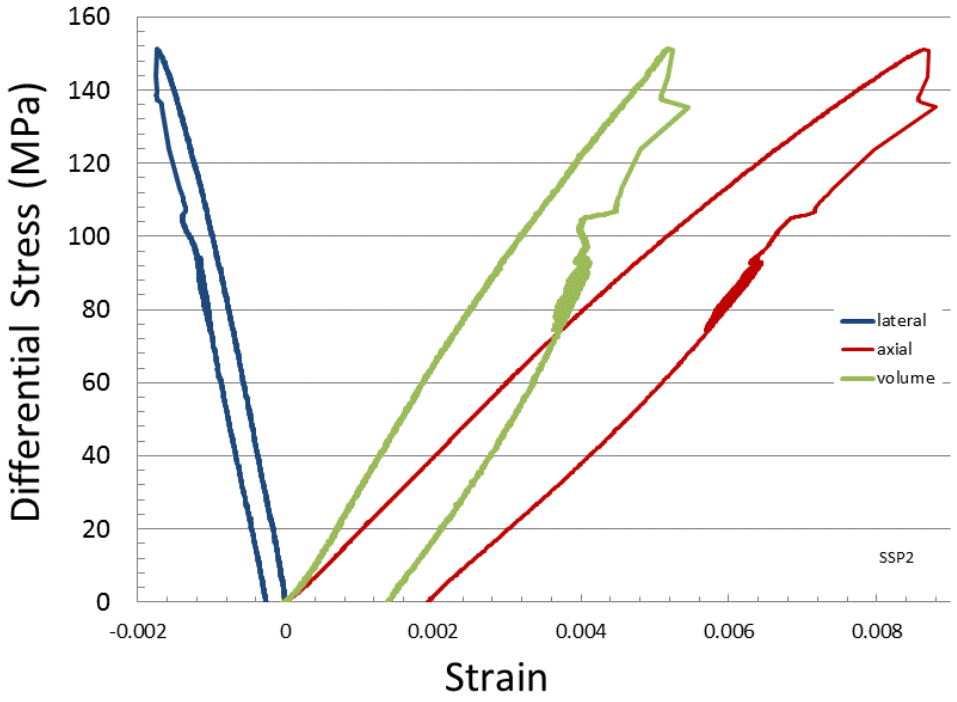

Figure 13. Differential stress versus strain SSP2.

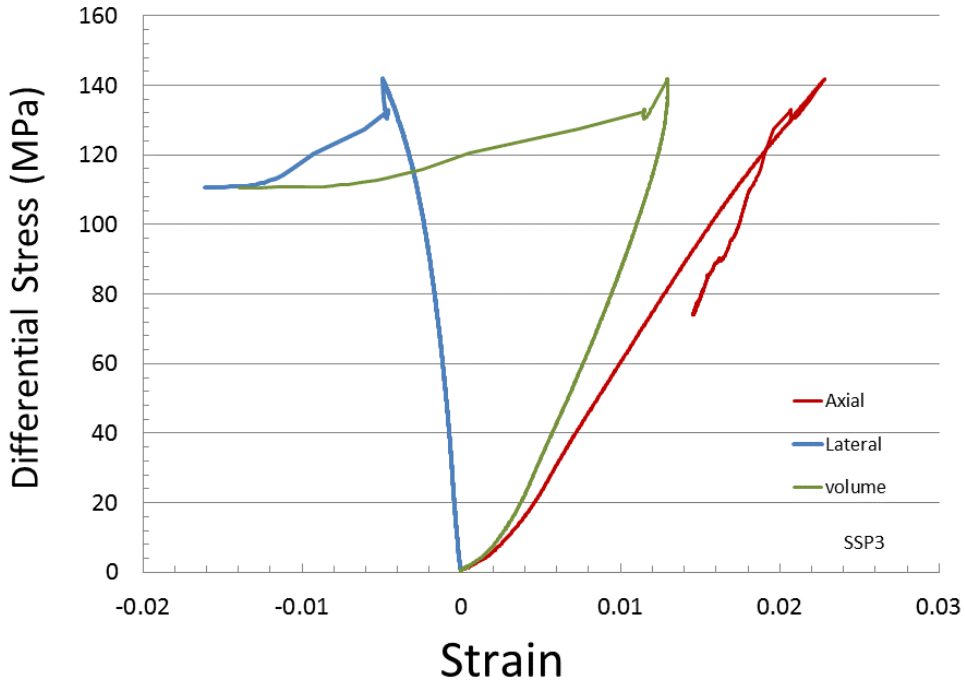

Figure 14. Differential stress versus strain SSP3.

Observations of deformation and fractures were made on surfaces created by careful wire sawing of deformed specimens along the specimen long axis perpendicular to the apparent dominant macrofractures. Within SSP1 (Figure 15) there is pervasive fracturing in a combination of axial subparallel and angled fractures. The fractures intersect and cross each other and strike parallel or at small angles to bedding. Fracturing is more numerous at the specimen ends, and longer fractures terminate at the specimen ends.

Within SSP2 (Figure 16) long, angled fractures dominate. The fractures tend to terminate at the specimen end or each other; again, fractures dominantly strike at low angles to bedding. SSP2 contains fewer fractures than SSP1.

Within SSP3 (Figure 17), the macro deformation is quite different in character to SSP1 and SSP2 and is concentrated near the specimen top. The fractures (black arrows) terminate at the specimen top end and along the side edge near the top, and are at a greater angle to the long axis. In close observation, it appears that fractures are lower angled near the specimen top and as they approach the side boundary. The effect of strong material anisotropy is apparent in the observed deformation.

Coarse grain deposits are identified in SSP3. Small pockets of coarser grained minerals are identified by blue arrows in Figure 17, and appear to be small scale sedimentary channels, creating mini-reservoirs in the rock. Coarsening sequences produce areas of finer and coarser material in the core, which appear to have different mechanical properties. The red arrow points to an interface between fine (above) and course (below) material in which the fracture angle(s) are refracted as it progresses through the specimen.

Figure 15. Deformed specimen SSP1.

Figure 16. Deformed specimen SSP2.

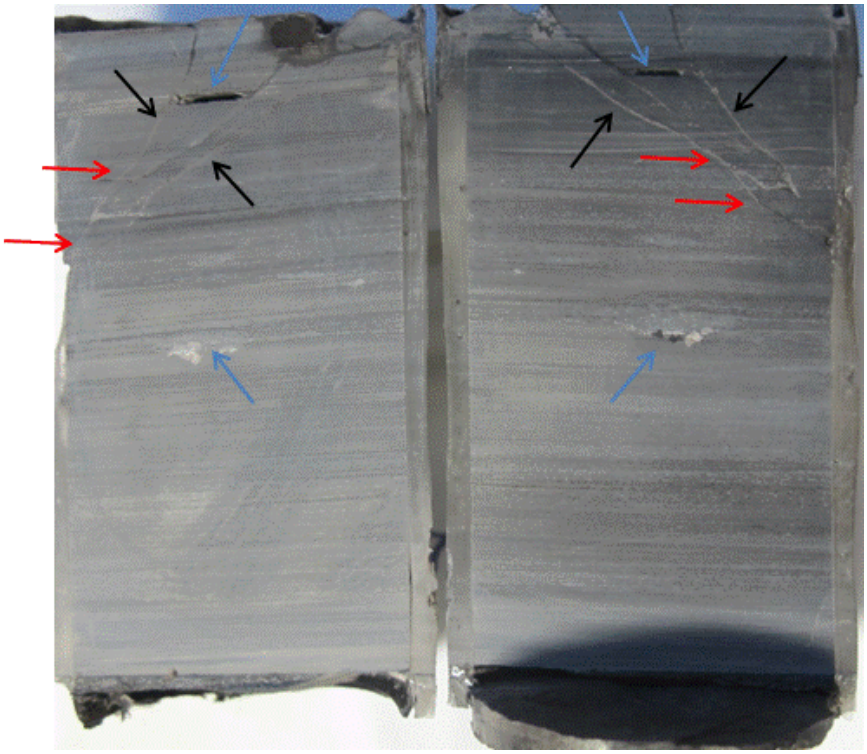

Figure 17. Deformed specimen SSP3 where blue arrows point to course pockets of sediment; black arrows indicate major fractures which terminate at the specimen end; red arrows point to fractures which refract (change direction) as fractures pass through fine and coarse material.

3.3.1.1 Flow Versus Strain Response

Volume strain and helium flow versus time are plotted in Figure 18 through Figure 23. For each specimen, the first plot represents most to all of the experiment, and the second plot represents the hour or so of intense activity of flow and deformation. The plots do not all start at zero because test procedures collected data changes when they commenced as opposed to when the testing began. Although specimens are shortened at a relatively constant rate, displacements observed near and post failure happen quickly.

For SSP1 (Figure 18 and Figure 19), helium release rate (flow) decreases with time for most of the compression stage of deformation consistent with draining of the pore space to the vacuum. Towards the end of the compression phase a slight increase in release rate is observed, followed by a sharp rise. Peak in flow around 6×10^{-4} is observed followed by a subsequent monotonic decrease in flow. Volume strain increases with increasing time as the specimen compacts, and then decreases slightly, and then decreases dramatically, then levels off. Figure 19 shows a 3000 second segment of the experiment around the fracture event. In it, the flow rate remains relatively stable and volume strain increases with increasing time during the compression phase.

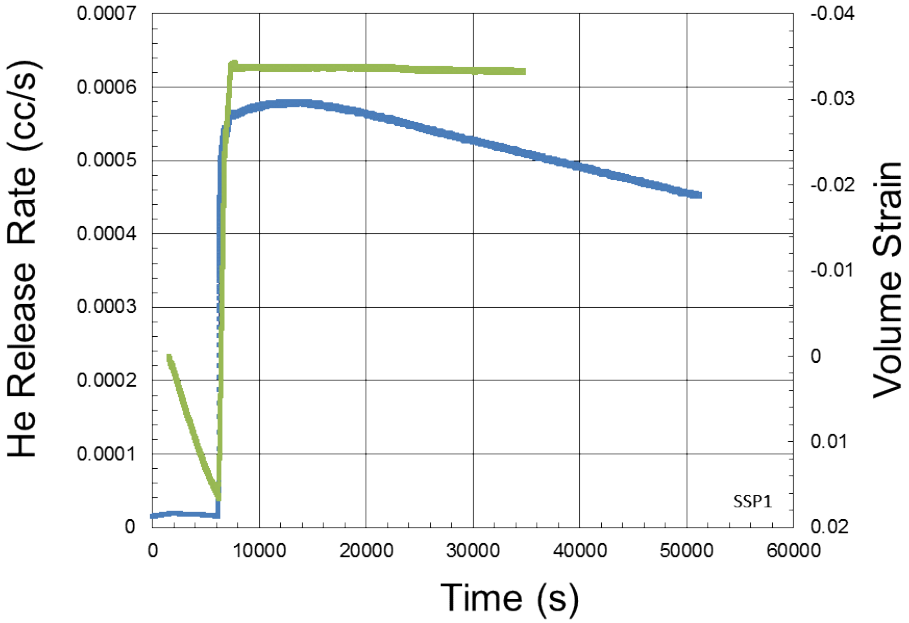

Figure 18. Helium release rate and volume strain versus time (SSP1).

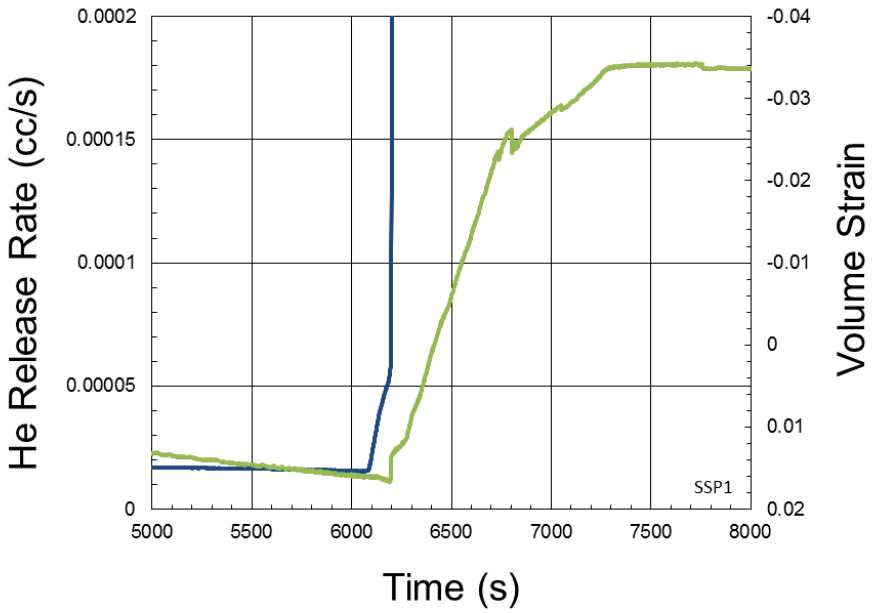

Figure 19. Helium release rate and volume strain versus time; close up view (SSP1).

A similar pattern is observed in SSP2 (Figure 20 and Figure 21). Helium release rate (flow) decreases with increasing time during the majority of the compression phase (steadily increasing volume strain). Between 5000-6000 s the flow rate begins to increase slightly. At 6000 s a sharp increase and peak flow of around 7×10^{-4} cc/s occurs followed by monotonic decrease in flow. For early times volume strain increases steadily with time consistent with compaction, at 6000 s the volume strain decreases sharply (this is when the specimen loses axial strength), and then increases dramatically consistent with dilation during fracturing, then levels off. Figure 20 shows a 4000 second segment of the experiment around the fracturing event. At 6100 s the flow rate begins to rapidly rise, and it is clear that flow rate begins to increase *before* macroscopic dilation occurs (volume strain begins to decreases).

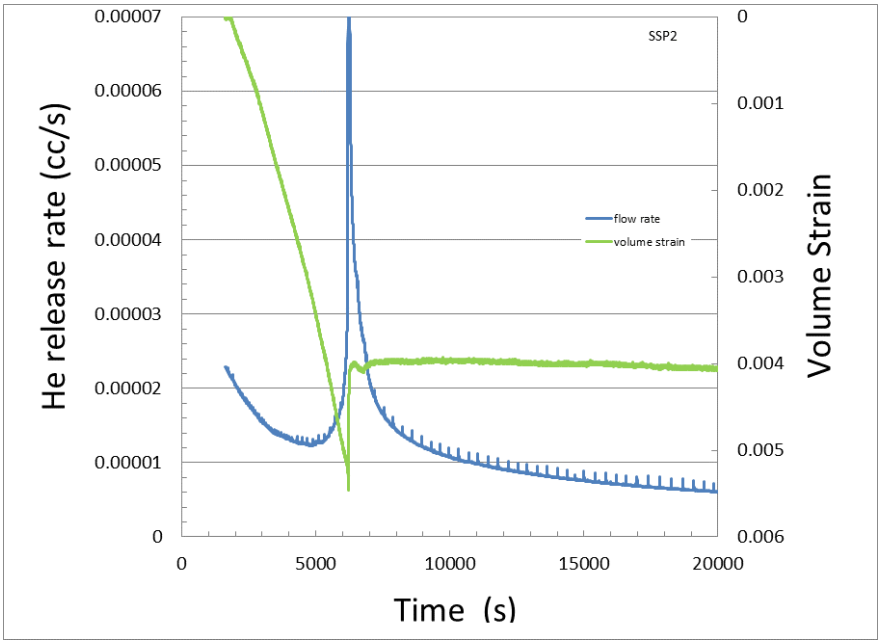

Figure 20. Helium release rate and volume strain versus time (SSP2).

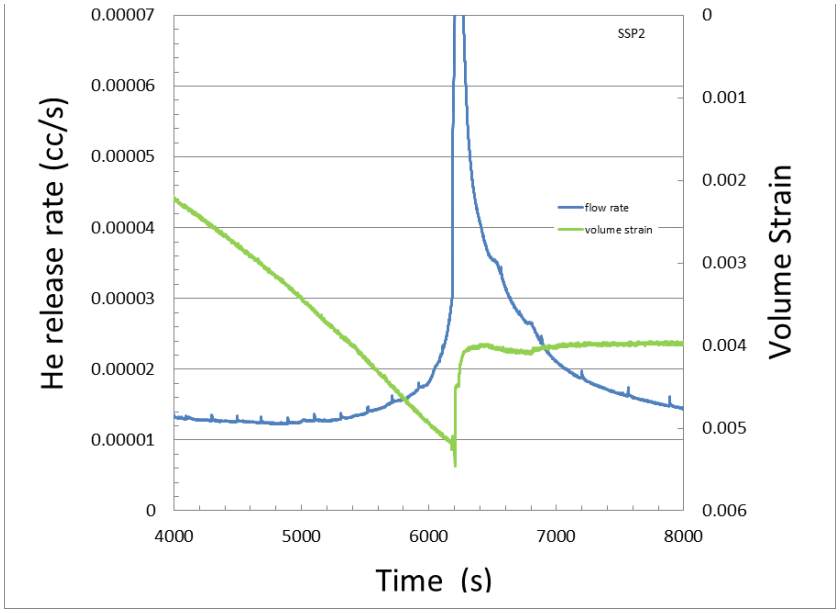

Figure 21. Helium release rate and volume strain versus time, close up time interval (SSP2).

SSP3 has some of the same general characteristics as SSP1 and SSP2, but has some unique characteristics (Figure 22 and Figure 23). Flow decreases with time during compression until around 9000s. Between 9000 and 14000 s a flat or slightly increasing flow rate is observed. A sharp increase and peak in flow around 5×10^{-4} cc/s occurs beginning at 16000 s, followed by decreasing flow. At 17000 s a second sharp peak in flow occurs followed by subsequent monotonic decline. Volume strain increases with increasing time as the specimen compacts until 17000 s, and then decreases abruptly to a local minimum, perhaps indicative of a fracture event. The volume strain then increases slightly prior to another decrease which signals a fracture event consistent with specimen failure and gage saturation. Figure 23 shows a 5000 second segment of the experiment around the fracturing events. It is observed that there are two flow rate peaks increases are roughly coincident with volume strain decreases.

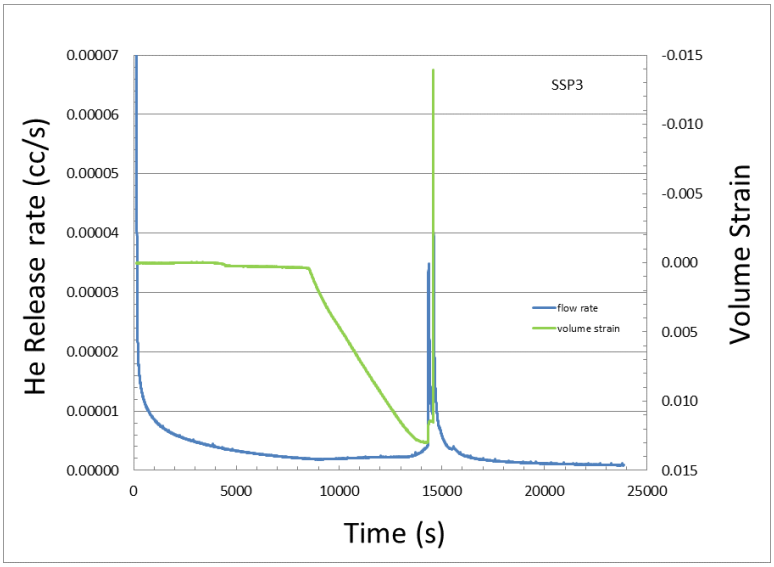

Figure 22. Helium release rate and volume strain versus time (SSP3).

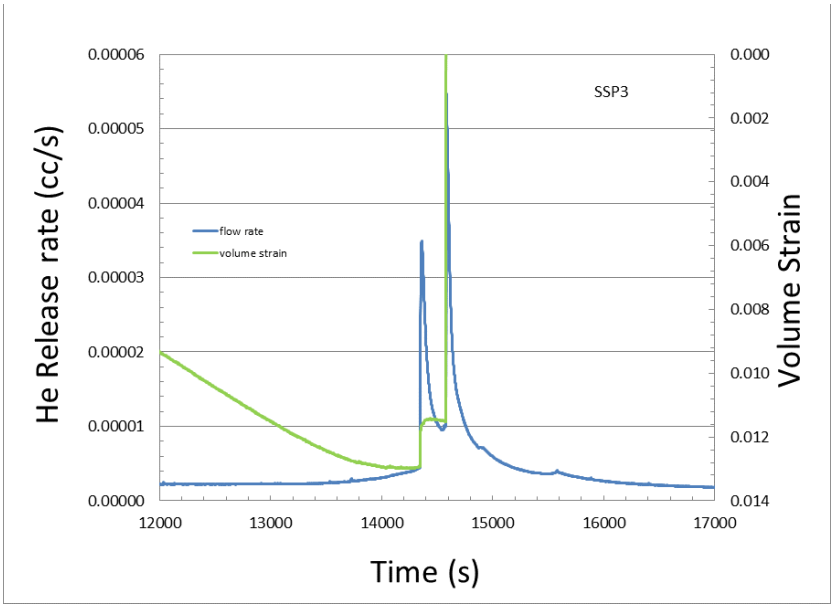

Figure 23. Helium release rate and volume strain versus time, close up time interval (SSP3).

3.3.2 QMS and Flow Test Results

For QMS test 1, the flow rate and confining pressure versus time is plotted in Figure 24. During this portion of the test, the helium leak detector measured gas flow rate; before and after this portion of the test, the QMS was used to measure gas composition release. The sample is generally highly conductive, with permeability estimated at 10^{-6} m^2; this permeability is consistent with that of a shale with a fracture. The flow rate is observed to decrease as pressure is increased from 3.45 MPa to 34.5 MPa prior to sample triaxial deformation (~70,000 s). During deformation, the sample experienced a stress drop, indicative of fracture formation. Post deformation, permeability remains about the same as before deformation.

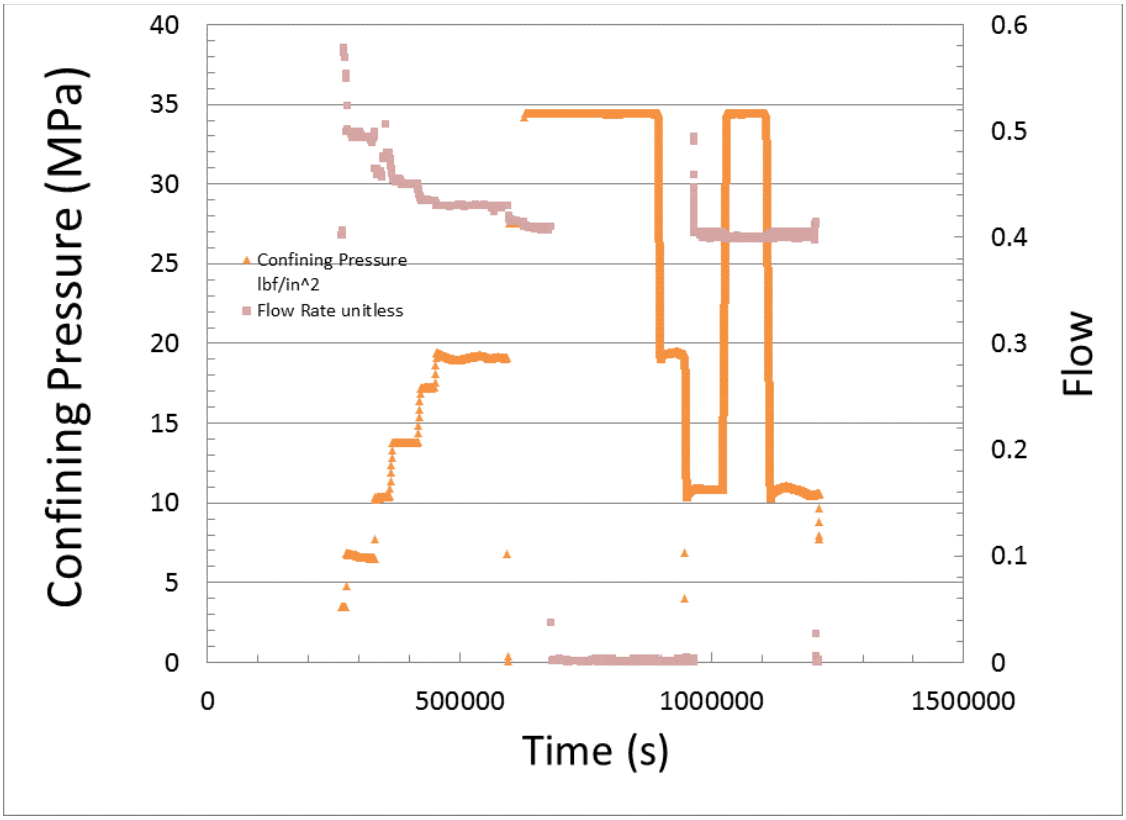

Figure 24. Confining pressure and flow versus time for QMS Test 1.

Figure 25 through Figure 33 plot gas composition release versus time for QMS test 1. Atomic mass 4 is fairly constant prior to deformation, and then decreases post deformation. Atomic mass 16 appears to steadily increase for the test duration. Atomic masses 28, 32, 36, 40 appear to remain constant throughout the test. Atomic mass 44 appears to increase after the deformation event. The N_2/He ratio increases slightly after the deformation and the He/Ar ratio remains about the same during the test.

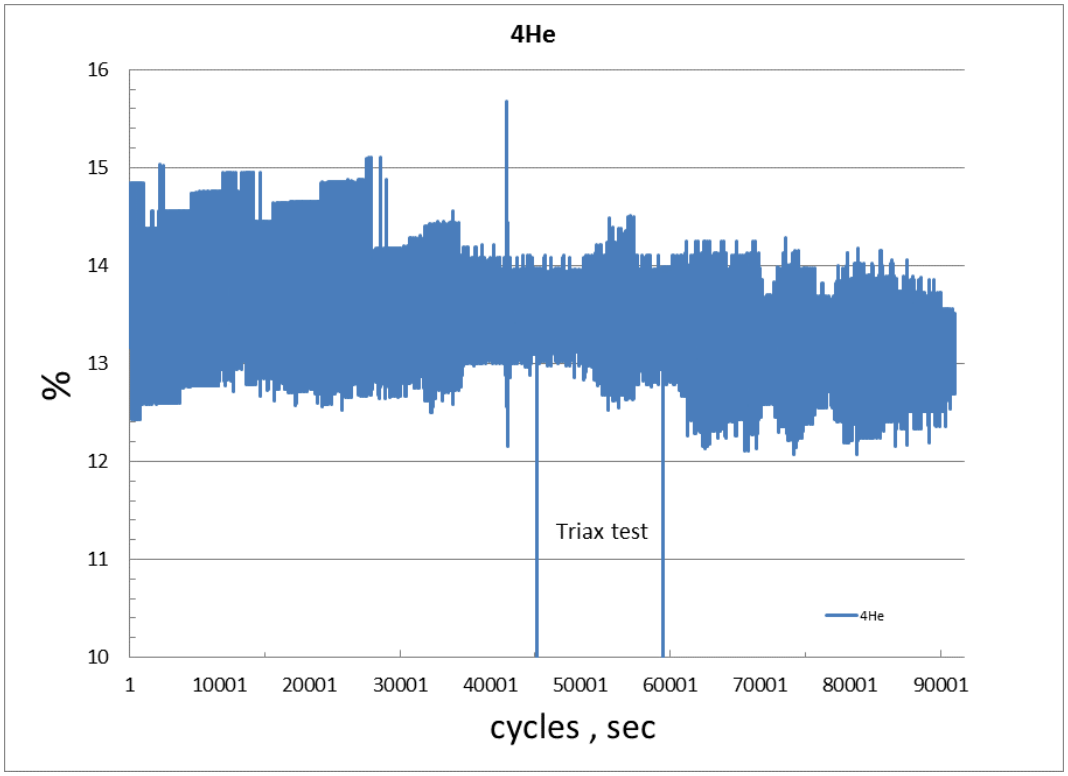

Figure 25. % mass 4 (He) release versus time for QMS Test 1.

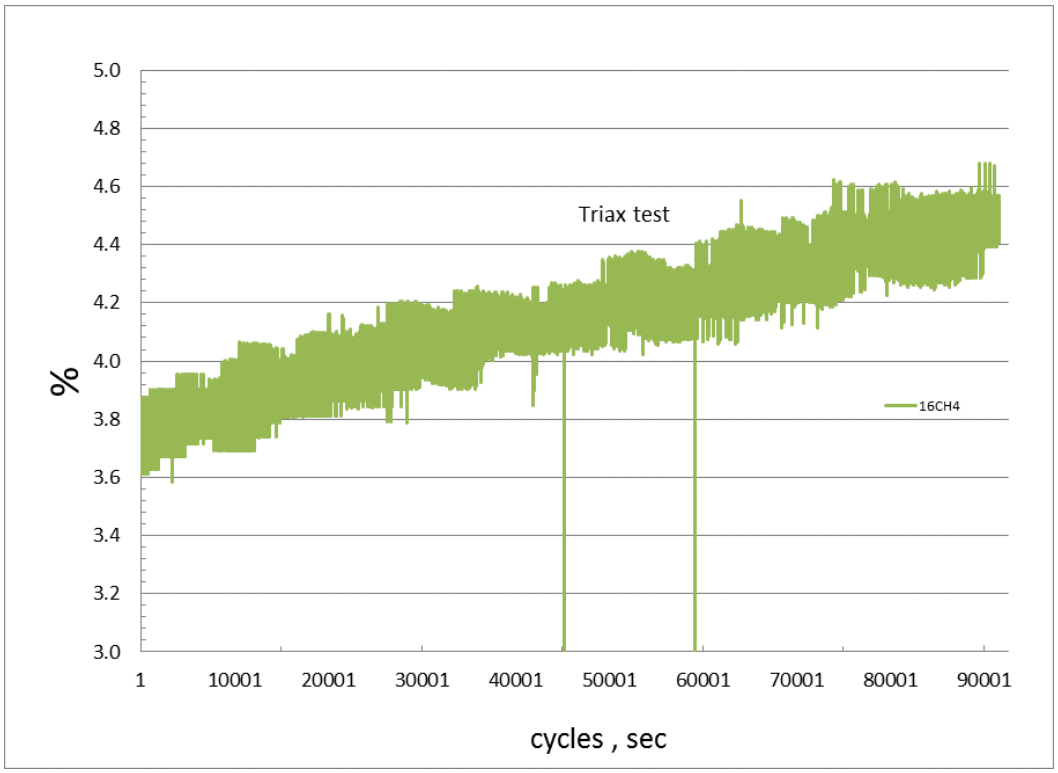

Figure 26. % mass 16 (CH_4) release versus time for QMS Test 1.

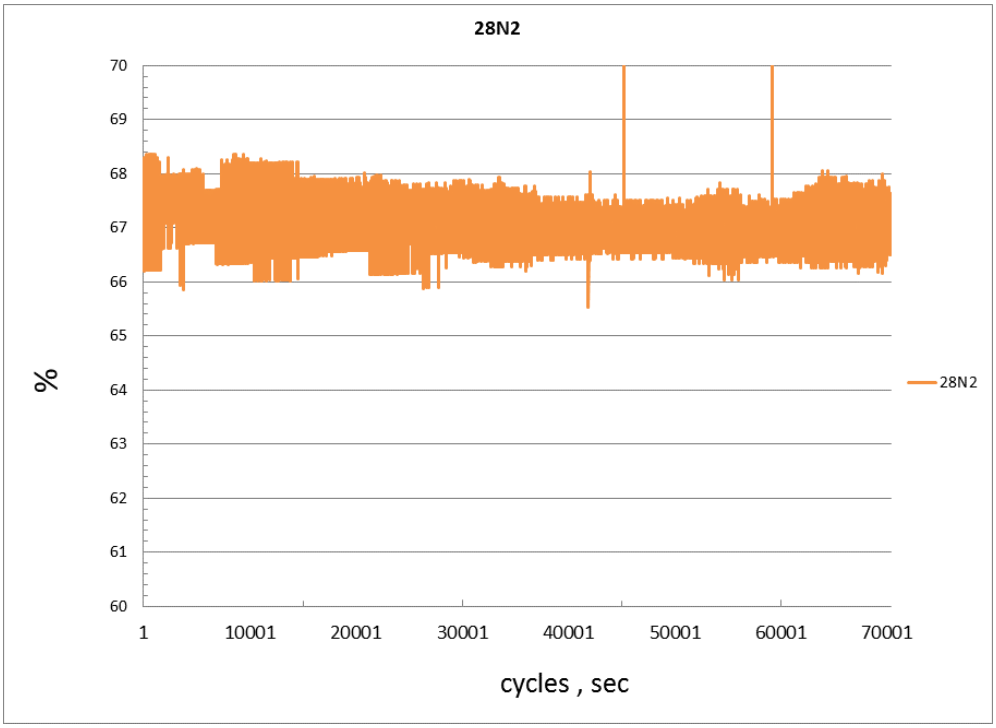

Figure 27. % mass 28 (N_2) release versus time for QMS Test 1.

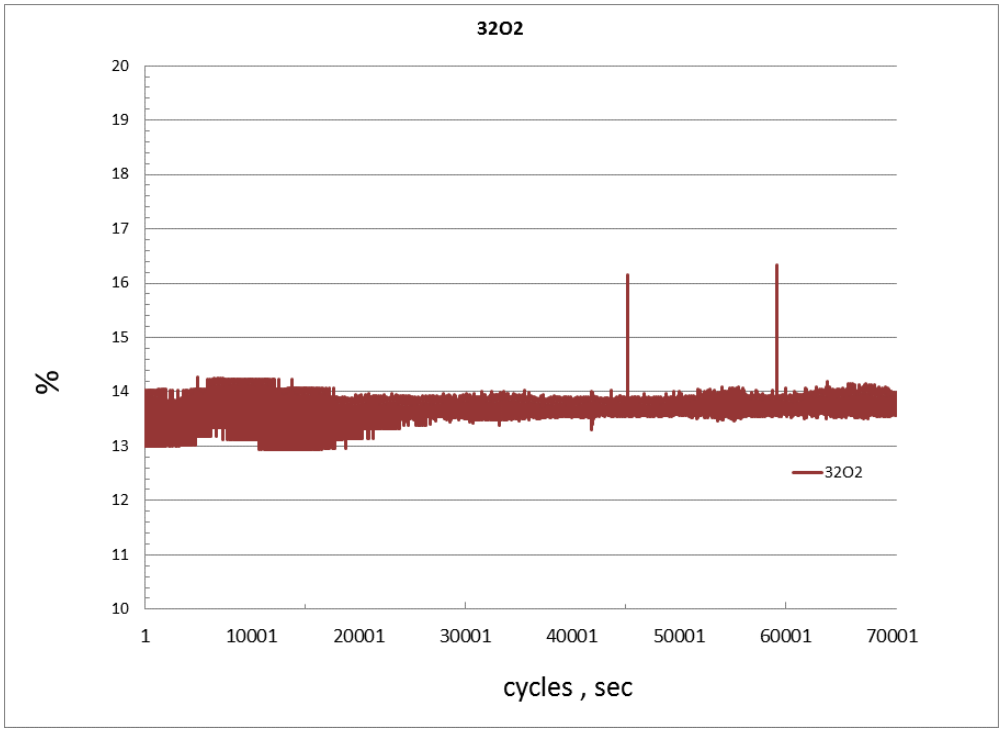

Figure 28. % mass 32 (O_2) release versus time for QMS Test 1.

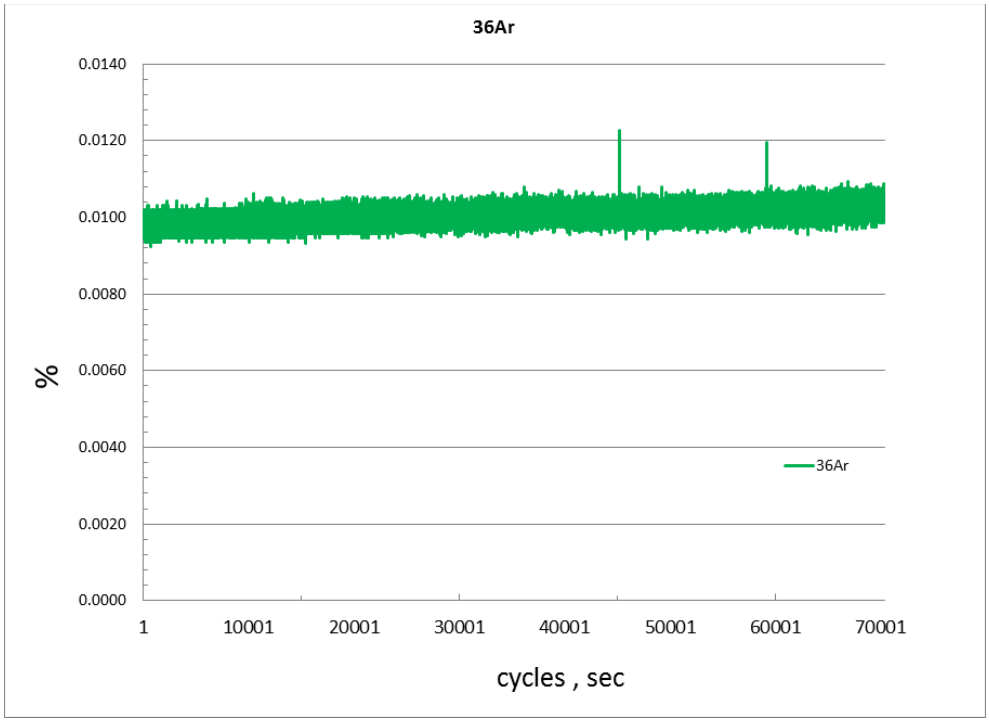

Figure 29. % mass 36 (Ar) release versus time for QMS Test 1.

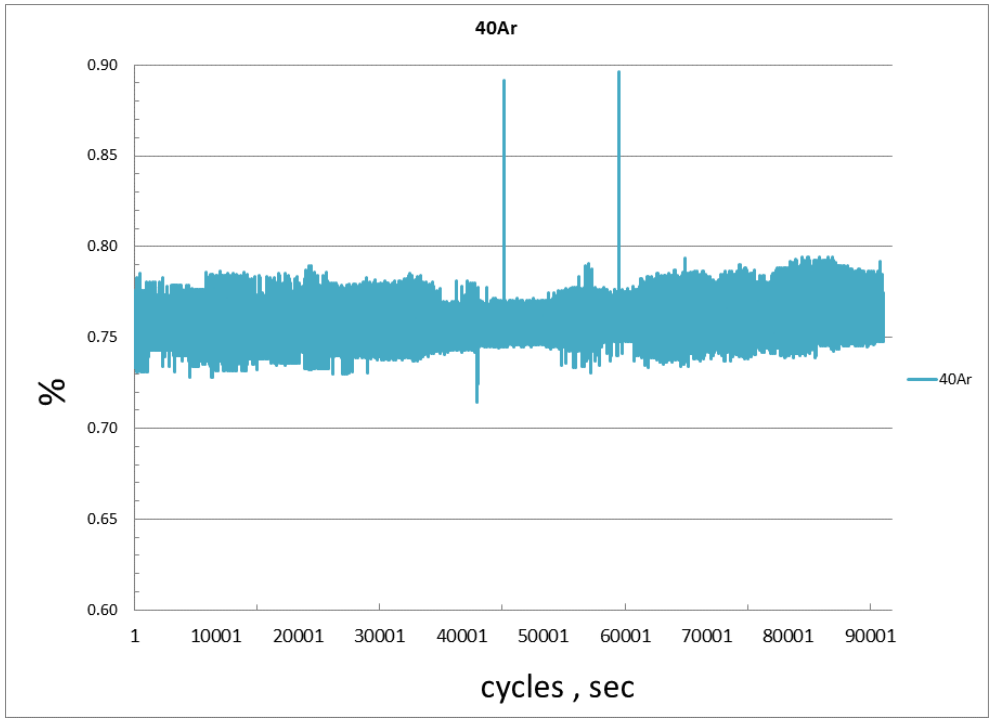

Figure 30. % mass 40 (Ar) release versus time for QMS Test 1.

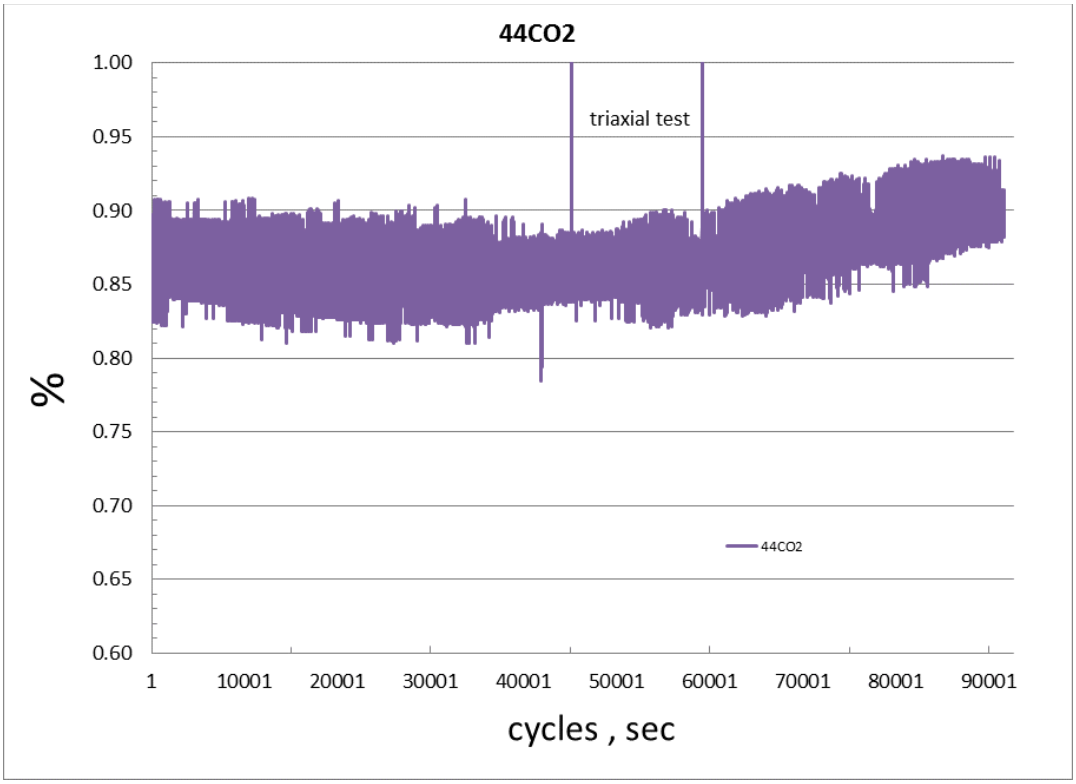

Figure 31. % mass 44 (CO_2) release versus time for QMS Test 1.

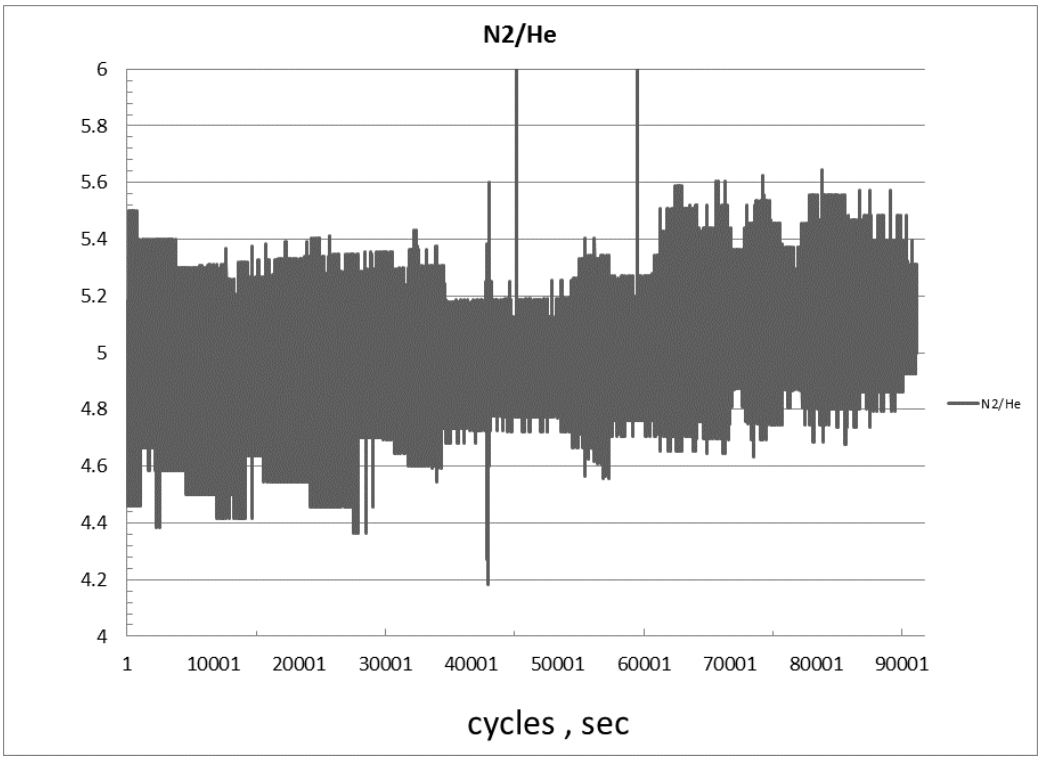

Figure 32. N_2/He ratio versus time for QMS Test 1.

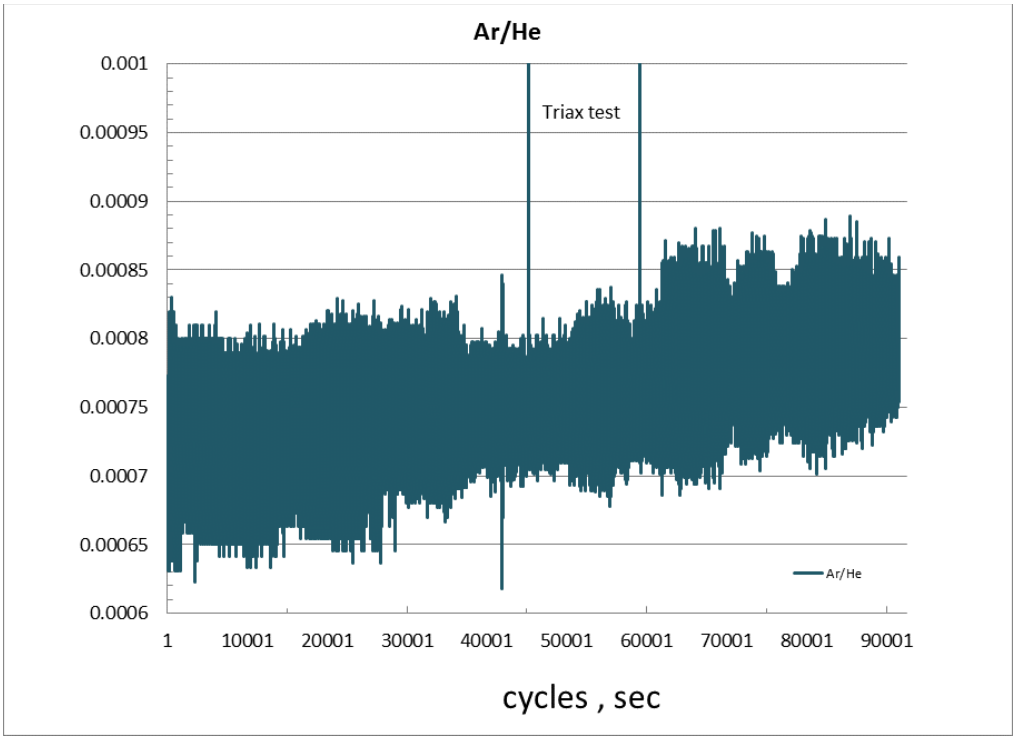

Figure 33. Ar/He ratio versus time for QMS Test 1.

For QMS test 2, gas composition was continuously collected for ~80 hours while the sample was subjected to 3.45 MPa confining pressure. Then confining pressure and differential stress were systematically modified (Figure 34) while the flow rate was measured with the helium leak detector. Generally, when pressure is increased, the flow rate decreases (see early time). During deformation, the flow rate decreases, this is related to sample compaction. At point A the axial deformation was stopped, and the sample held at that displacement, while confining pressure was cycled. The flow rate and axial stress changed in response to the confining pressure cycles, with the flow rate increasing about a factor of 2, and axial stress decreasing by about 1/3.

The plot in Figure 35 represents a closer look at the deformation portion of the test. There is a remarkable relationship between stress change and flow rate.

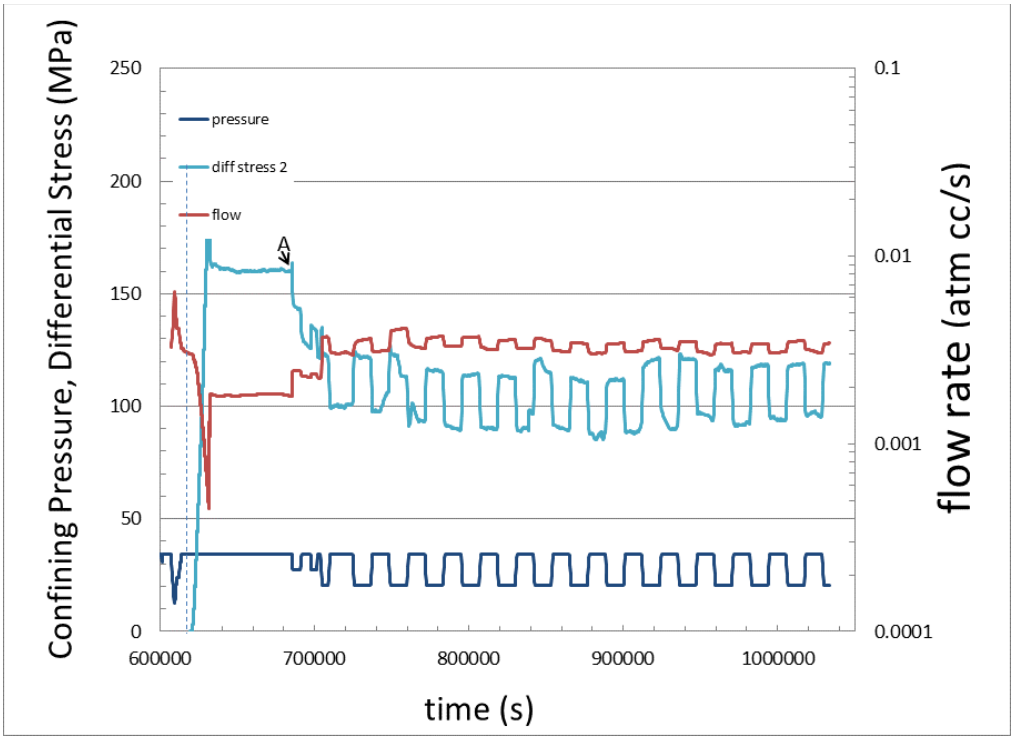

Figure 34. Confining pressure, differential stress and flow versus time for QMS Test 2.

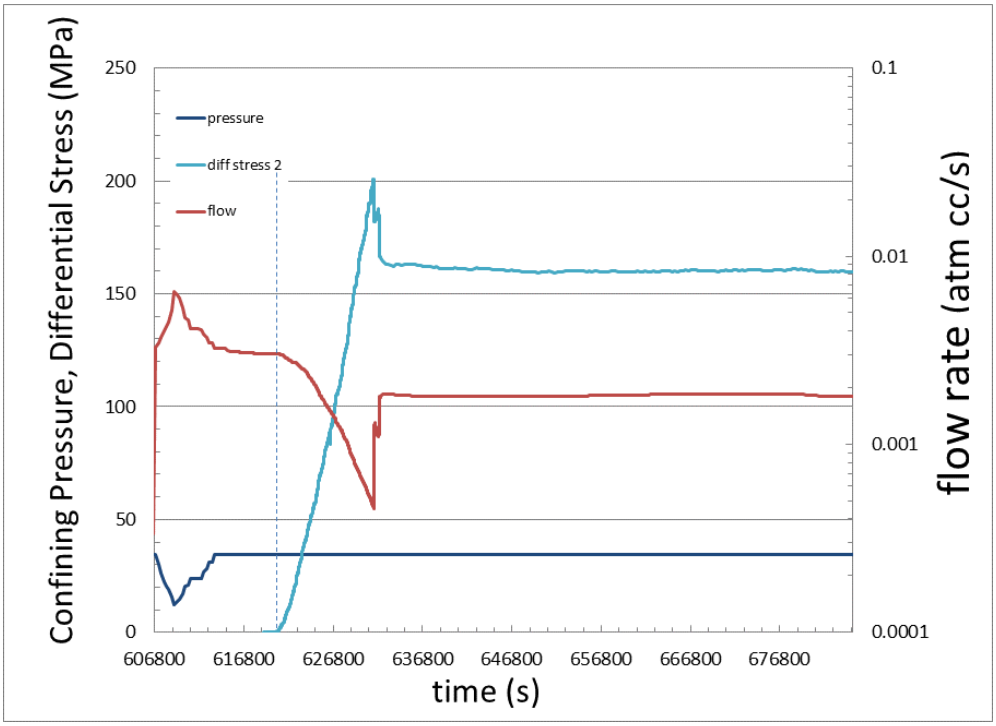

Figure 35. Confining pressure, differential stress and flow versus time for QMS Test 2.

Figure 36 through Figure 44 plot gas composition release versus time for QMS test 2. Early times, the first 30000 cycles are believed to represent a transient pump down of the system and are not discussed. Atomic masses 4, 16 and 44 appear to increase with time; Atomic masses 28 and 30 appear to decrease with time. Atomic masses 36 and 40 appear increase with time at a decreasing rate. The N_2/He ratio decreases slightly and the He/Ar ratio increases then begins to decrease.

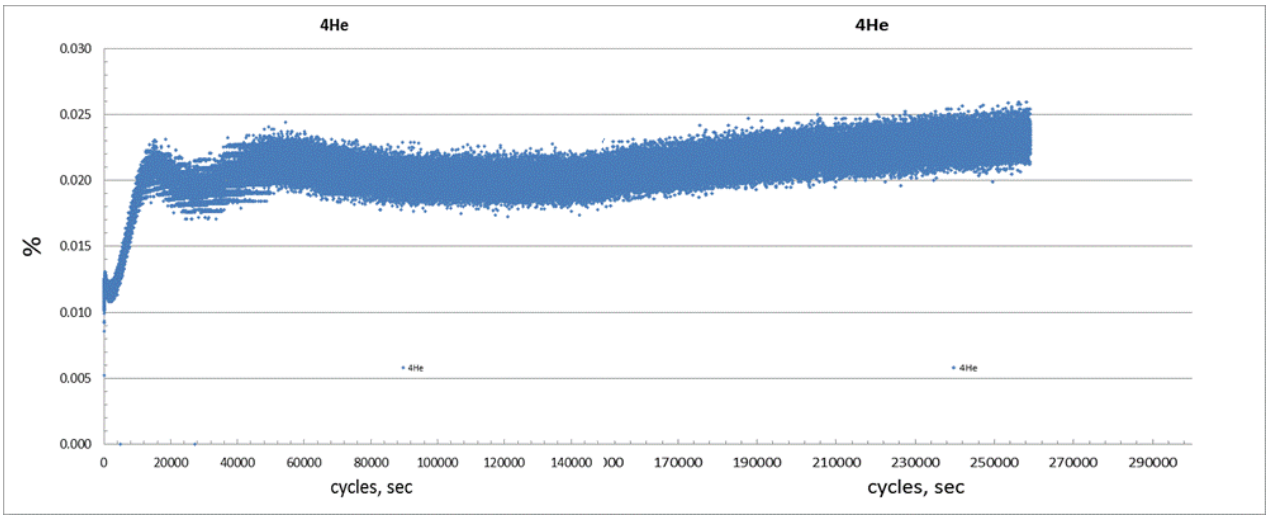

Figure 36. % mass 4 (He) release versus time for QMS Test 2.

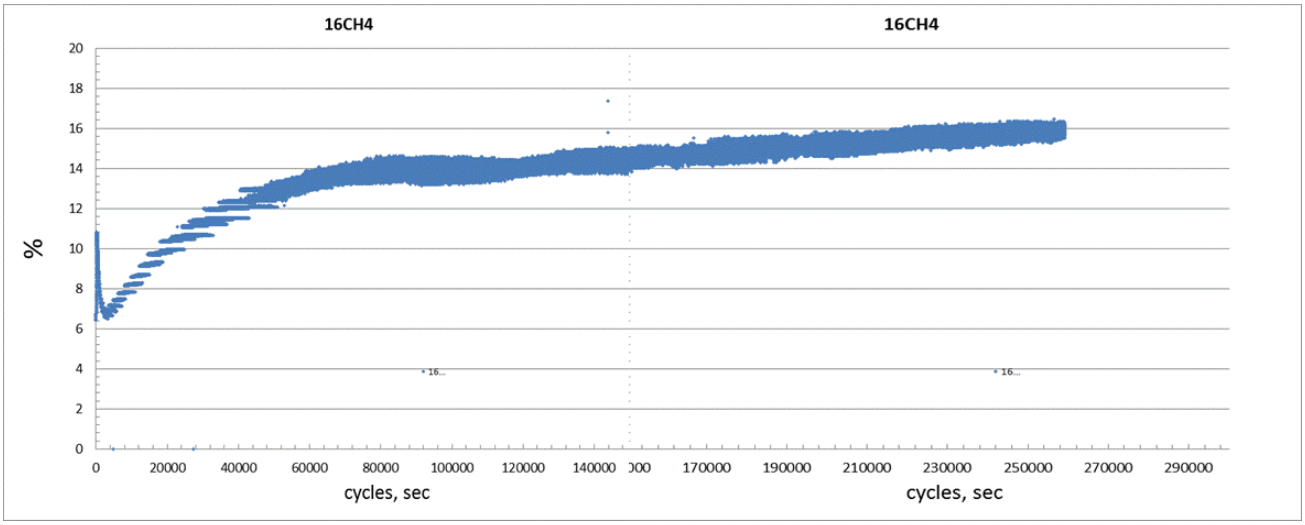

Figure 37. % mass 16 (CH_4) release versus time for QMS Test 2.

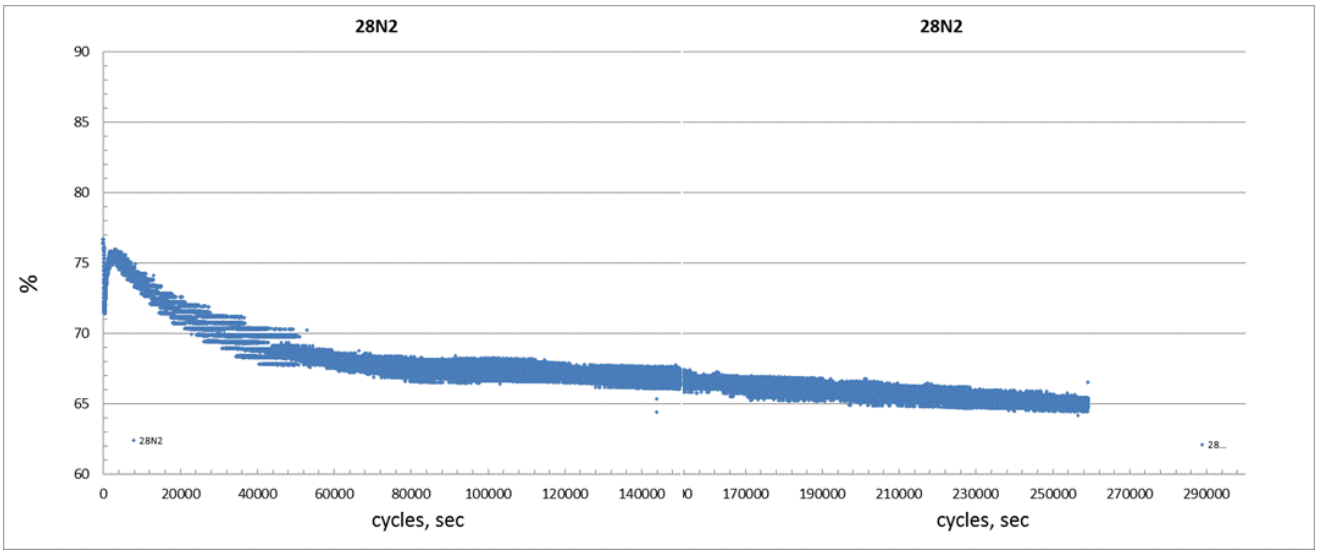

Figure 38. % mass 28 (N_2) release versus time for QMS Test 2.

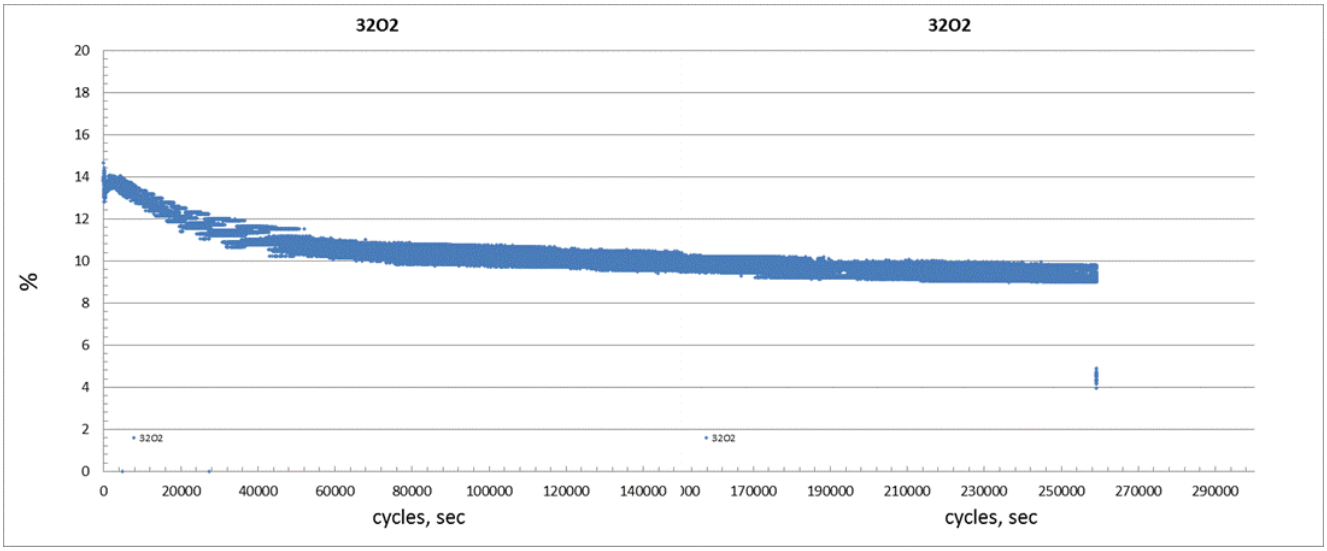

Figure 39. % mass 32 (O_2) release versus time for QMS Test 2.

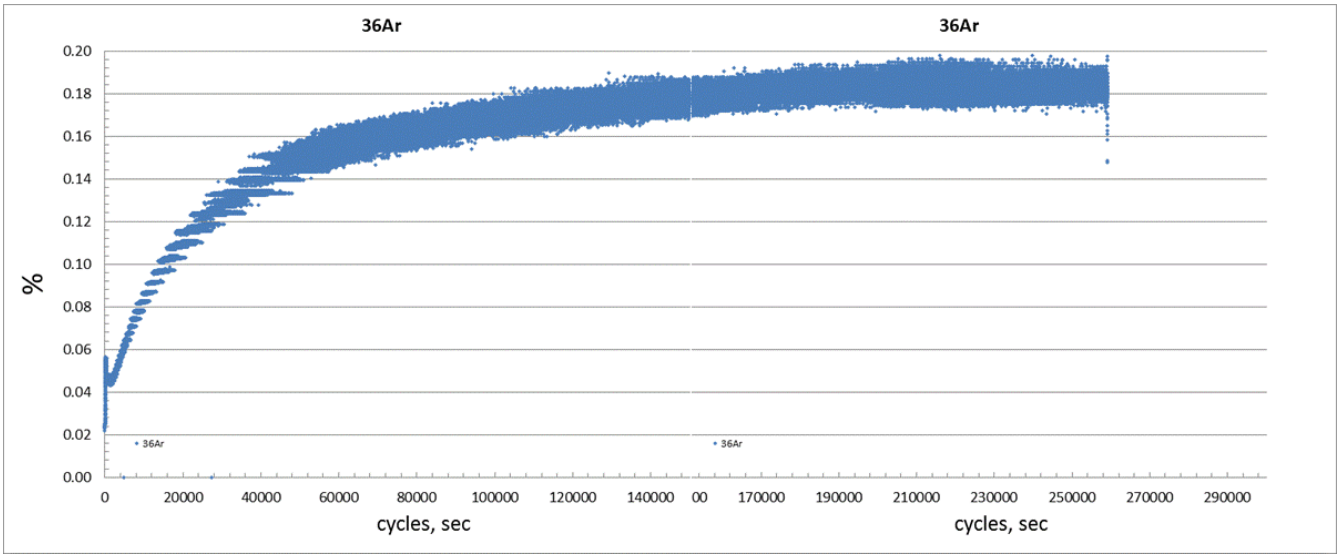

Figure 40. % mass 36 (Ar) release versus time for QMS Test 2.

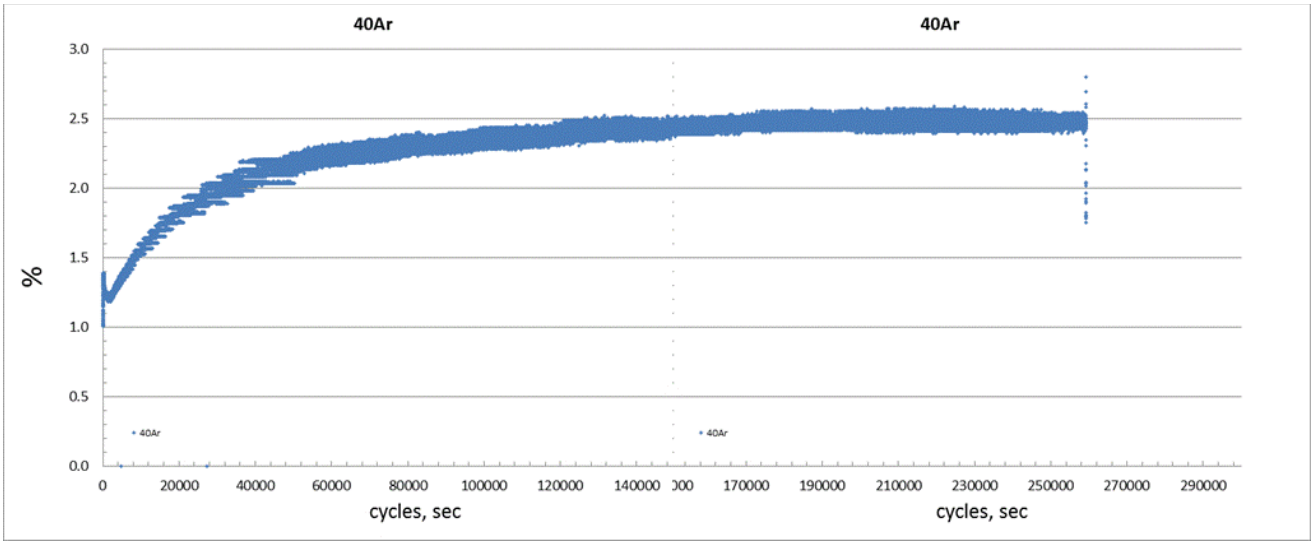

Figure 41. % mass 40 (Ar) release versus time for QMS Test 2.

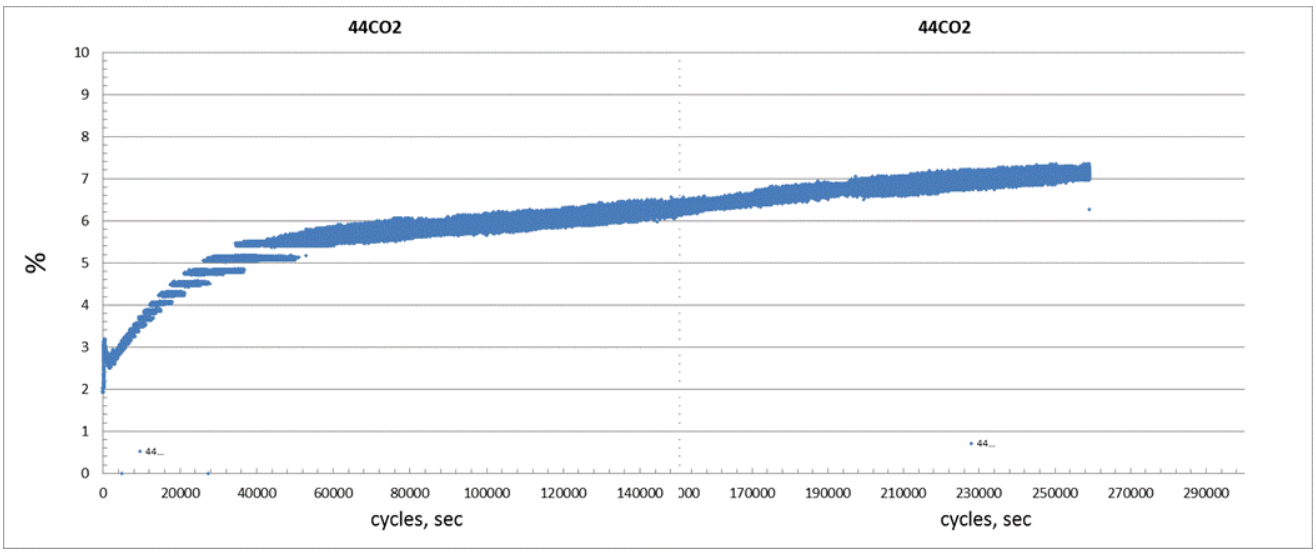

Figure 42. % mass 44 (CO_2) release versus time for QMS Test 2.

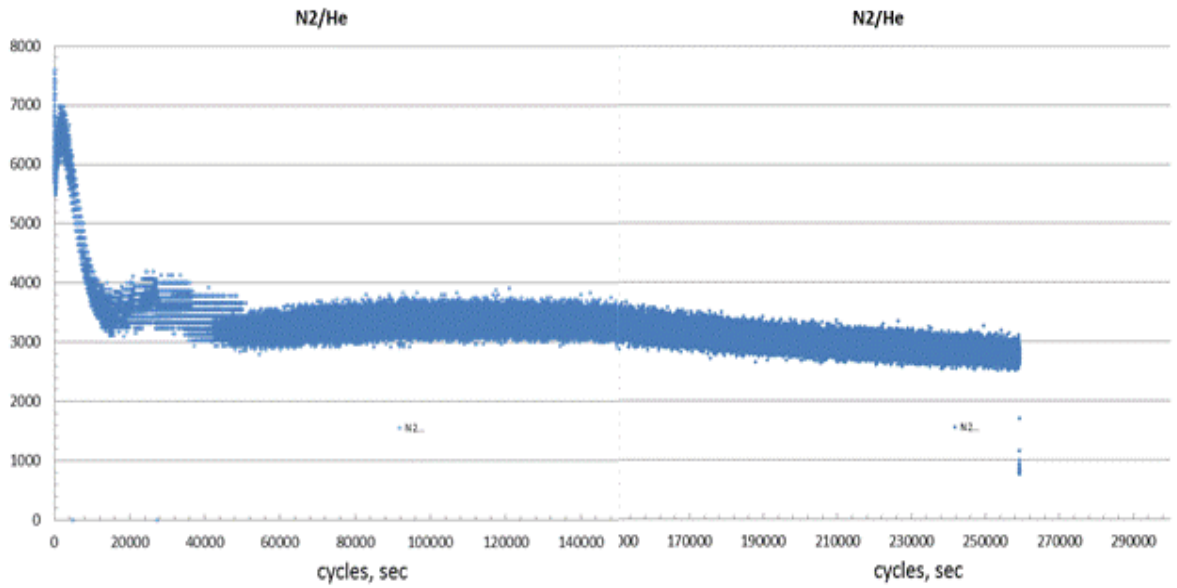

Figure 43. N_2/He ratio versus time for QMS Test 2.

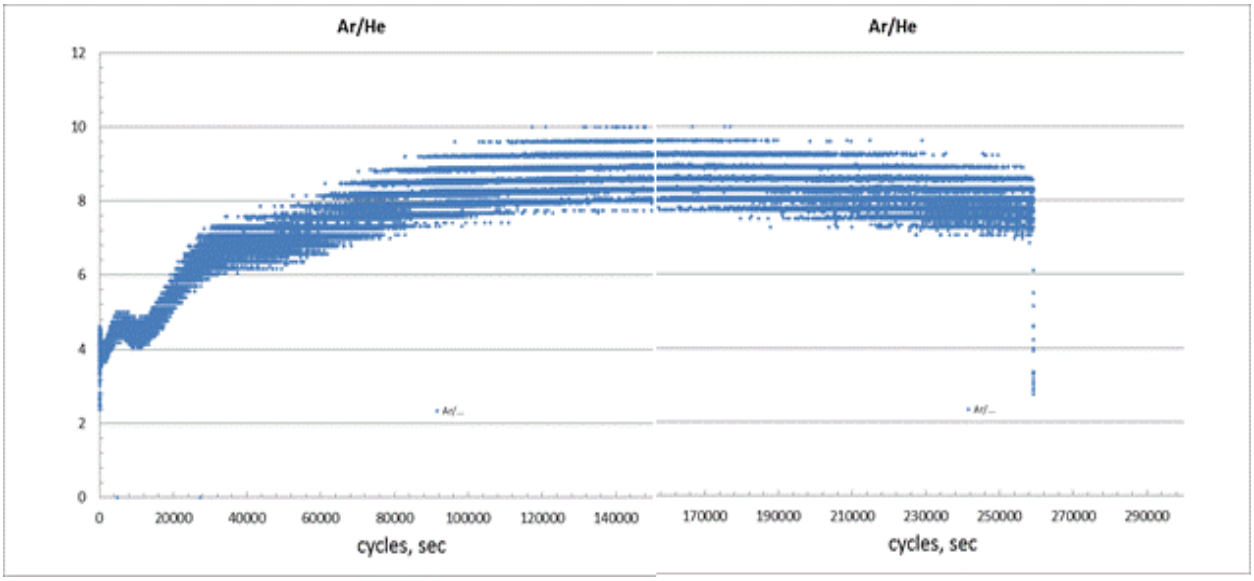

Figure 44. Ar/He ratio versus time for QMS Test 2.

3. 4 Discussion

3.4.1 Helium Release

The experimental approach presented represents a new means to study the complimentary processes of deformation and flow in very low permeability rock. Figure 45, Figure 46, and Figure 47 plot for each test the volume strain versus helium release. Each sample shows a decrease in helium release early, as the sample compacts. In each sample, as deformation proceeds flow rate increases as volume strain continues to decrease. Then, in a different manner for each test the release rate (flow) increases dramatically as volume strain decreases. This is a combination of dilatancy and macrofracture formation.

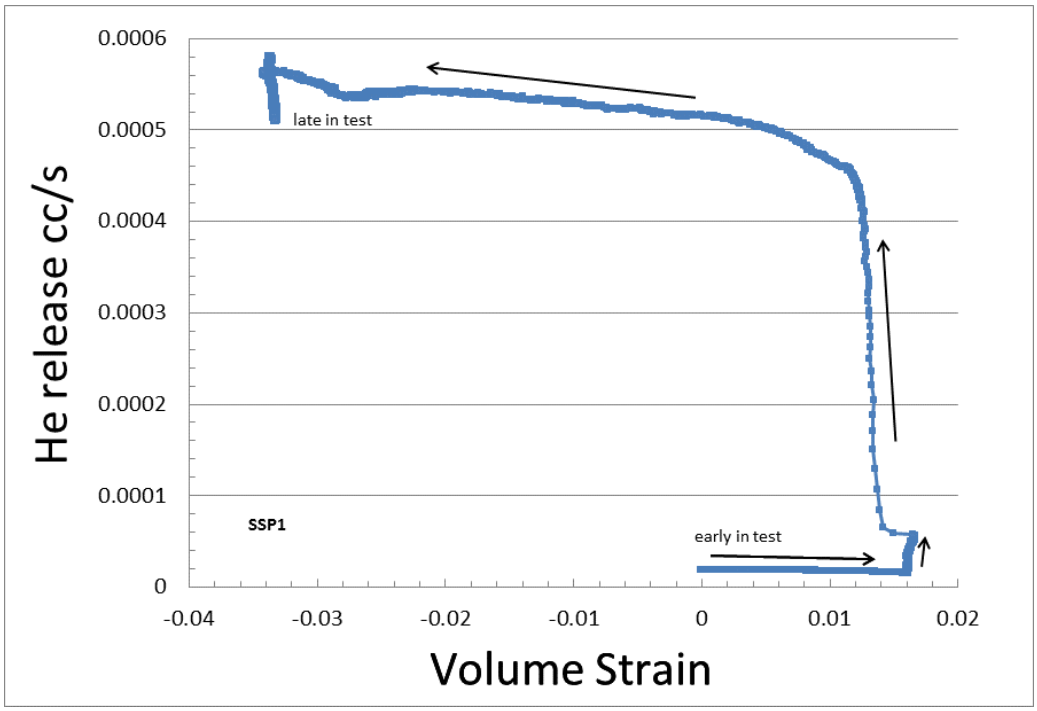

Figure 45. Volume strain versus helium release SSP1.

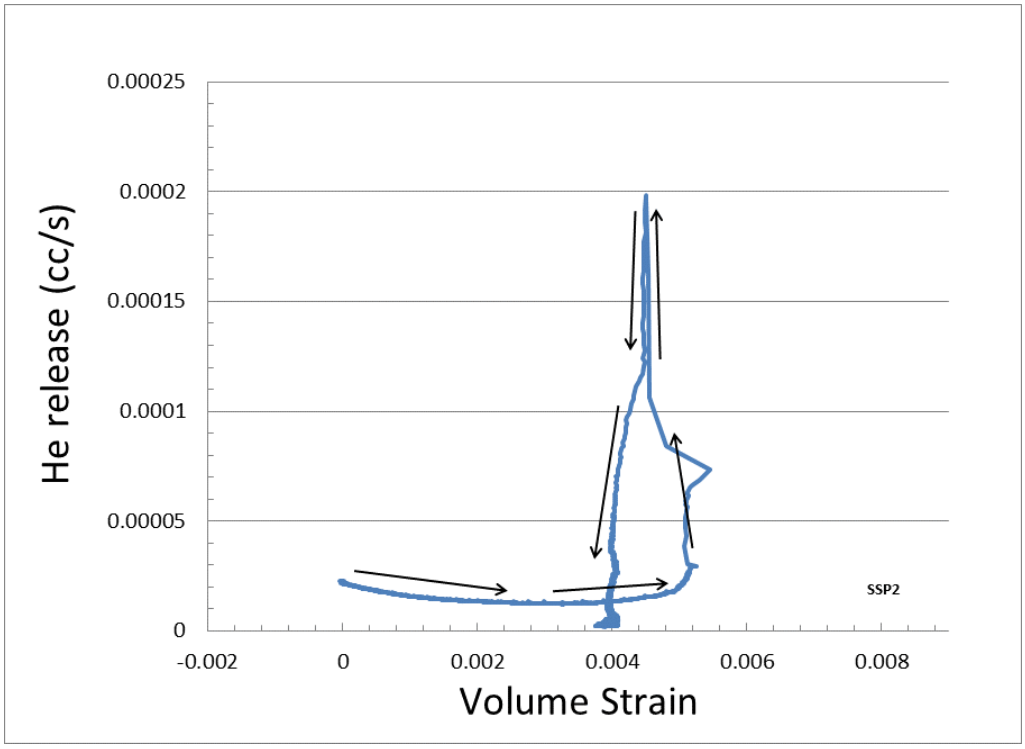

Figure 46. Volume strain versus helium release SSP2.

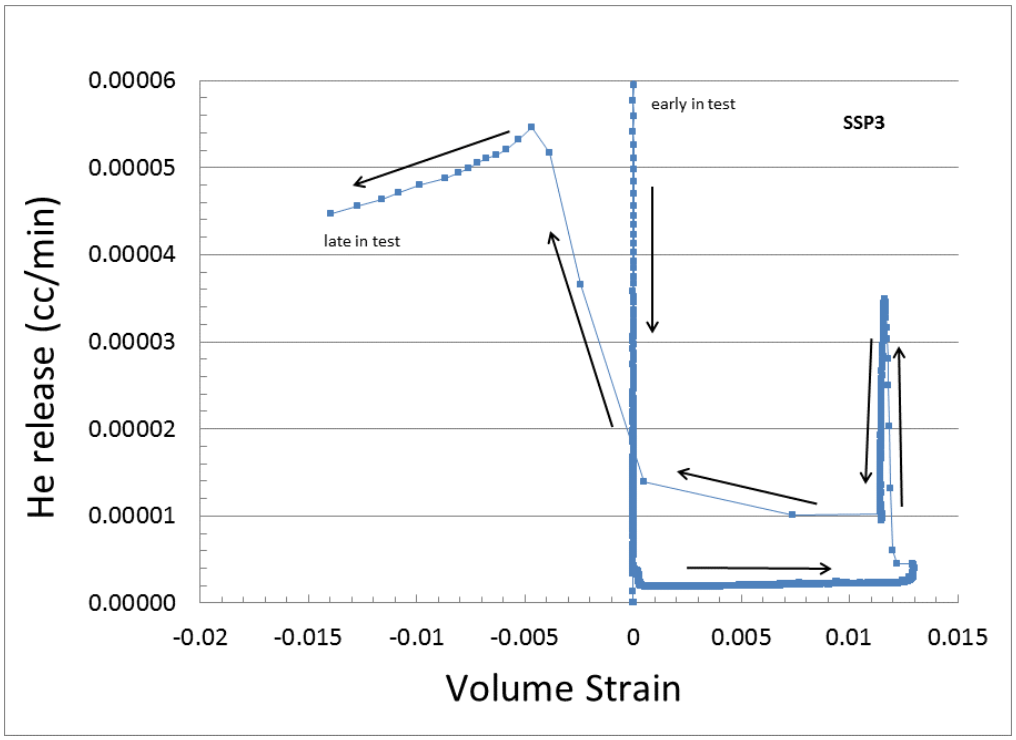

Figure 47. Volume strain versus helium release SSP3.

The compression phase is characterized by a constant or slowly decreasing flow of helium and a constant increase in volume strain. This process shows up as a relatively flat line moving to the right in the He flow vs. strain plots (Figure 45 through Figure 47). As deformation progresses, the increase in flow observed (in advance of specimen expansion) indicates microcracks are forming which connect to pores, facilitating helium release. This process occurs as a short segment moving up and to the right on flow vs. strain plot. The macro fracturing event follows

where flow rapidly increases relative to volume strain and line moves vertically in flow and strain space. In most cases macroscopic dilation follows, where volume strain decreases rapidly compared to flow, showing up as a relatively flat line moving the left in the flow vs. strain diagrams.

For a homogeneous pore network system, undergoing no deformation the helium flow rate should be constantly decreasing as the reservoir depletes. During the compressive phase of deformation, specimens compact, and helium flow rate decreases, in part from compaction and in part from reservoir depletion.

SSP1 and SSP2, are deformed parallel to bedding, and individual small-scale beds are in a constant axial strain state. This concentrates stresses in the stiffer units, perhaps allowing microcracking and pore collapse to initiate/combine at appropriate stress levels to increase flow. This process could explain flow increases in advance of macroscopic volume strain increase. For both SSP1 and SSP2, the flow rate increases dramatically with the presence of a macrofracture. The macrofracture provides an ample conduit(s) that transects bedding and compositional (flow) boundaries, creating a preferential flow path.SSP2 shows a greater flow rate and drains faster (post failure) than SSP1because the SSP2 specimen is connected to the mass spectrometer on both ends and there is not an additional reservoir of helium in the volume of tubing between the sample and the upstream valve. The boundary conditions in SSP1 allow for a better interrogation of the fracture permeability since there is more gas to degas through the fracture, while SSP2 gives more information on the matrix transport from the shale to fracture system since that is the only reservoir of gas after fracturing in that experiment.

SSP3 is deformed perpendicular to bedding, and the individual small-scale beds are in a constant axial stress state. This concentrates strain in the softer units. As deformation progresses, enough modifications of the pore structure take place to facilitate an increase in flow; this is coupled with a draining of the reservoir of gas during the course of the experiment. In SSP3 two fracturing events are observed with smaller strains than in SSP1 and SSP2. In the helium flow signal two smaller flow events are observed.

3.4.2 Results QMS and Helium Flow

The QMS measurements made on these two shale samples show in some cases increasing trends, and some decreasing, and the meaning of the results is thus unclear. The flow measurements are reconcilable in that increasing pressure may be related to decreasing flow, and vice versa. Pressure cycling does not appear to decrease flow rate, once the fractured rock settles in upon itself.

3.5 Conclusions

This scoping study presents experimental results that relate key dependent parameters of flow rate and volume strain in a shale under triaxial deformation. We present the first continuous measurements of gas released from a shale during mechanical deformation. The helium release is sensitive to the structural evolution of the sample during deformation and can be used to infer some of major processes occurring throughout deformation. A common pattern is seen in the responses, which indicate an initial compression phase where axial strain increases and helium release steadily decreases. The compressional phases are followed by a microstructural deformation phase where the permeability of the sample is increased due to increased deformation. During this phase the helium release rate from the core increases even as the

sample continues to show macroscopic volume compression. During fracturing the helium flow rate rapidly peaks, followed by a montonic decrease in helium released from the core. This experiment indicates that the helium release signal is sensitive to the details of the mechanical deformation and provides information on changes in the stress and strain states in shales and other rocks. This work sets the stage for monitoring the release of naturally occurring helium in the subsurface to monitor changes in stress, strain, and permeability in subsurface shale formations. Future work could include a systematic study on a single lithology where in, for example, confining pressure is increased in the test series through the brittle ductile transition. The pressure sensitive deformation could be correlated to the pressure sensitive flow characteristics of the deforming pore structure. The test method developed in the helium release experiments sets the stage for such a test program. These experiments, coupled with detailed observation of operative process each step of the deformation will provide insight into the relationship between flow and deformation of the rock.The flow rate versus pressure data for the fractured shale data demonstrated pressure sensitivity and stress sensitivity. This data should be used to inform modelers of fractured shale behavior.

In terms of the QMS data, the few data collected may represent the first data set of this type. It was not known what was to be expected. The shale samples were from core, but it is unclear how long they sat on a shelf and in what sort of condition. The gas compositions and the release rates collected will hopefully be used to help understand natural processes similar to those being evaluated in other portions of this study. It is unclear from the data set if the imposed deformation affected gas composition release. It appears that the measurements for each test, although lengthy, on the order of days, should have been much longer.

Many of the test types and results presented here may represent the first time tests like this have been performed. The small number of tests is small—the limited results present some intrigue to better understand what these results mean. Perhaps additional data is needed to build a database to develop that understanding.

4. HIERARCHICAL BAYESIAN ANALYSIS OF PRODUCTION DATA FROM UNCONVENTIONAL WELLS

4.1 Introduction

Unconventional gas reservoirs are an increasing source of hydrocarbons in the world. Shale gas is accessible in a fine-grained reservoir in which the gas is stored as both a free gas within the natural matrix and on the surface of the organic fraction as an adsorbed gas. Free gas production is common in shale plays characterized by quartz-rich deposits, while adsorbed gas is more common in organic-rich, clay shales. Tight gas, shale gas, and coalbed methane will be collectively referred to as unconventional gas reservoirs.

Regardless of the matrix structure, these gas reservoirs are characterized by very low permeability. To be economical, extensive hydraulic fracturing is required to assure an economical recovery of gas resources. The nature of hydraulic fracturing results in considerable uncertainty in production forecasts and estimation of reserves. Further contributing to the uncertainty in reserve estimation is that the low permeability of these reservoirs can lead to years of delay before a boundary-dominated flow condition is reached. The ability to forecast shale gas production is further complicated by the inability to correctly account for all of the mechanisms that affect production and the application of predictive analytical tools to unconventional reservoirs continues to evolve.

There has been a recent focus on the application of more formal uncertainty analysis methods for reservoir forecasting. As alternatives to deterministic methods, probabilistic decline curve analysis methods have been proposed to quantify the significant uncertainty in the estimate of reserves in shale gas plays. One of the early investigations by Hefner and Thompson (1996) relied entirely on expert opinion to characterize the uncertainty in the production data for five wells. Since the original graphical methods proposed by Arps (1945), more involved methods for forecasting have been applied and McGlade et al.(2013) provides a broad review of their effectiveness. In addition, formal statistical methods have been explored including bootstrapping non-linear regression techniques (Wang, 2006; Darwis et al., 2009), and time series analysis (Cheng et al., 2010). To overcome the limitations of traditional methods there have been forays into advanced predictive analytics. In particular Gong et al. (2011, 2014) and Gonzales et al. (2012) have focused on Bayesian statistical techniques to enhance forecasting models. However, the benefits and capabilities of these methods were not fully explored.

Traditional uncertainty analysis methods suffer from the need for an extensive observation history. These methods also require substantial assumptions regarding the homogeneity of the forecast uncertainty over time. In the following we will investigate the extension of various deterministic decline curve models to permit consideration of both the uncertainty in the underlying model as an approximation to the complex flow physics as well as uncertainty in the model parameters. We will show how production forecasts for a particular well can borrow information or statistical strength from production data of nearby wells and reduce the uncertainty in the forecasts. This borrowing will result in a reduced uncertainty in forecasts of the reservoir capacity.

4.2 Decline Curve analysis

The focus will be on two of popular decline curve models: Arps and Duong; the latter being more oriented toward hydraulically fractured horizontal wells. Alternatives that remain to be investigated are the stretched exponential and power law models (Valko and Lee, 2013; Ilk et al., 2008).

4.2.1 Arps Model

There are a number of basic, deterministic decline curves commonly employed for reservoir characterization. The first is the fundamental Arps equation (Eqn 1) (Arps, 1945):

Error! (1)

Various Arps models are associated with harmonic decline with b=1, exponential decline, b=0, (Equation 2), and hyperbolic decline, b>0 (Equation 3).

q = **Error!** (2)

q = **Error!** (3)

where b is the hyperbolic exponent, D_i initial decline rate, and q_i initial flow rate, and **Error!**. Fetkovich (1980) demonstrated that the Arps equation assumes boundary dominated flow with a reservoir of slightly compressible fluid, and a constant bottom hole pressure. Since shale gas reservoirs can require years to transition from a transient flow regime to boundary dominated flow, these characteristics present significant challenges to the Arps model. Reservoir forecasting is particularly difficult with only early production data.

4.2.2 Duong Model

As noted by Duong (2011), the previously discussed Arps relationships do not perform well for shale reservoirs where production is dominated by fracture flow and matrix flow is negligible. The point of boundary dominated flow is never reached making permeability and drainage area difficult to estimate. Duong's model is characterized by long term linear flow and is bounded as the production rate approaches zero.

The analysis approach suggested by Duong is accomplished in two steps. First, a log-log plot of Equation 4 is constructed:

Error! (4)

where G_p is the cumulative production and

Error! = **Error!** (5)

G_p = **Error!** (6)

will yield a straight line with a slope of $-m$ and an intercept of a. Once m and a are determined, then Equation 7 is plotted:

Error! (7)

where:

Error!

In the current effort, we will not use two separate steps, but will directly employ a non-linear Bayesian regression of Equation 7 to simultaneously estimate m,a, and q_1. Since we are

concerned primarily with forecasting based on early production information, we will assume that $q_\infty = 0$.

4.3 Analysis

4.3.1 Data

To evaluate the proposed approach, the analysis focused on the same data set used by Gong et al. (2014) and Gonzalez et al. (2012). In particular, 197 horizontally drilled wells where chosen from the Barnett Shale Gas play in Denton, Tarrant, and Wise counties (Figure 48). All data sets are from horizontal wells with either single or multistage hydraulic fractures; an initial production after 1 January 2002 and a production length of at least seven years. For those wells that had been restimulated, only the data associated with the longest period of production was selected. Spurious data were culled.

When applicable, analysis focused on plays from a single company, similar borehole characteristics. Since the actual well locations were unknown, in an attempt to capture similar geology, the subsample of wells was limited to a single county.

Figure 48. Texas Counties of Interest.

4.3.2 Statistical Models

Hyperbolic Decline Model

We will begin with the hyperbolic decline model presented in Equation 3. Since production flow rate cannot be negative, we will assume that q_{ij} is a lognormally distributed random variable, or equivalently, **Error!** is a Gaussian random variable. For consistency, the characteristics of the prior distributions are from Gonzalez et al. (2012).

$$
\begin{aligned}
q_{ij} &= \textbf{Error!} \\
Y_{ij} &\sim \textbf{Error!} \\
\nu_{ij} &= \log\left[q_i\left(1 + b_i Di_i t_{ij}\right)^{-1/b_i}\right]
\end{aligned}
$$

$$
\begin{aligned}
D_{i_i} &\sim \textbf{Error!} \\
q_{i_i} &\sim \textbf{Error!} \\
b_i &= \textbf{Error!} \\
\tau_i &= 1/\sigma^2 \\
\sigma_i &\sim \textbf{Error!}
\end{aligned}
$$

Duong Model

In addition to the hyperbolic model, increasingly popular Duong model was investigated (Equation 4). As with the hyperbolic model, we will assume that monthly production q_{ij} is a lognormally distributed random variable, or equivalently, **Error!** is a Gaussian random variable.

$$
\begin{aligned}
q_{ij} &= \textbf{Error!} \\
Y_{ij} &\sim \textbf{Error!} \\
\nu_{ij} &= \textbf{Error!}
\end{aligned}
$$

$$
\begin{aligned}
a_i &\sim \textbf{Error!} \\
m_i &\sim \textbf{Error!} \\
q_{1_i} &= \textbf{Error!} \\
Lq_{1_i} &\sim \textbf{Error!} \\
\tau_i &= 1/\sigma^2 \\
\sigma_i &\sim \textbf{Error!}
\end{aligned}
$$

where **Error!**, **Error!**, N_f is the number of wells, and N_{s_i} is the number of monthly flow observations samples for well *i*. In this case, we assume that each well is independent of the others and therefore each shale play has a unique triplet **Error!** that much be estimated. In addition, it is assumed that our ability to characterize the production model is different for each well; expressed by allowing the modeling error to vary across wells via **Error!**.

Alternatively, we can assume that wells with similar geology, well depth and well development technology, will be related in a statistical sense. In that case we can assume that **Error!**. This results in the *borrowing of statistical strength* across the production models and reduces the uncertainty in the production forecasts for all similar wells.

All analyses were run using the *R* statistical analysis software coupled with the JAGS (Just Another Gibbs Sampler) Bayesian hierarchical analysis package (Plummer, 2013).

4.4 Production Forecasting

While data from all 197 wells were consistently employed throughout the analyses, the following discussion will focus on a particular group of six wells (Figure 49). The exact location of the wells is not known, but we do know that the wells are located in the same county. It is therefore assumed that the wells have at least roughly similar geology. Further, these horizontal wells are at similar depths and developed by the same company. Finally, we limited all analyses on the first 60 months of production to avoid biasing results due to differences in production time and provide a consistent baseline.

The following discussion will use some or all of these particular wells to highlight the results for various investigations.

4.4.1 Hyperbolic Model Results

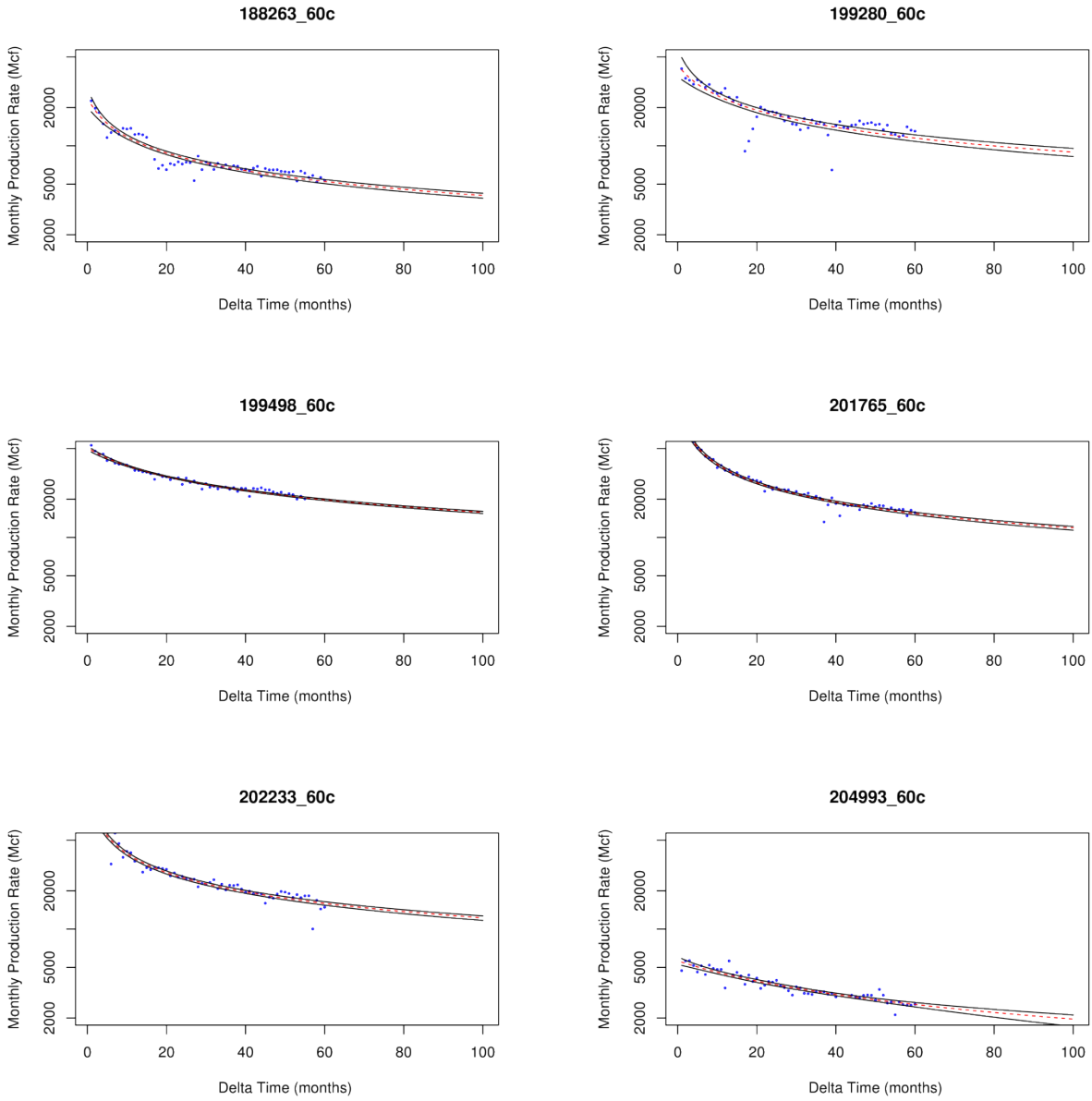

Figure 49. Production Forecasts - Hyperbolic Model.

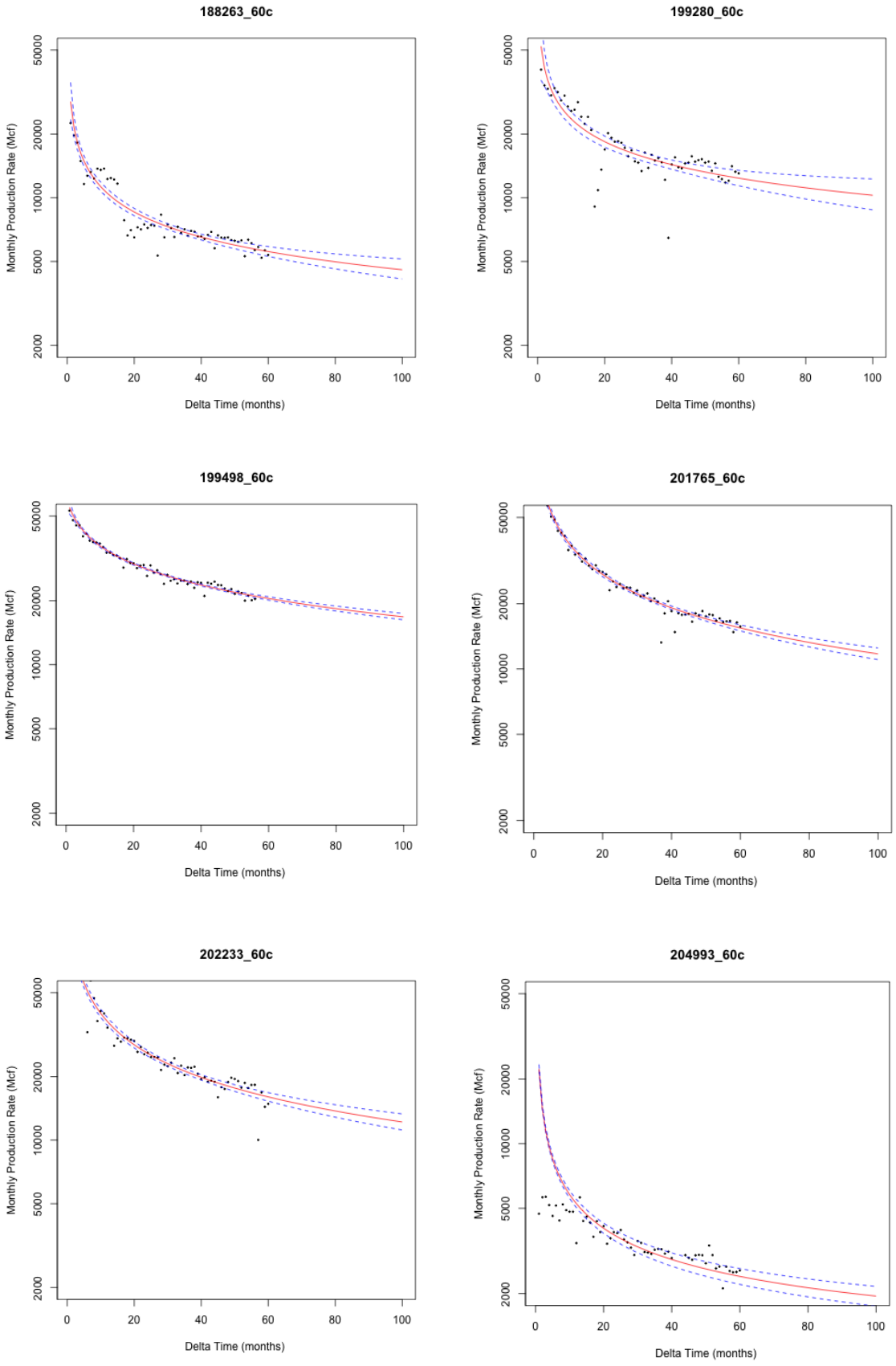

Figure 50. Production Forecasts - Duong Model.

4.4.2 Duong Model Results

Figure 50 summarizes the results from the same six wellbores with the application of the Duong model.

4.4.3 Borrowing Strength

In Figure 51we have again assuming the basic hyperbolic model but have now considered the addition statistical power available by assuming that the modeling error will be the same for the six neighboring wellbores. The borrowing of statistical strength is naturally inherent in hierarchical Bayesian models, but is further amplified by explicitly considering the relationship between the six wells in the production decline analyses.

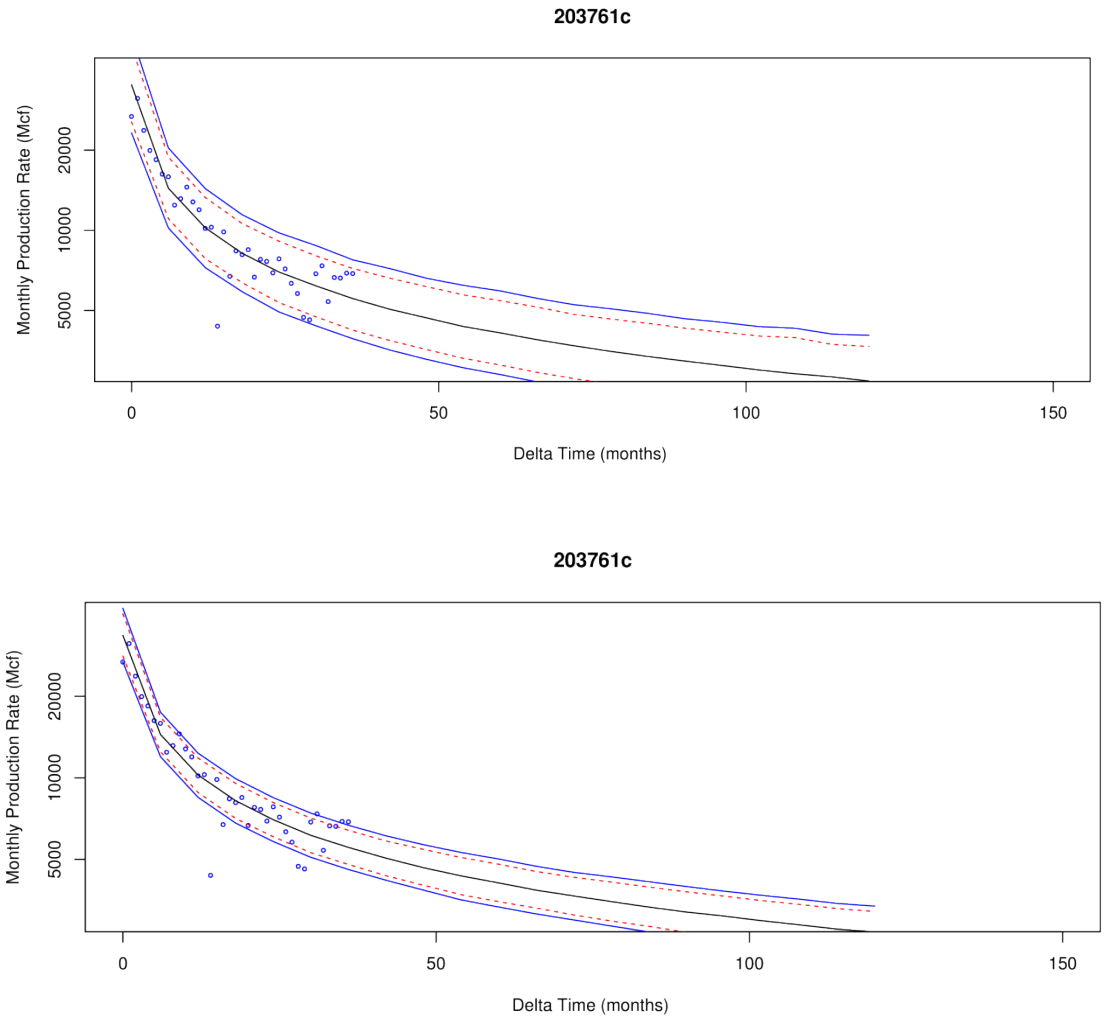

Figure 51. Wellbore 203761 Production using Hyperbolic Model (single and total).

Borrowing statistical strength is important from a number of perspectives. First, it reduces the forecast uncertainty for individual wells. By explicitly accounting for physical similarities in the neighboring wells in the statistical models, we can objectively increase the credibility of production forecasts. This reduction in uncertainty is independent of the assumed underlying

statistical model (e.g. Arps or Duong). Second, by considering the possible relationship between wells, we are able to make more credible long term forecasts earlier in the production process.

Figure 52 begins with the forecast based on the 60 months of production data; the median and 95% credibility limits are depicted. Our goal is to make credible forecasts based on fewer production data points. A "good" forecast will have 95% credibility limits which contain the median for the entire 60 month data. Each subsequent (analysis and) plot (Figure 53) is based on a further reduction in the production data; beginning with 24, 18, 12, and ending with only 6 months.

By considering local well similarities, we are able to forecast the production 60 months in the future with 95% credibility.

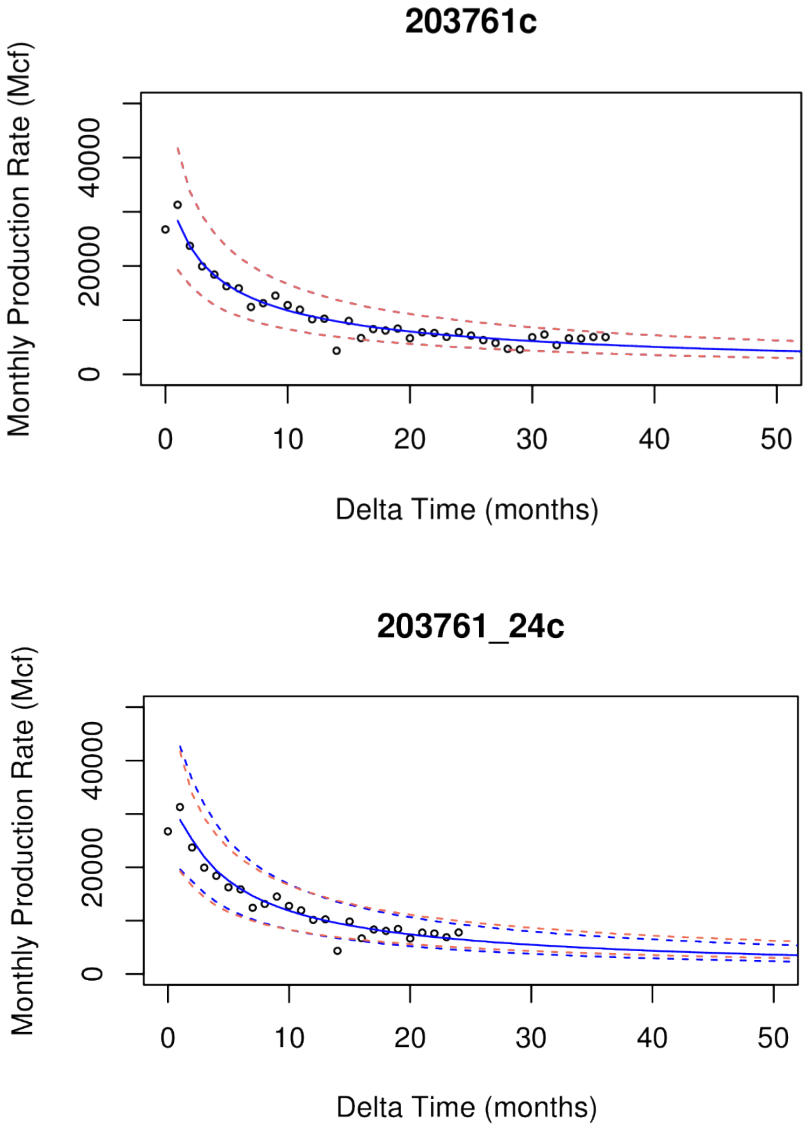

Figure 52. Wellbore 203761 Production Forecast Series.

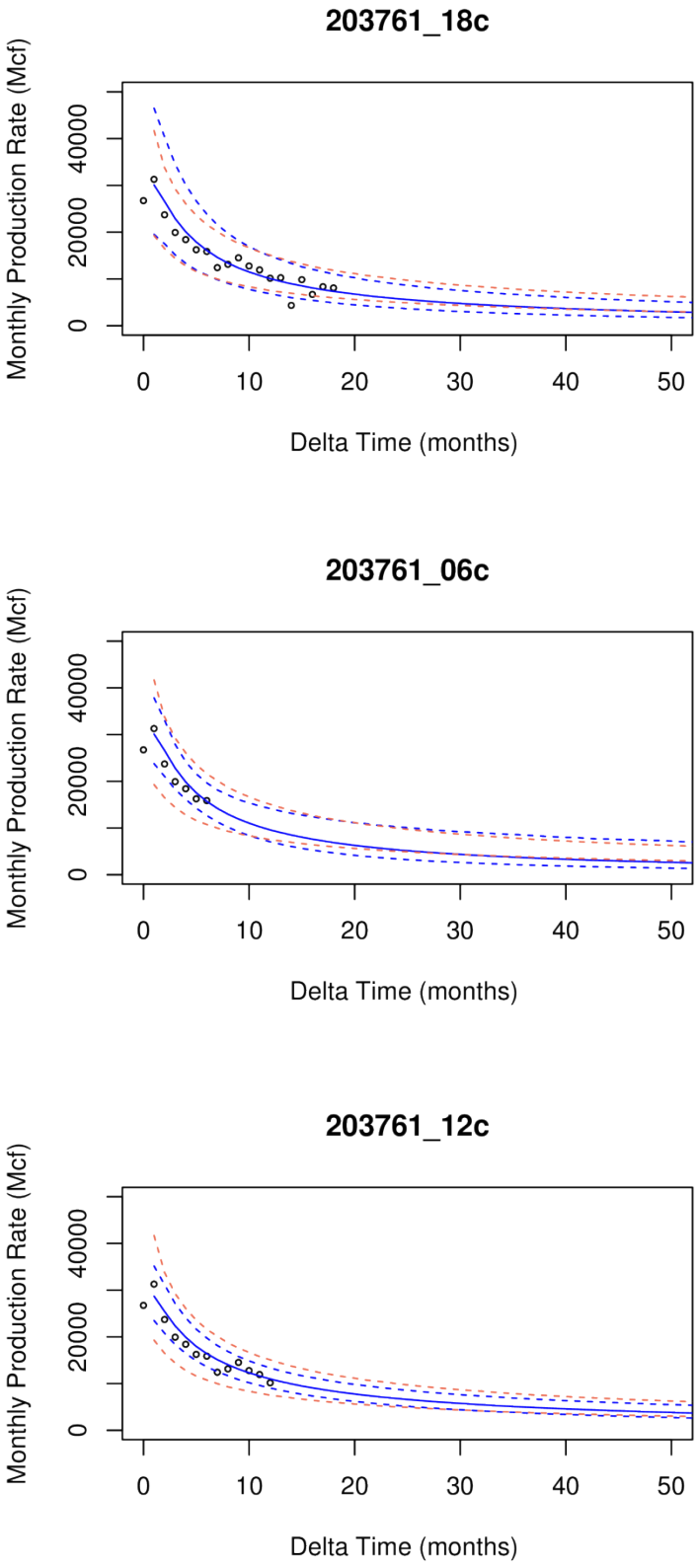

Figure 53. Wellbore 203761 Production Forecast Series.

4.5 Estimated Ultimate Recovery

The expected ultimate recovery from a producing well is provided by the Estimated Ultimate Recovery (EUR). EUR is estimated for a rate of production over a particular well lifetime. Following the work of Duong (2011) and contrary to a traditional approach, we will focus on situations where fracture flow is dominant and matrix contribution is negligible.

Error! (8)

A well nearing the end of its economic life is referred to as a stripper well or marginal well. There is a slight difference between the two: in general, a marginal well becomes unprofitable to operate whenever oil and gas prices drop below its critical profit point. The National Stripper Well Association defines a stripper well as any natural gas well whose maximum daily average gas production does not exceed 90 Mcf per day. The Internal Revenue Service, for tax purposes, uses a threshold of 75,000 cubic feet (2,100 m^3) per day.

For our analyses we will use an approximate value of $q_{eco} = 100$ Mcf per day. In addition, to simply demonstrate the concept we have chosen an arbitrary economic life of $t_{eco} = 30$ years. (More correctly the economic life of each well would be based on the associated q_{eco}.)

Considering that both *a* and *m* are random variables, the estimated ultimate reserve for each well are therefore random variables. Figure 54 depicts the resulting uncertainty distributions for the six wells previously identified. These distributions will provide the basis for risk based decisions regarding the remaining useful production capacity of the wells.

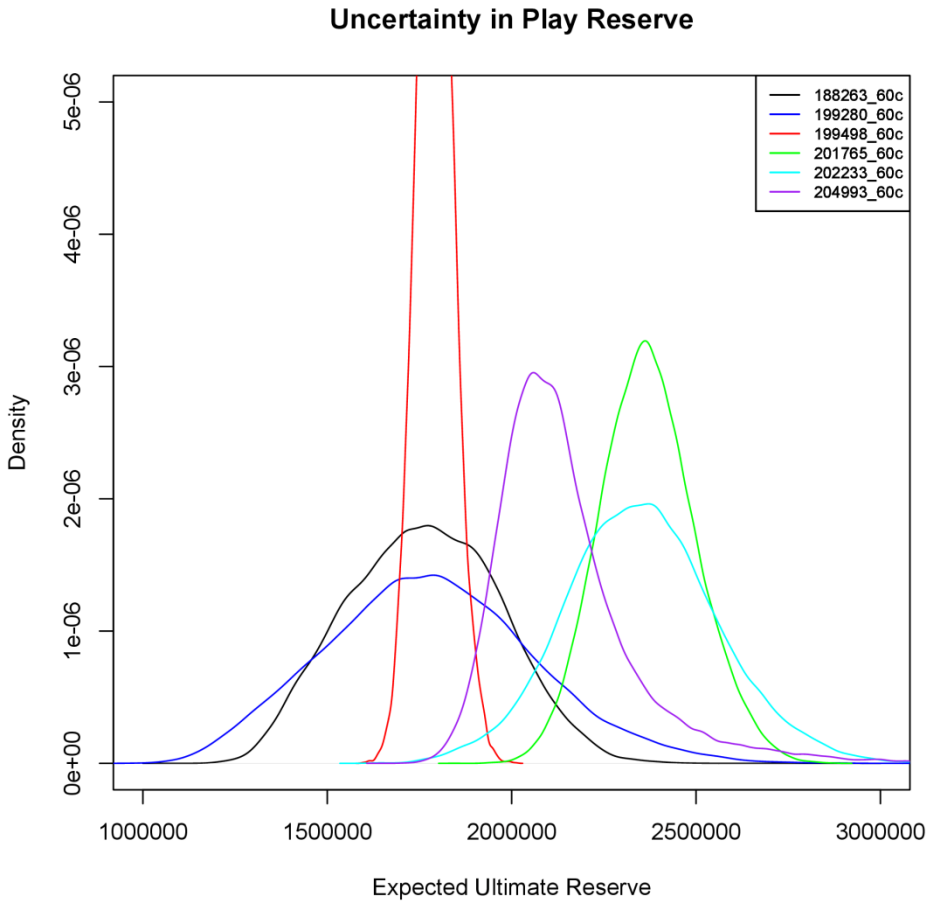

Figure 54. Estimated Ultimate Recovery.

4.6 Conclusions

Differences between this relatively limited investigation are related to a few small but significant analytical areas. First, we assumed production is characterized by lognormally distributed random variable; slightly more realistic assumption than the common assumption of normality used by, for example Gonzalez et al. (2012) and Gong et al. (2014). Second, and most significant, the typical Bayesian analysis models were extended to allow borrowing statistical strength. This results in an increase in the credibility of production forecasts and permits a significant extension of forecast capability.

5. CONCLUSIONS AND RECOMMENDATIONS

The field data collection, laboratory geomechanical testing, and theoretical advances in Bayesian production analysis have exemplified the utility of the noble gases and rigorous statistical approaches to solving shale hydrocarbon challenges. Although the field and laboratory data collected were not conclusive, they hint at their power in future applications.

Recommendations for future field noble gas sampling include:

1. sample from wells with single-phase (i.e., dry gas) production;
2. sample before or better understand separator's influence on noble gas trends; and
3. better understand frac fluid isotopic composition and contribution to system.

Recommendations for laboratory tracer-release testing:

1. perform longer duration tests to observe mass-dependent transport and fractionation of noble gases, and
2. perform tests under a variety of stress regimes to better link tracer flow to specific deformation mechanisms.

Recommendations for Bayesian methods include:

1. performing data fusion with different data types to better quantify and reduce uncertainty,
2. including physics of tracer transport in models that can be included in the Bayesian production analysis framework we have developed in Section 4.

6. REFERENCES

Arps, J.J., (1945), Analysis of decline curves, *Transactions of the American Institute of Mining Engineers*, 160(1): 228-247.

Bauer, S.J., M.Y. Lee, and W.P. Gardner, (2015), Helium-Mass-Spectrometry-Permeameter for the measurement of permeability of low permeability rock with application to triaxial deformation conditions, *ARMA, 49th US Rock Mechanics / Geomechanics Symposium*.

Brace, W.F., (1980), Permeability of crystalline and argillaceous rocks, *International Journal of Rock Mechanics and Mining Sciences & Geomechanics Abstracts*, 17(5): 241–251.

Castro, M.C., M. Stute, and P. Schlosser, (2000), Comparison of He-14 ages and C-14 ages in simple aquifer systems: implications for groundwater flow and chronologies, *Applied Geochemistry*, 15: 1137–1167.

Cheng, Y., Y. Wang, D. McVay, and W. J. Lee., (2010), Practical application of a probabilistic approach to estimate reserves using production decline data, *SPE Economics & Management*, 2(1): 19–31.

Clarkson, C.R., (2013), Production data analysis of unconventional gas wells: review of theory and best practices, *International Journal of Coal Geology*, 109:101-146.

Darrah, T.H.,A. Vengosh, R.B. Jackson, N.R. Warner, and R.J. Poreda, (2014), Noble gases identify the mechanisms of fugitive gas contamination in drinking-water wells overlying the Marcellus and Barnett Shales, *Proceedings of the National Academy of Sciences*, 111(39):14,076-14,081.

Darwis, S., A. Gunawan, M. Ashat, W. S., and N. Sunusi, (2009), Bootstrapping nonlinear regression applied to Arps hyperbolic decline curve, *Journal of Theoretical Statistics*, 27 (2): 219–231.

Dewers, T., Heath, J., Ewy, R., Duranti, L., (2012), Three-dimensional pore networks and transport properties of a shale gas formation determined from focused ion beam serial imaging, *International Journal of Oil, Gas, and Coal Technology,* 5(2/3), 229–248.

Dewhurst, D.N., A.C., Aplin, J. Sarda, Y. Yang, (1998), Compaction-driven evolution of porosity and permeability in natural mudstones: an experimental study, *Journal of Geophysical Research: Solid Earth*, 103(B1), 651–661.

Dewhurst, D.N., Y. Yang, and A.C. Aplin, (1999), Permeability and fluid flow in natural mudstones, *Geological Society of London, Special Publications*, 158(1), 23–43.

Duong, A.N., (2011), Rate-Decline Analysis for Fracture-Dominated Shale Reservoirs, *SPE Reservoir Evaluation & Engineering*, 14 (3): 377–387.

Fetkovich, M.J., (1980), Decline curve analysis using type curves, *Journal of Petroleum Technology*, 32(6): 1065–1077.

Gong, X., R. Gonzalez, D. McVay, and J. Hart, (2011), "Bayesian Probabilistic Decline Curve Analysis Quantifies Shale Gas Reserves Uncertainty", in *Canadian Unconventional Resources Conference*, pages 1–8, Calgary, Alberta, Canada, Nov. 2011.

Gong, X., R. Gonzalez, D. A. McVay, and J. D. Hart, (2014), Bayesian Probabilistic Decline-Curve Analysis Reliably Quantifies Uncertainty in Shale-Well-Production Forecasts, *SPE Journal*, 19(6):1047–1057.

Gonzalez, R., X. Gong, and D. McVay, (2012), "Probabilistic Decline Curve Analysis Reliably Quantifies Uncertainty in Shale Gas Reserves Regardless of Stage of Depletion", in *SPE Eastern Regional Meeting, Lexington, KY*.

Gutierrez, M., Øyno, L. E., and Nygärd, R., (2000), Stress-dependent permeability of a de-mineralized fracture in shale, *Marine and Petroleum Geology*, 17: 895 – 907.

Holland, G., S. Gilfillan, (2013). "Application of noble gases to the viability of CO_2 storage", in P. Burnard [Ed.] *The Noble Gases as Geochemical Tracers*, Springer-Verlag, Heidelberg, p. 177–223.

Hefner, J.M. and R.S. Thompson, (1996), A Comparison of Probabilistic and Deterministic Reserve Estimates: A Case Study. *SPE Reservoir Engineering*, 11(1):1–7.

Hunt, A.G., T.H. Darrah, and R.J. Poreda, (2012), Determining the source and genetic fingerprint of natural gases using noble gas geochemistry: a northern Appalachian Basin case study, *AAPG Bulletin*, 96(10): 1785–1811.

Ikari, M.J., D.M. Saffer, and C. Marone, (2009), Frictional and hydrologic properties of clay-rich fault gouge, *Journal of Geophysical Research-Solid Earth*, 114, B05409.

Ilk, D., J. Rushing, A. Perego, and T. A. Blasingame, (2008), "Exponential vs. Hyperbolic Decline in Tight Gas Sands — Understandingthe Origin and Implications for Reserve Estimates Using Arps' DeclineCurves", in *SPE Annual Technical Conference*, 1–51, Denver, CO.

Katsube, T.J., B.S., Mudford, B.S., and M.E., Best, (1991), Petrophysical characteristics of shales from the Scotian Shelf, *Geophysics*, 56(10), 1681–1689.

King, G.E., (2010), Thirty Years of Gas Shale Fracturing: What Have We Learned? SPE 133456 paper and presentation, SPE Annual Technical Conference and Exhibition, Florence, Italy, 19-22 September 2010.

Kuhlman, K.L., B. Malama and J.E. Heath, (2015), Multiporosity flow in fractured low-permeability rocks, *Water Resources Research*, 51(2):848-860.

Kwon, O., A. K. Kronenberg, A. F. Gangi, B. Johnson, and B. E. Herbert, (2004), Permeability of illite-bearing shale:1. Anisotropy and effects of clay content and loading, *Journal of Geophysical Research*, 109, B10205, doi:10.1029/2004JB003052.

Lee, M. and S.J. Bauer, (submitted 2014), Development of Helium-Mass-Spectrometry-Permeameter for the measurement of permeability of near-impermeable rock.

Loucks, R.G., R.M. Reed, S.C. Ruppel, and D.M. Jarvie, (2009), Morphology, Genesis, and Distribution of Nanometer-Scale Pores in Siliceous Mudstones of the Mississippian Barnett Shale, *Journal of Sedimentary Research*, 79(12):848-861.

Mackintosh, S.J. and C.J. Ballentine, (2012), Using $^{3}He/^{4}He$ isotope ratios to identify the source of deep reservoir contributions to shallow fluids and soil gas, *Chemical Geology*, 304: 142-150.

McGlade, C., J. Speirs, and S. Sorrell, (2013), Methods of estimating shale gas resources-Comparison, evaluation and implications, *Energy*, 59(C):116–125.

Metwally, Y.M. and C.H. Sondergeld, (2011), Measuring low permeabilities of gas-sands and shales using a pressure transmission technique, *International Journal of Rock Mechanics and Mining Sciences*, 48(7), 1135–1144.

Morrow, C.A., L.Q. Shi, and J.D. Byerlee, (1984), Permeability of fault gouge under confining pressure and shear stress, *Journal of Geophysical Research*, 89, 3193–3200.

Nicolas, A.F. Girault, A. Schubnel1, É. Pili, F. Passelègue, J. Fortin, and D. Deldicque, (2014), Radon emanation from brittle fracturing in granites under upper crustal conditions, *Geophysical Research Letters*, 41(15):5436-5443.

M. Plummer, (2013), *JAGS: Just Another Gibbs Sampler - A program for analysis of Bayesian graphical models using Gibbs sampling*, URL:`mcmc-jags.sourceforge.net/`.

Popp, T., and K. Salzer, (2007), Anisotropy of seismic and mechanical properties of Opalinus clay during triaxial deformation in a multi-anvil apparatus, *Physics and Chemistry of the Earth*, 32, 879–888.

Prinzhofer, A., (2013), "Noble Gas in Oil and Gas Accumulations", in P. Burnard [Ed.] *The Noble Gases as Geochemical Tracers*, Springer-Verlag, Heidelberg, p. 225–247.

Slatt, R.M. and Y Abousleiman, (2011), Merging sequence stratigraphy and geomechanics for unconventional gas shales, *The Leading Edge*, 30(3):274-282.

Sone, H., (2012), *Mechanical Properties of Shale Gas Reservoir Rocks and Its Relation to the In Situ Stress Variation Observed in Shale Gas Reservoirs*, PhD Dissertation, Stanford University.

Tuccimei, L S. Mollo, S. Vinciguerra, M. Castelluccio,and M. Soligo, (2010), Radon and thoron emission from lithophysae-rich tuff under increasing deformation: An experimental study, *Geophysical Research Letters*, 37(5).

Valko, P.P. and W. J. Lee, (2013), "A Better Way To Forecast Production From Unconventional Gas Wells", in *SPE Annual Technical Conference and Exhibition*, 1–16.

Wang, Y., (2006), *Determination of Uncertainty in Reserves Estimates from Analysis of Production Decline Data*. PhD thesis, Texas A&M University.

Vermylen, J.P., (2011), *Geomechanical Studies of the Barnett Shale, Texas, USA*, PhD Dissertation, Stanford University.

Yunlai Y. and A.C. Aplin, (2010), A permeability–porosity relationship for mudstones, *Marine and Petroleum Geology*, 27:1692–1697.

Zhang, C., and T. Rothfuchs, (2008), Damage and sealing of clay rocks detected by measurements of gas permeability. Physics and Chemistry of the Earth, 33, S363–S373.

Zhou, Z., C.J. Ballentine, R. Kipfer, M. Schoell, S. Thibodeaux, (2005), Noble gas tracing of groundwater/coalbed methane interaction in the San Juan Basin, USA, Geochimica et Cosmochimica Acta, 69: 5413–5428.

APPENDIX A: RAW DATA

Table 1 . Well 1 (W1) Noble Gas Data from University of Utah

Lab ID	Lab Run ID	Date analyzed	Date Sampled	XN_2	XCH_4	XO_2	XCO_2	XHe3	XHe4	R/Ra	XNe20	XNe22	XAr36	XAr40	XKr78	XKr80	XKr82	XKr83	XKr84	XKr86	XXe124	XXe128	XXe129	XXe130	XXe131	XXe132	XXe134	XXe136
W1-02122014 1420 S1	06231403	6/23/14 8:14 AM	2/12/14 2:20 PM	1.37E-02	1.05E-04	2.56E-06	3.63E-04	4.37E-12	4.91E-04	6.43E-03	1.82E-08	nd	1.12E-07	2.03E-05	3.90E-16	6.18E-10	1.47E-09	1.92E-09	6.26E-09	1.83E-09	3.67E-08	2.46E-10	1.32E-09	nd	9.26E-10	1.33E-09	3.86E-10	4.47E-10
W1-02142014 1400 S2	06231407	6/23/14 11:36 PM	2/14/14 2:00 PM	1.32E-02	1.16E-04	3.53E-06	2.70E-04	4.30E-12	4.79E-04	6.48E-03	4.47E-08	nd	3.45E-08	1.79E-05	4.12E-09	3.83E-09	5.82E-09	1.16E-08	1.20E-08	4.04E-09	8.58E-08	3.34E-10	1.66E-09	2.98E-10	9.44E-10	2.06E-09	4.26E-10	5.37E-10
W1-02162014 1420 S3	06231404	6/23/14 2:15 PM	2/16/14 2:20 PM	7.99E-03	5.79E-05	9.88E-07	1.82E-04	4.14E-12	5.02E-04	5.95E-03	3.07E-09	2.12E-09	2.00E-08	1.11E-05	2.56E-08	6.67E-09	3.87E-09	7.52E-09	5.54E-09	1.83E-09	2.08E-08	nd	3.32E-10	2.56E-10	7.01E-10	4.11E-10	1.25E-10	1.12E-11
W1-02182014-1430 S4	02261505	2/26/15 1:24 PM	2/18/14 2:30 PM	9.55E-03	5.88E-05	-3.19E-05	5.83E-04	5.85E-12	8.33E-04	5.08E-03	8.52E-08	2.32E-08	1.60E-07	9.79E-05	5.86E+05	1.45E-08	4.63E-06	1.52E-05	7.20E-05	5.01E-05	3.43E-11	8.80E-10	nd	1.17E-09	1.86E-09	nd	nd	nd
W1-02202014 1414 S5	06241403	6/24/14 10:58 AM	2/20/14 2:14 PM	6.75E-03	3.06E-05	2.13E-06	1.60E-04	2.31E-12	2.55E-04	6.56E-03	5.86E-08	2.96E-09	2.09E-07	3.62E-05	5.14E-06	1.25E-08	1.95E-07	7.97E-07	6.01E-07	2.76E-07	3.84E-10	5.66E-09	1.52E-08	7.76E-09	1.51E-08	1.72E-08	1.27E-08	1.24E-08
W1-02222014 1415 S6	06241402	6/24/14 8:00 AM	2/22/14 2:15 PM	4.29E-03	1.59E-05	1.35E-06	9.01E-05	1.68E-12	1.90E-04	6.37E-03	4.85E-08	2.00E-08	3.32E-08	2.48E-05	1.51E-05	9.24E-09	2.28E-07	9.92E-07	7.80E-07	4.55E-07	7.43E-09	3.28E-09	9.46E-09	4.06E-09	9.35E-09	1.04E-08	8.03E-09	7.88E-09
W1-02242014 1400 S7	06231406	6/23/14 8:29 PM	2/24/14 2:00 PM	3.27E-03	1.12E-05	7.21E-07	7.75E-05	1.49E-12	1.57E-04	6.88E-03	4.30E-08	nd	1.43E-08	1.80E-05	5.62E-06	1.35E-08	1.82E-07	6.55E-07	5.86E-07	3.43E-07	1.87E-09	5.39E-09	1.45E-08	8.30E-09	1.10E-08	1.69E-08	1.17E-08	1.13E-08
W1-02262014 1400 S8	06241404	6/24/14 2:42 PM	2/26/14 2:00 PM	2.40E-03	8.19E-06	3.17E-07	5.23E-05	1.30E-12	1.49E-04	6.31E-03	nd	7.17E-09	8.21E-08	1.28E-05	5.50E-06	9.53E-09	1.96E-07	7.72E-07	6.76E-07	4.69E-07	8.62E-07	2.90E-09	1.26E-08	4.28E-09	1.35E-08	1.69E-08	9.35E-09	8.08E-09
W1-02282014 1400 S9	07021402	7/2/14 7:49 AM	2/28/14 2:00 PM	2.06E-03	7.14E-06	2.74E-07	5.49E-05	1.74E-12	1.87E-04	6.72E-03	2.75E-09	nd	nd	1.21E-05	2.10E-06	1.01E-08	1.75E-07	7.20E-07	6.09E-07	3.55E-07	7.62E-10	4.31E-09	9.81E-09	5.32E-09	9.17E-09	1.05E-08	7.49E-09	7.70E-09
W1-03032014 1400 S10	07021404	7/2/14 1:54 PM	3/3/14 2:00 PM	2.64E-03	9.38E-06	2.91E-07	6.46E-05	1.37E-12	1.43E-04	6.92E-03	1.41E-08	8.70E-09	6.76E-08	1.47E-05	2.49E-06	9.88E-09	2.03E-07	8.37E-07	6.55E-07	4.29E-07	1.91E-08	2.89E-09	9.10E-09	3.90E-09	7.76E-09	9.06E-09	5.63E-09	5.78E-09
W1 03082014 1445 S11	07021407	7/2/14 10:34 PM	3/8/14 2:45 PM	2.76E-03	1.09E-05	5.32E-07	8.33E-05	1.16E-12	1.32E-04	6.35E-03	7.43E-09	nd	5.97E-08	1.48E-05	2.55E-07	8.63E-09	1.47E-07	5.71E-07	4.58E-07	2.57E-07	8.25E-10	4.28E-09	8.04E-09	4.89E-09	7.82E-09	9.91E-09	6.86E-09	7.41E-09
W1-03132014 1300 S12	06251407	6/25/14 8:52 PM	3/13/14 1:00 PM	5.64E-02	2.18E-04	2.22E-04	1.91E-03	1.82E-12	1.32E-04	1.00E-02	6.62E-07	8.73E-08	1.13E-06	3.13E-04	2.56E-06	1.07E-08	2.25E-07	8.78E-07	6.63E-07	3.23E-07	9.76E-10	3.53E-09	8.99E-09	4.64E-09	7.29E-09	8.26E-09	6.21E-09	6.53E-09
W1-03142014 1210 S13	07021406	7/2/14 7:40 PM	3/14/14 12:10 PM	1.48E-02	2.01E-04	1.34E-05	5.65E-04	2.49E-12	3.22E-04	5.57E-03	6.15E-08	1.23E-08	5.44E-08	2.44E-05	1.50E-05	1.80E-08	4.69E-07	1.76E-06	1.04E-06	1.86E-07	3.72E-09	4.64E-09	7.21E-09	3.94E-09	6.80E-09	7.76E-09	5.36E-09	5.87E-09
W1-03312014-0830 S14	07051401	7/5/14 5:48 AM	3/31/14 8:30 AM	8.22E-02	3.06E-04	7.53E-04	2.58E-03	3.08E-12	1.57E-04	1.42E-02	1.45E-06	1.44E-07	1.64E-06	5.02E-04	4.07E-06	1.09E-08	2.21E-07	8.74E-07	6.32E-07	3.06E-07	8.53E-10	3.86E-09	7.21E-09	4.56E-09	5.83E-09	6.71E-09	5.34E-09	6.00E-09
W1 04072014-1250 S15	07051402	7/5/14 8:39 AM	4/7/14 12:50 PM	7.77E-03	3.56E-05	3.26E-06	2.50E-04	1.44E-12	1.38E-04	7.57E-03	9.68E-08	3.10E-08	1.24E-07	4.31E-05	2.47E-06	9.81E-09	1.79E-07	6.76E-07	4.98E-07	2.54E-07	1.27E-09	3.68E-09	6.38E-09	3.62E-09	5.69E-09	6.27E-09	5.14E-09	5.73E-09
W1-04192014-1240 S16	07051404	7/5/14 2:55 PM	4/19/14 12:40 PM	3.66E-03	1.61E-05	8.33E-07	1.06E-04	1.15E-12	1.57E-04	5.31E-03	3.65E-08	2.16E-08	2.17E-08	1.89E-05	1.45E-06	9.64E-09	2.04E-07	7.66E-07	5.86E-07	3.24E-07	7.41E-09	3.06E-09	5.09E-09	2.80E-09	4.99E-09	5.21E-09	4.11E-09	4.57E-09
W1 05052014-0845 S17	07041406	7/4/14 8:50 PM	5/5/14 8:45 AM	4.74E-03	2.28E-05	1.15E-06	1.29E-04	1.61E-12	1.68E-04	6.92E-03	4.42E-08	1.12E-08	7.69E-08	2.41E-05	2.58E-07	7.50E-09	1.22E-07	4.57E-07	4.96E-07	1.95E-07	1.14E-09	3.68E-09	5.80E-09	4.09E-09	6.13E-09	6.96E-09	5.91E-09	5.46E-09
W1 05232014-0830 S18	07041403	7/4/14 11:47 AM	5/23/14 8:30 AM	5.41E-02	2.30E-04	1.48E-04	1.17E-03	2.08E-12	1.54E-04	9.76E-03	7.97E-07	8.81E-08	8.89E-07	2.77E-04	2.22E-07	8.62E-09	1.63E-07	5.90E-07	4.87E-07	2.83E-07	6.13E-09	2.92E-09	6.00E-09	3.60E-09	5.20E-09	6.43E-09	4.69E-09	5.11E-09
W1-06152014-1010 S19	02251502	2/25/15 7:39 AM	6/15/14 10:10 AM	3.54E-02	1.80E-04	-2.29E-04	1.85E-03	3.20E-12	3.32E-04	6.95E-03	3.29E-07	nd	nd	3.01E-04	5.09E+19	6.89E-07	2.24E-06	1.41E-06	2.11E-06	2.73E-06	0.00E+00	1.02E-06	3.55E-06	2.05E-06	3.11E-06	3.51E-06	3.76E-06	4.05E-06
W1-07132014-0800-S20	02251507	2/25/15 9:31 PM	7/13/14 8:00 AM	1.14E-02	5.18E-05	-6.05E-05	5.79E-04	4.62E-12	5.26E-04	6.35E-03	1.09E-07	2.79E-07	4.71E-08	1.12E-04	1.92E+05	1.21E-08	8.26E-07	3.60E-06	2.02E-05	2.28E-05	2.37E-14	1.03E-10	nd	8.03E-10	1.85E-09	2.24E-09	5.52E-10	nd
W1-08162014-1100 S21	02241502	2/24/15 7:45 AM	8/16/14 11:00 AM	1.74E-01	5.12E-04	8.73E-03	4.90E-03	9.14E-12	4.14E-04	1.60E-02	7.57E-06	1.58E-07	2.92E-06	2.28E-03	6.14E+17	1.03E-06	2.65E-06	1.52E-06	2.52E-06	3.17E-06	0.00E+00	1.19E-06	4.21E-06	2.35E-06	3.51E-06	4.03E-06	4.46E-06	4.80E-06
W1-10272014-1500 S22	02261501	2/26/15 12:37 AM	10/27/14 3:00 PM	1.20E-01	6.71E-04	9.49E-04	4.87E-03	3.27E-12	3.16E-04	7.48E-03	2.25E-06	6.62E-08	3.90E-07	7.46E-04	2.48E+04	1.37E-08	9.00E-07	3.57E-06	2.01E-05	2.42E-05	2.87E-08	nd	nd	9.72E-12	5.81E-10	9.66E-10	1.53E-09	1.32E-09
W1-11182014-1220 S23	08121506	8/12/15 5:44 PM	11/18/14 12:20 PM	6.31E-01	-1.54E-07	8.53E-04	2.43E-04	2.12E-12	1.55E-04	9.89E-03	4.18E-07	1.64E-07	nd	1.67E-04	1.23E-08	4.72E-08	2.29E-08	3.28E-08	1.33E-07	6.36E-08	1.46E-08	nd	7.75E-10	6.06E-10	7.59E-10	2.99E-10	4.68E-10	nd
W1-01202015-0950 S24	08121504	8/12/15 11:11 AM	1/20/15 9:50 AM	1.34E+00	1.35E-06	-2.27E-02	5.52E-05	1.19E-11	7.88E-05	1.09E-01	2.33E-05	2.20E-06	4.34E-05	1.23E-02	7.88E-09	4.21E-08	1.54E-07	1.58E-07	7.31E-07	2.32E-07	9.78E-09	2.28E-09	2.99E-08	3.76E-09	2.49E-08	3.18E-08	1.28E-08	8.89E-09
W1-07132015-1038 S25	08121502	8/12/15 3:54 AM	7/13/15 10:38 AM	-4.25E-02	3.30E-06	-9.37E-04	-4.77E-05	4.14E-12	1.31E-04	2.29E-02	3.58E-06	1.94E-07	6.44E-06	1.36E-03	9.02E-09	3.61E-08	3.49E-08	4.19E-08	1.48E-07	8.91E-08	1.02E-08	7.83E-11	2.89E-09	6.19E-10	2.44E-09	3.39E-09	1.93E-09	1.35E-09
W1-08052015-0930	08121501	8/12/15 12:36 AM	8/5/15 9:30 AM	2.63E-03	-1.70E-06	-1.36E-02	4.25E-05	2.68E-12	9.44E-05	2.05E-02	2.65E-06	3.69E-07	5.74E-06	1.21E-03	9.04E-09	3.74E-08	2.76E-08	3.96E-08	1.08E-07	6.49E-08	1.02E-08	5.51E-10	2.13E-09	1.88E-10	1.95E-09	1.73E-09	1.44E-09	2.66E-10

Table 2. Well 2 (W2) Noble Gas Data from University of Utah

Lab ID	Lab Run ID	Date analyzed	Date Sampled	XN_2	XCH_4	XO_2	XCO_2	XHe3	XHe4	R/Ra	XNe20	XNe22	XAr36	XAr40	XKr78	XKr80	XKr82	XKr83	XKr84	XKr86	XXe124	XXe128	XXe129	XXe130	XXe131	XXe132	XXe134	XXe136
W2-03102014-1230 S1	07041405	7/4/14 5:57 PM	3/10/14 12:30 PM	1.04E+00	1.46E-05	1.92E-01	6.44E-04	9.78E-12	6.73E-06	1.05E+00	1.85E-05	1.82E-06	3.29E-05	9.71E-03	9.41E-07	5.93E-08	2.88E-07	3.26E-07	1.34E-06	4.06E-07	1.82E-06	3.50E-09	4.61E-08	7.01E-09	3.66E-08	4.54E-08	1.76E-08	1.49E-08
W2-03122014 1605 S2	06251403	6/25/14 7:23 AM	3/12/14 4:05 PM	3.44E-03	3.01E-05	1.00E-06	1.23E-04	1.93E-12	2.50E-04	5.57E-03	1.37E-08	nd	6.18E-08	1.46E-05	9.08E-06	1.35E-08	3.37E-07	1.38E-06	8.65E-07	3.27E-07	1.61E-09	4.46E-09	9.83E-09	5.81E-09	1.05E-08	1.35E-08	8.20E-09	8.43E-09
W2-03142014 1210 S3	6261401	6/26/14 1:23 AM	3/14/14 12:10 PM	6.20E-01	8.88E-04	3.08E-02	7.94E-03	7.06E-12	5.42E-05	9.41E-02	8.84E-06	9.04E-07	1.52E-05	4.41E-03	1.94E-06	7.83E-09	1.78E-07	7.09E-07	5.38E-07	2.90E-07	7.12E-09	2.94E-09	1.36E-08	3.88E-09	1.08E-08	1.42E-08	6.42E-09	6.89E-09
W2-03162014-1245 S4	07041402	7/4/14 9:05 AM	3/16/14 12:45 PM	1.16E+00	7.87E-06	9.50E-02	9.78E-05	5.59E-12	4.01E-06	1.01E+00	1.71E-05	1.87E-06	3.12E-05	9.01E-03	5.19E-10	2.03E-08	7.01E-08	7.26E-08	3.43E-07	1.08E-07	9.53E-10	5.14E-09	2.32E-08	5.84E-09	1.79E-08	2.23E-08	1.03E-08	1.22E-08
W2 03182014 1030 S5	07031403	7/3/14 9:07 AM	3/18/14 10:30 AM	3.38E-02	2.25E-04	7.39E-05	9.27E-04	1.37E-12	1.59E-04	6.21E-03	4.71E-07	6.49E-08	4.53E-07	1.76E-04	2.10E-06	1.48E-08	2.65E-07	1.01E-06	6.59E-07	2.58E-07	2.80E-10	6.88E-09	1.17E-08	8.15E-09	1.11E-08	1.31E-08	1.08E-08	1.12E-08
W2-03222014 1230 S7	06251405	6/25/14 1:45 PM	3/22/14 12:30 PM	2.49E-02	1.43E-04	4.08E-05	8.99E-04	1.55E-12	1.68E-04	6.66E-03	3.24E-07	5.56E-08	4.80E-07	1.35E-04	5.89E-06	1.56E-08	2.97E-07	1.17E-06	6.79E-07	2.35E-07	2.18E-10	6.43E-09	1.38E-08	8.16E-09	1.39E-08	1.57E-08	1.18E-08	1.24E-08
W2-03242014 0830 S8	06251404	6/25/14 10:21 AM	3/24/14 8:30 AM	2.69E-03	1.39E-05	2.21E-07	7.65E-05	8.26E-13	1.13E-04	5.29E-03	3.90E-08	2.45E-08	6.83E-08	1.36E-05	2.52E-06	1.11E-08	2.14E-07	8.78E-07	5.99E-07	2.74E-07	6.79E-10	4.29E-09	1.05E-08	5.35E-09	1.09E-08	1.17E-08	8.86E-09	7.89E-09
W2-03262014 1520 S9	07021403	7/2/14 10:34 AM	3/26/14 3:20 PM	4.36E-01	4.25E-04	2.40E-02	2.72E-03	7.31E-12	2.27E-05	2.33E-01	1.03E-05	1.06E-06	1.16E-05	3.32E-03	4.19E-06	1.36E-08	1.97E-07	7.45E-07	7.54E-07	4.85E-07	5.13E-08	3.22E-09	1.72E-08	4.14E-09	1.60E-08	1.77E-08	9.22E-09	7.82E-09
W2-03292014 1230 S10	07031402	7/3/14 6:20 AM	3/29/14 12:30 PM	2.43E-03	1.34E-05	4.89E-07	5.58E-05	7.77E-13	1.12E-04	4.99E-03	1.03E-08	3.67E-09	3.81E-08	1.30E-05	1.66E-06	1.41E-08	2.37E-07	9.31E-07	5.95E-07	2.37E-07	2.00E-10	6.66E-09	1.12E-08	8.36E-09	1.08E-08	1.26E-08	1.15E-08	1.12E-08
W2-04032014 1325 S11	07031406	7/3/14 6:16 PM	4/3/14 1:25 PM	4.77E-03	2.83E-05	2.10E-06	1.20E-04	8.88E-13	9.42E-05	6.81E-03	5.30E-08	2.28E-08	6.89E-08	2.29E-05	1.49E-06	1.03E-08	2.16E-07	7.94E-07	6.03E-07	3.20E-07	8.23E-09	3.20E-09	6.13E-09	3.18E-09	4.99E-09	6.05E-09	4.48E-09	4.44E-09
W2-04082014 1250 S12	07031404	7/3/14 12:30 PM	4/8/14 12:50 PM	2.48E-03	1.43E-05	6.92E-07	6.77E-05	7.31E-13	1.05E-04	5.05E-03	1.12E-08	nd	2.79E-08	1.24E-05	1.82E-06	1.32E-08	2.71E-07	9.90E-07	6.59E-07	2.59E-07	6.26E-10	5.55E-09	1.03E-08	6.92E-09	8.87E-09	1.01E-08	9.37E-09	9.40E-09
W2 04152014 0840 S13	07031407	7/3/14 9:10 PM	4/15/14 8:40 AM	4.81E-03	3.02E-05	1.48E-06	1.20E-04	8.44E-13	1.00E-04	6.08E-03	3.66E-08	3.37E-09	1.11E-07	2.24E-05	1.05E-06	9.37E-09	2.03E-07	7.44E-07	5.75E-07	3.21E-07	2.09E-08	2.67E-09	6.33E-09	2.79E-09	5.20E-09	5.96E-09	4.15E-09	5.08E-09
W2-04232014-2205 S14	07051405	7/5/14 5:51 PM	4/23/14 10:05 PM	4.80E-03	2.86E-05	1.12E-06	1.19E-04	1.00E-12	1.02E-04	7.08E-03	4.39E-08	nd	1.23E-07	2.05E-05	1.59E-06	7.21E-09	1.61E-07	5.88E-07	4.73E-07	3.01E-07	2.40E-07	1.75E-09	4.38E-09	1.94E-09	3.14E-09	4.31E-09	2.66E-09	2.63E-09
W2-05032014-0845 S15	07051406	7/5/14 9:14 PM	5/3/14 8:45 AM	1.10E-01	5.12E-04	7.78E-04	2.19E-03	2.08E-12	9.06E-05	1.66E-02	1.52E-06	1.88E-07	1.83E-06	5.40E-04	2.51E-06	8.35E-09	2.01E-07	7.22E-07	5.38E-07	3.02E-07	3.75E-07	2.30E-09	6.06E-09	1.93E-09	4.59E-09	5.96E-09	3.21E-09	2.81E-09
W2-05152014-1030 S16	02261504	2/26/15 10:30 AM	5/15/14 10:30 AM	7.56E-02	4.43E-04	8.67E-04	3.22E-03	3.71E-12	3.18E-04	8.42E-03	1.19E-06	nd	nd	5.63E-04	5.80E+18	8.37E-07	2.50E-06	1.39E-06	2.28E-06	2.91E-06	0.00E+00	1.08E-06	3.77E-06	2.08E-06	3.28E-06	3.87E-06	3.96E-06	4.44E-06
W2-05312014-1320 S17	02241505	2/24/15 4:54 PM	5/31/14 1:20 PM	1.39E-01	7.28E-04	8.32E-04	5.09E-03	3.71E-12	2.87E-04	9.33E-03	3.10E-06	6.76E-08	1.69E-06	1.07E-03	1.15E+05	1.35E-08	9.49E-07	4.04E-06	1.95E-05	2.14E-05	6.50E-14	1.30E-10	nd	1.35E-09	1.16E-09	nd	4.12E-09	6.88E-09
W2-06182014-1302 S18	02241504	2/24/15 1:47 PM	6/18/14 1:02 PM	5.39E-02	3.42E-04	1.73E-04	2.12E-03	2.88E-12	3.19E-04	6.52E-03	8.78E-07	nd	1.41E-06	4.54E-04	2.51E+34	2.05E-08	3.81E-07	2.57E-07	4.40E-07	4.91E-07	0.00E+00	1.94E-07	7.87E-07	4.10E-07	6.31E-07	7.56E-07	8.70E-07	9.03E-07
W2-07112014-0950 S19	02251506	2/25/15 6:24 PM	7/11/14 9:50 AM	1.27E+00	2.59E-03	2.02E-01	1.90E-02	1.59E-11	1.97E-04	5.84E-02	3.36E-05	2.87E-06	4.14E-05	1.55E-02	1.65E+21	2.22E-07	9.45E-07	5.75E-07	8.86E-07	1.18E-06	0.00E+00	4.33E-07	1.54E-06	8.42E-07	1.35E-06	1.59E-06	1.65E-06	1.82E-06
W2-08082014-0800 S20	02241503	2/24/15 10:41 AM	8/8/14 8:00 AM	4.22E-01	2.04E-03	4.83E-03	1.25E-02	8.10E-12	3.01E-04	1.94E-02	1.06E-05	3.51E-07	6.80E-06	4.36E-03	2.75E+23	2.16E-07	1.15E-06	6.86E-07	1.09E-06	1.44E-06	0.00E+00	5.52E-07	2.07E-06	1.13E-06	1.71E-06	1.98E-06	2.24E-06	2.33E-06
W2-09112014-1040 S21	02261502	2/26/15 3:44 AM	9/11/14 10:40 AM	1.11E-02	7.21E-05	3.17E-05	5.69E-04	2.91E-12	3.23E-04	6.51E-03	6.48E-08	1.15E-07	1.76E-07	9.83E-05	1.21E+03	2.40E-08	1.59E-06	6.19E-06	3.01E-05	3.43E-05	1.81E-04	1.63E-10	9.33E-10	1.39E-09	nd	nd	6.68E-10	nd
W2-10272014-1430 S22	02251503	2/25/15 10:30 AM	10/27/14 2:30 PM	2.03E-02	1.02E-04	-2.74E-04	1.04E-03	3.40E-12	4.95E-04	4.96E-03	1.26E-07	2.65E-07	1.25E-08	1.50E-04	1.70E+04	1.61E-08	1.33E-06	5.66E-06	3.04E-05	3.70E-05	2.59E-06	nd	nd	nd	nd	7.99E-10	nd	5.29E-09
W2-12142014-1430 S23	08111505	8/11/15 5:12 PM	12/14/14 2:30 PM	1.02E-04	-1.96E-08	1.85E-04	8.08E-07	1.38E-12	1.09E-04	9.17E-03	2.44E-07	8.96E-08	1.07E-06	3.21E-05	1.03E-08	4.00E-08	1.97E-08	2.89E-08	5.43E-08	5.17E-08	1.17E-08	4.66E-10	5.57E-10	3.73E-10	8.56E-10	nd	nd	6.22E-10
W2-07132015-1140 S24	08121505	8/12/15 2:26 PM	7/13/15 11:40 AM	1.10E-01	2.51E-07	1.04E-03	7.85E-05	2.39E-12	9.71E-05	1.78E-02	1.29E-06	1.97E-07	9.02E-07	6.24E-04	1.48E-08	5.74E-08	4.51E-08	1.40E-07	9.70E-07	1.63E-07	1.59E-08	1.25E-10	9.66E-10	3.18E-10	1.82E-09	1.16E-09	nd	7.77E-10
W2-08052015-1015	08111504	8/11/15 1:56 PM	8/5/15 10:15 AM	nd	nd	nd	nd	2.64E-12	2.07E-04	9.25E-03	1.14E-07	4.73E-08	nd	nd	9.52E-09	3.65E-08	2.04E-08	3.24E-08	7.17E-08	6.95E-08	1.13E-08	nd	nd	nd	5.03E-10	nd	9.39E-10	4.83E-10

Table 3. Well 1 (W1) Hydrocarbon Composition Data from Isotech

Isotech No	Sample	Sample Date	Sample Time	GC Date	He	H_2	Ar	O_2	CO_2	N_2	CO	C_1	C_2	C_2H_4	C_3	C_3H_6	iC_4	nC_4	iC_5	nC_5	C_6+	MS Date	$\delta^{13}C_1$	δDC_1	$\delta^{13}C_2$	Spec. Grav.	BTU	Pressure On Tag
497332	W1 02122014-1420 S1	2/12/2014	14:20	3/18/2015	0.0563	0.161	0.0314	0.83	0.89	3.96	nd	85.86	6.93	nd	1.04	nd	0.0443	0.138	0.0134	0.0212	0.0265	5/19/2015	-45.72	-166.2	-34.44	0.630	1029	ATM
497333	W1 02142014-1400 S2	2/14/2014	14:00	3/18/2015	0.0595	0.146	nd	0.016	0.94	0.92	nd	89.55	7.07	nd	1.05	nd	0.0445	0.138	0.0134	0.0212	0.0295	8/25/2015	-45.73	-164.9	nd	0.614	1070	ATM
497334	W1 02162014-1420 S3	2/16/2014	14:20	3/18/2015	0.0577	0.189	0.0088	0.16	1.06	1.41	nd	89.04	6.84	nd	0.996	nd	0.0435	0.132	0.0134	0.0212	0.0304	8/25/2015	-45.64	-166.8	nd	0.617	1059	ATM
497335	W1 02182014-1430 S4	2/18/2014	14:30	3/18/2015	0.0331	0.0709	0.0111	0.23	1.03	1.48	nd	78.51	11.33	nd	3.91	nd	0.448	1.29	0.315	0.509	0.832	8/25/2015	-45.58	-169.2	nd	0.725	1228	ATM
455224	W1 02202014-1414 S5	2/20/2014	14:14	9/9/2014	0.0287	0.0486	nd	nd	0.84	0.63	nd	76.81	12.70	nd	4.80	nd	0.552	1.61	0.373	0.610	1.00	9/19/2014	-45.65	-171.7	nd	0.747	1286	
497336	W1 02222014-1415 S6	2/22/2014	14:15	3/18/2015	0.0197	0.0183	nd	nd	0.53	0.57	nd	72.93	14.62	nd	6.05	nd	0.738	2.12	0.501	0.791	1.11	8/25/2015	-45.65	-169.3	nd	0.784	1354	50 psi
497337	W1 02242014-1400 S7	2/24/2014	14:00	3/18/2015	0.0172	nd	nd	nd	0.46	0.57	nd	72.12	15.47	nd	6.52	nd	0.763	2.19	0.464	0.718	0.704	8/21/2015	-45.78	-167.9	nd	0.782	1352	100 psi
497338	W1 02262014-1400 S8	2/26/2014	14:00	3/18/2015	0.0160	nd	nd	nd	0.40	0.58	nd	71.89	16.03	nd	6.72	nd	0.750	2.14	0.408	0.620	0.450	8/25/2015	-45.83	-171.3	nd	0.776	1344	150 psi
497339	W1 02282014-1405 S9	2/28/2014	14:05	3/18/2015	0.0154	nd	nd	nd	0.37	0.57	nd	70.53	16.11	nd	6.97	nd	0.806	2.37	0.499	0.794	0.970	5/19/2015	-45.94	-167.0	-34.44	0.800	1383	35 psi
497340	W1 03032014-1400 S10	3/3/2014	14:00	3/18/2015	0.0153	0.0239	nd	0.030	0.38	0.66	nd	71.42	16.31	nd	6.86	nd	0.751	2.13	0.393	0.589	0.438	8/25/2015	-45.95	-170.3	nd	0.777	1345	ATM
497341	W1 03082014-1445 S11	3/8/2014	14:45	3/18/2015	0.0155	nd	nd	nd	0.24	0.56	nd	70.81	16.30	nd	7.02	nd	0.803	2.34	0.477	0.748	0.685	8/25/2015	-45.90	-171.0	nd	0.791	1373	30 psi
497362	W1 03132014-1300 S12	3/13/2014	13:00	3/18/2015	0.0152	nd	nd	nd	0.37	0.57	nd	70.90	16.08	nd	7.03	nd	0.805	2.30	0.460	0.706	0.759	8/25/2015	-45.98	-169.0	nd	0.792	1370	30 psig
497342	W1 03202014-1230 S13	3/20/2014	12:30	3/18/2015	0.0172	nd	nd	nd	0.36	0.56	nd	71.26	16.15	nd	6.93	nd	0.787	2.26	0.444	0.675	0.556	5/20/2015	-45.97	-167.7	-34.45	0.784	1359	25 psi
455227	W1 03312014-830 S14	3/31/2014	8:30	9/10/2014	0.0159	0.0196	nd	nd	1.55	0.65	nd	71.23	14.84	nd	6.55	nd	0.796	2.27	0.498	0.752	0.826	9/19/2014	-45.87	-171.0	nd	0.795	1345	
497343	W1-04072014-1250 S15	4/7/2014	12:50	3/18/2015	0.0166	nd	nd	nd	0.46	0.57	nd	71.81	16.16	nd	6.76	nd	0.732	2.08	0.381	0.574	0.452	8/25/2015	-46.10	-169.5	nd	0.775	1341	25 psi
497344	W1-04192014-1240 S16	4/19/2014	12:40	3/18/2015	0.0184	nd	nd	0.013	0.43	0.66	nd	72.86	15.66	nd	6.35	nd	0.674	1.94	0.361	0.556	0.480	8/25/2015	-46.32	-171.2	nd	0.766	1326	ATM
455228	W1 05052014-845 S17	5/5/2014	8:45	9/10/2014	0.0195	nd	nd	nd	0.42	0.60	nd	73.11	15.44	nd	6.33	nd	0.669	1.97	0.357	0.557	0.526	9/19/2014	-46.39	-171.5	nd	0.765	1327	
497345	W1-05232014-0830 S18	5/23/2014	8:30	3/18/2015	0.0196	nd	nd	nd	0.43	0.59	nd	73.57	15.48	nd	6.19	nd	0.651	1.86	0.340	0.510	0.361	8/25/2015	-46.57	-170.7	nd	0.757	1314	30 psi
497346	W1-06152014-1010 S19	6/15/2014	10:10	3/18/2015	0.0200	nd	nd	nd	0.42	0.58	nd	73.49	15.47	nd	6.24	nd	0.664	1.90	0.337	0.500	0.380	8/25/2015	-46.55	-168.5	nd	0.758	1316	150 psi
497347	W1-07132014-0800 S20	7/13/2014	8:00	3/18/2015	0.0210	nd	nd	nd	0.45	0.58	nd	74.12	15.09	nd	5.94	nd	0.635	1.83	0.358	0.550	0.423	8/25/2015	-46.52	-170.1	nd	0.755	1310	150 psi
497363	W1-08162014-1100 S21	8/16/2014	11:00	3/18/2015	0.0190	nd	nd	nd	0.43	0.58	nd	73.59	15.27	nd	6.24	nd	0.679	1.92	0.359	0.530	0.380	8/25/2015	-46.52	-171.5	nd	0.759	1317	100 psig
497348	W1-10272014-1500 S22	10/27/2014	15:00	3/19/2015	0.0124	nd	nd	nd	0.50	0.36	nd	80.38	11.81	nd	3.93	nd	0.514	1.25	0.320	0.449	0.478	5/14/2015	-43.52	-162.5	-32.65	0.708	1237	100 psig
529412	W1 11182014-1220 S23	11/18/2014	12:20	9/2/2015	0.0198	nd	nd	nd	0.45	0.57	nd	73.72	15.35	nd	6.13	nd	0.657	1.85	0.347	0.515	0.388	nd	nd	nd	nd	0.765	1326	
529413	W1 01202015-0950 S24	1/20/2015	9:50	9/2/2015	0.0194	nd	nd	nd	0.47	0.58	nd	74.28	15.27	nd	5.97	nd	0.624	1.73	0.304	0.440	0.311	nd	nd	nd	nd	0.749	1300	
529414	W1 07132015-1038 S25	7/13/2015	10:38	9/2/2015	0.0199	nd	nd	nd	0.48	0.56	nd	73.18	15.29	nd	6.17	nd	0.684	1.99	0.417	0.653	0.558	9/7/2015	-46.41	-173.1	nd	0.768	1330	
529415	W1 08052015-0930	8/5/2015	9:30	9/2/2015	0.0125	nd	nd	nd	0.55	0.35	nd	80.00	11.95	nd	3.98	nd	0.520	1.29	0.326	0.460	0.566	9/7/2015	-43.49	-167.4	nd	0.712	1244	

Table 4. Well 2 (W2) Hydrocarbon Composition Data from Isotech

Isotech No	Sample	Sample Date	Sample Time	GC Date	He	H_2	Ar	O_2	CO_2	N_2	CO	C_1	C_2	C_2H_4	C_3	C_3H_6	iC_4	nC_4	iC_5	nC_5	C_6+	MS Date	$\delta_{13}C1$	δDC1	δ13C2	Spec. Grav.	BTU	Pressure On Tag
497364	W2 03102014-1230 S1	3/10/2014	12:30	3/19/2015	0.0106	0.0352	0.277	6.74	1.02	25.88	nd	58.37	5.32	nd	1.24	nd	0.143	0.349	0.0941	0.138	0.388	8/25/2015	-37.59	-158.7		0.769	762	ATM
497349	W2 03122014-1605 S2	3/12/2014	16:05	3/19/2015	0.0087	nd	0.934	20.97	0.099	77.97	nd	0.0014	0.0003	nd	0.0001	nd	nd	0.0002	0.0001	0.0003	0.0154					1.001	1	ATM
497365	W2 03142014-1210 S3	3/14/2014	12:10	3/19/2015	0.0374	0.108	nd	nd	1.31	0.52	nd	91.33	5.34	nd	0.654	nd	0.0325	0.0890	0.0120	0.0215	0.549	5/12/2015	-43.03	-164.1	-32.71	0.616	1070	45 psi
455225	W2 03162014-1245 S4	3/16/2014	12:45	9/9/2014	0.0316	0.0828	nd	nd	1.62	0.48	nd	89.93	6.06	nd	1.02	nd	0.0911	0.232	0.0548	0.0816	0.316	9/19/2014	-42.86	-165.7		0.625	1077	
497350	W2 03182014-1030 S5	3/18/2014	10:30	3/19/2015	0.0202	0.0363	nd	nd	1.01	0.42	nd	82.54	9.88	nd	3.07	nd	0.405	1.01	0.283	0.425	0.903	5/20/2015	-42.89	-163.0	-32.44	0.699	1210	25 psig
497366	W2 03202014-1515 S6	3/20/2014	15:15	3/19/2015	0.0370	0.0926	0.0101	0.17	1.96	1.16	nd	87.20	5.43	nd	1.34	nd	0.206	0.604	0.221	0.363	1.21	8/25/2015	-42.79	-157.9		0.670	1123	ATM
497351	W2 03222014-1230 S7	3/22/2014	12:30	3/19/2015	nd	nd	0.931	20.92	0.044	77.94	nd	0.116	0.0224	nd	0.0097	nd	0.0016	0.0037	0.0014	0.0020	0.0109					1.000	3	-5"Hg
497352	W2 03242014-0830 S8	3/24/2014	8:30	3/19/2015	0.0137	0.0171	nd	0.013	0.62	0.43	nd	79.89	11.92	nd	4.03	nd	0.522	1.27	0.307	0.432	0.534	8/25/2015	-43.15	-160.4		0.712	1239	ATM
497367	W2-03262014-1520 S9	3/26/2014	15:20	3/19/2015	0.0120	0.0113	nd	nd	0.50	0.39	nd	78.44	12.58	nd	4.39	nd	0.585	1.50	0.386	0.566	0.641	8/25/2015	-43.10	-163.7		0.728	1269	10 psi
455226	W2 03292014-1230 S10	3/29/2014	12:30	9/10/2014	0.0113	nd	nd	nd	0.46	0.37	nd	78.31	12.44	nd	4.41	nd	0.595	1.53	0.406	0.604	0.865	9/19/2014	-43.16	-165.6		0.734	1280	
497353	W2-04032014-1325 S11	4/3/2014	13:25	3/19/2015	0.0110	nd	nd	nd	0.40	0.37	nd	78.79	12.63	nd	4.36	nd	0.562	1.39	0.337	0.482	0.669	8/25/2015	-43.19	-164.6		0.723	1264	60 psig
497354	W2-04082014-1250 S12	4/8/2014	12:50	3/18/2015	0.0126	nd	nd	nd	0.42	0.37	nd	78.85	12.47	nd	4.31	nd	0.564	1.39	0.346	0.495	0.774	8/25/2015	-43.26	-165.1		0.725	1267	25 psig
497355	W2-04152014-0840 S13	4/15/2014	8:40	3/18/2015	0.0118	nd	nd	nd	0.45	0.37	nd	79.29	12.44	nd	4.27	nd	0.551	1.35	0.321	0.454	0.492	5/20/2015	-43.30	-164.2		0.716	1252	20 psig
497356	W2-04232014-2205 S14	4/23/2014	22:05	3/18/2015	0.0120	nd	nd	0.011	0.46	0.43	nd	80.70	12.16	nd	3.94	nd	0.473	1.08	0.222	0.290	0.219	8/25/2015	-43.29	-163.3		0.695	1217	100 psig
497368	W2-05032014-0845 S15	5/3/2014	8:45	3/19/2015	0.0128	nd	nd	nd	0.46	0.39	nd	80.78	12.06	nd	3.89	nd	0.473	1.11	0.240	0.322	0.262	5/20/2015	-43.33	-163.0		0.696	1220	100 psi
497357	W2-05152014-1030 S16	5/15/2014	10:30	3/18/2015	0.0126	nd	nd	nd	0.48	0.37	nd	80.62	11.98	nd	3.92	nd	0.486	1.15	0.261	0.359	0.362	8/25/2015	-43.46	-164.6		0.701	1227	100 psig
497358	W2-05312014-1320 S17	5/31/2014	13:20	3/18/2015	0.0126	nd	nd	nd	0.48	0.36	nd	79.72	12.22	nd	4.16	nd	0.536	1.31	0.316	0.444	0.445	8/25/2015	-43.47	-164.3		0.712	1245	200 psig
497359	W2-06182014-1302 S18	6/18/2014	13:02	3/18/2015	0.0140	nd	nd	nd	0.49	0.37	nd	80.97	11.68	nd	3.77	nd	0.479	1.15	0.283	0.395	0.404	8/25/2015	-43.53	-165.3		0.700	1225	200 psig
497369	W2-07112014-0950 S19	7/11/2014	9:50	3/19/2015	0.0136	nd	nd	nd	0.51	0.36	nd	80.95	11.87	nd	3.82	nd	0.467	1.12	0.254	0.346	0.287	5/20/2015	-43.58	-162.5		0.696	1220	150 psi
497370	W2-08082014-0800 S20	8/8/2014	8:00	3/19/2015	0.0139	nd	nd	nd	0.49	0.35	nd	80.48	11.77	nd	3.87	nd	0.501	1.23	0.320	0.457	0.516	8/25/2015	-43.49	-165.5		0.707	1237	150 psi
497360	W2-09112014-1040 S21	9/11/2014	10:40	3/18/2015	0.0136	nd	nd	nd	0.51	0.36	nd	80.83	11.73	nd	3.80	nd	0.483	1.15	0.286	0.400	0.438	8/25/2015	-43.56	-164.6		0.702	1228	100 psig
497361	W2-10272014-1430 S22	10/27/2014	14:30	3/18/2015	0.0193	nd	nd	nd	0.46	0.57	nd	73.72	15.11	nd	6.11	nd	0.672	1.94	0.386	0.581	0.427	5/12/2015	-46.48	-171.7	-34.63	0.760	1318	100 psig
529416	W2 12142014-1430 S23	12/14/2014	14:30	9/2/2015	0.0126	nd	nd	nd	0.53	0.37	nd	80.56	11.81	nd	3.85	nd	0.492	1.20	0.306	0.433	0.440					0.705	1232	
529417	W2 07132015-1140 S24	7/13/2015	11:40	9/2/2015	0.0131	nd	nd	nd	0.55	0.37	nd	80.16	11.87	nd	3.90	nd	0.503	1.24	0.323	0.468	0.600	9/8/2015	-43.58	-166.7		0.711	1242	
529418	W2 08052015-1015	8/5/2015	10:15	9/2/2015	0.0193	nd	nd	nd	0.48	0.56	nd	73.28	15.32	nd	6.19	nd	0.681	1.96	0.389	0.599	0.523	9/8/2015	-46.49	-174.2		0.765	1326	

Distribution

1	MS0359	D. Chavez, LDRD Office	1911
1	MS0899	Technical Library	9536 (electronic copy)


Sandia National Laboratories